MECHANICAL STRESS AND STRESS COMPENSATION IN HALL SENSORS

A Thesis
Presented to
The Academic Faculty

By

Juan Manuel Cesaretti

In Partial Fulfillment
Of the Requirements for the Degree
Master of Science in
Electrical and Computer Engineering

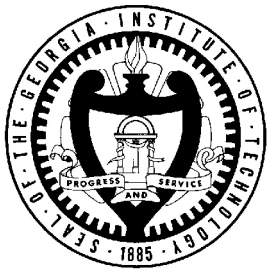

Georgia Institute of Technology
May 2008

MECHANICAL STRESS AND STRESS COMPENSATION IN HALL SENSORS

Approved by:

Dr. Oliver Brand, Advisor
School of Electrical and Computer Engineering
Georgia Institute of Technology

Dr. Paul Hasler
School of Electrical and Computer Engineering
Georgia Institute of Technology

Dr. William P. Taylor
Allegro MicroSystems, Inc.

Date Approved: March 21, 2008

To my wife.
To my parents,
my brother and sister.

ACKNOWLEDGEMENTS

Many people have helped me fulfill this project. First of all, I would like to thank my advisor, Dr. Oliver Brand. His guidance and insights have been invaluable during the course of this research. In addition to his technical expertise, I feel blessed to have had the opportunity to work with such a remarkable person on the human level.

I would also like to acknowledge the thesis committee members, Dr. Paul Hasler and Dr. Bill Taylor. In particular, I would like to thank Dr. Taylor for his observations, helping to guide my research efforts, and for his continuous support, making sure that at all times I had the tools to continue this investigation.

I have enjoyed very much working with the current and past members of our research group. To Jae Hyeong Seo, Kemal Safak Demirci, Kianoush Naeli, Stuart Truax, Luke A. Beardslee and Albert Byun many thanks for their help, comments and companionship during the course of this thesis research.

This experience would have not been possible if not for the financial, logistical and emotional support of the Fulbright program. Many thanks to Fulbright Commission in Argentina for their help in arranging my arrival to Georgia Tech and to the Fulbright Association in Atlanta for their constant support. Besides its academic purpose, the Fulbright scholarship is a one of a kind opportunity to get involved with people from around the world, and learn about their rich culture and customs.

Gratitude is also expressed to Allegro MicroSystems for their decision to finance this endeavor. Without their knowledge, technologies and resources, I could not have done this research.

I would also like to recognize the importance of Gerardo Monreal, Alejandro Milesi, Hernan Romero, Pablo Bolzinger, Daniel Musciano, Andres Colonna, Eduardo Daniello, Mauricio Contaldo, Bruno Uberti and the rest of the Allegro MicroSystems Argentina Design Center's members in my decision to pursue a Master's degree. It is because of them that I was introduced to the world of IC design, and their passion to this field encouraged me to deepen my knowledge of it.

Also, I would like to thank my family, and in particular my parents, for all the little and big things they did and continue to do to help me in every aspect of my life. Their faith in me made me be who I am today.

Finally I want to acknowledge my loved wife, Rosana. She believed in me when this project was just a dream and encouraged me to pursue it. She postponed her professional aspirations to follow me to Atlanta and during these two years at Georgia Tech she was there for me in the good days, but more importantly, in the not so good ones. My only hope is that one day I will be able to do for her what she did these two years for me.

TABLE OF CONTENTS

LIST OF TABLES

LIST OF FIGURES

SUMMARY

Silicon magnetic sensors based on the Hall effect have proven to be an excellent sensor choice for many applications, such as position sensing, gear-tooth sensing, contact-less switching and linear sensing. Although a sensor can be trimmed over temperature before it is shipped to the customer, little can be done about the sensitivity's stability once the sensor has been installed in its final application.

The goal of this project is to propose and implement mechanisms to stabilize the Hall sensor's sensitivity through the use of mechanical stress feedback and magnetic feedback.

CHAPTER I

INTRODUCTION

Silicon magnetic sensors based on the Hall effect have proven to be an excellent sensor choice for many applications, such as position sensing, gear-tooth sensing, contact-less switching and linear sensing. Hall sensors have some key advantages when compared with other magnetic sensors: they can be seamlessly integrated in silicon chips with integrated circuits for amplification and control with no added processing steps [1], and their offset can be dynamically compensated [2]. The integrated circuitry allows for the gain of the system to be adjusted to, for example, obtain a flat response over temperature. If the application requires a higher degree of accuracy, each sensor can be individually calibrated by means of integrated memory cells.

Although a sensor can be trimmed before it is shipped to the customer, little can be done about the stability of the device's gain once the part has been installed in its final application. The long-term stability of the sensor can be affected by various factors [3], with the moisture absorption of the sensor's plastic package being one of the most important. The package will swell in a high humidity environment [4], causing the stress seen by the silicon die to vary [5]. This change in the stress will cause the sensitivity of the sensor to be modified due to the piezo-Hall effect [6]. Sensitivity changes due to this effect are currently difficult to predict in current commercial sensors.

Two approaches to cope with this issue have been investigated in this thesis work. The first one is based on a mechanical stress feedback. If piezoresistors are integrated

close to the Hall sensor, their values can be monitored to detect changes in the stress conditions on the die surface. Any change in stress sensed by the integrated resistors can then be used to estimate the change in the Hall plate sensitivity. The second approach is to rely on a magnetic feedback from a known magnetic field, generated by a coil integrated on the silicon chip, and surrounding the Hall plate. The reference magnetic field can be used to implement a feedback system to dynamically compensate variations in the sensor's gain due to not only changes in the humidity conditions but due to temperature changes as well.

This thesis has been structured into three sections. The first section, consisting of Chapters 2 and 3, is mainly theoretical, and serves as an introduction to the concepts used in the rest of the thesis. Chapter 2 presents the concept of Hall sensors and develops the theory behind them. Chapter 3 introduces the reader to the theoretical background of stress, the origin of stress in silicon integrated circuits and the effects of stress on Hall-based magnetic sensors.

The second section discusses the proposed compensation techniques to deal with the effects of stress. Chapter 4 is dedicated to the compensation by mechanical stress feedback. It presents an experiment designed to measure the effect of stress in various devices. A compensation scheme is presented and a particular system implementation is proposed in the final section of this chapter. Chapter 5 studies the compensation of stress-induced sensitivity changes by using a magnetic reference signal. Its objective is to present a coil implementation that can match or exceed the performance of previous integrated coils, and propose a closed loop system implementation that can stabilize the Hall plate sensitivity and the overall system gain.

The third section, consisting of Chapter 6, presents the conclusions of this investigation and discusses possible future work. Figure 1.1 shows a schematic diagram of the thesis structure.

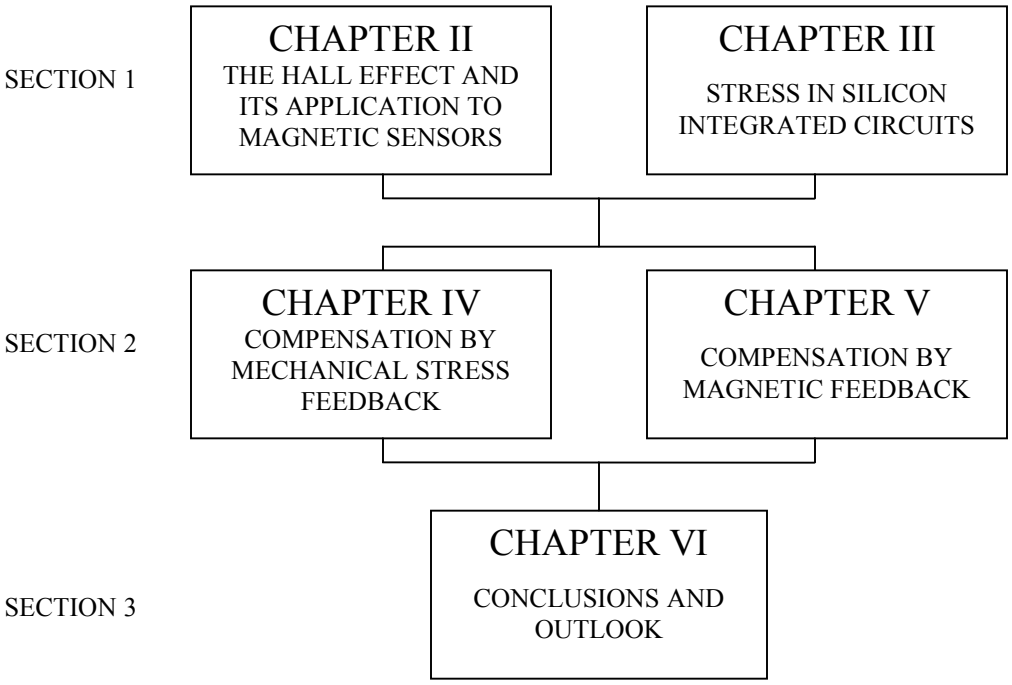

Figure 1.1 - *Thesis structure.*

CHAPTER II

THE HALL EFFECT AND ITS APPLICATION TO MAGNETIC SENSORS

2.1 Magnetic Field Sensors

Magnetic field sensors are commonly used in a broad spectrum of applications. Different detection techniques and their implementations can be found in industrial, medical, military and scientific settings. Depending on their sensitivity they can be classified as low field, Earth's field and bias field sensors [7].

Low field sensors are capable of sensing fields as low as 10 fT (100 pG). This category includes superconducting quantum interference devices (SQUID) [8], [9], optically pumped magnetometers [10], [11], nuclear precession magnetometers, Overhauser magnetometers [12], Meissner effect sensors [13], [14], search-coil magnetometers and fiber-optic magnetometers. Low field sensors are mainly used for medical applications and for magnetic anomaly detection (MAD).

Earth's field sensors typically have a detection threshold of 1 nT (10 uG) and include flux-gate magnetometers [15], search-coil magnetometers, anisotropic magnetoresistance (AMR) sensors [16], giant magnetoresistance (GMR) sensors [17] and MEMS based sensors [18]. The major applications of Earth's field sensors are compass navigation, mineral prospecting, traffic control and munitions fusing.

The last category is of bias field sensors, where a minimum field detection of 100 uT (1 G) is needed. Search-coil magnetometers, Hall effect sensors [19], GMR and AMR sensors, magneto-optical sensors, magnetotransistors [20] and magnetodiodes [21] can be employed in this magnetic field range. Bias field sensors are mainly used in contact-less systems, such as position sensing, gear-tooth sensing, contact-less switching, linear sensing and electrical current measuring. The main advantage of these systems in industrial settings is that they are immune to a variety of factors, such as grease, dust and RF noise, which usually cause problems to other sensing mechanisms.

2.2 Hall Effect Sensors

Because the Hall effect is usually small, commercial sensors only became available after the discovery of high mobility semiconductors. Hall sensors have some key advantages when compared with other bias field sensors. They can be seamlessly integrated in silicon chips with ICs for amplification and control with no added processing steps [1], and their offset can be dynamically compensated [2].

2.2.1 Simplified Analysis

The Hall effect was first described by Edwin Hall in 1879 [22]. When a charge-carrying particle is placed under an electromagnetic field, the particle will experience a force with a component parallel to the electric field and a component normal to the magnetic field and to the particle flow. This force is called the Lorentz force, and is given by:

$$\vec{F} = q[\vec{E}_E + \vec{v} \times \vec{B}] \tag{2.1}$$

Where E_E is the external electric field responsible for the particle flow, q is the electric charge of the particle, v is the velocity of the particle and B is the magnetic field. For holes $q_h = q = 1.602 \times 10^{-19}$ *C,* and for electrons $q_e = -q$.

In order to study the Hall effect some approximations will be made [19]: the carrier velocity will be considered to be equal for all the carriers and the thermal motion of the carriers will be neglected. Let's consider two strips of material with length l, width w and thickness t, where l is much larger than w and t (see Figure 2.1). Let one of the strips be n-type and the other p-type. For this calculation the materials will be considered as highly extrinsic (n, $p >> n_i$). In the presence of an external electric field E_E, along the length l, the drift velocity of the carriers and their current density will be given by:

$$\vec{v}_e = -\mu_e \vec{E}_E \tag{2.2}$$

$$\vec{J}_e = -nq_e \mu_e \vec{E}_E = nq\mu_e \vec{E}_E \tag{2.3}$$

$$\vec{v}_h = \mu_h \vec{E}_E \tag{2.4}$$

$$\vec{J}_h = pq_h \mu_h \vec{E}_E = pq\mu_h \vec{E}_E, \tag{2.5}$$

where n is the electron concentration, μ_e is the electron mobility, p is the hole concentration and μ_h is the hole mobility. If now a magnetic field B, normal to the surface defined by l and w (and so normal to the electric field E_E), is also applied, the force on the carriers due to B will be:

$$\vec{F}_{Be} = -q_e \mu_e [\vec{E}_E \times \vec{B}] = q\mu_e [\vec{E}_E \times \vec{B}] \tag{2.6}$$

$$\vec{F}_{Bh} = q_h \mu_h [\vec{E}_E \times \vec{B}] = q\mu_h [\vec{E}_E \times \vec{B}] \tag{2.7}$$

The force acting on the particles will push them to the side of the strips, resulting in an increased carrier concentration along one side of the material and a decreased carrier concentration on the other side. Because of this, an electric field E_H (Hall electric field) will appear that will balance the effect of the magnetic force under steady state conditions.

$$\vec{F}_B + \vec{F}_H = 0 \tag{2.8}$$

$$\vec{F}_{Be} = -\vec{F}_{He} = -q_e \vec{E}_{He} = q\vec{E}_{He} \tag{2.9}$$

$$\vec{F}_{Bh} = -\vec{F}_{Hh} = -q_h \vec{E}_{Hh} = -q\vec{E}_{Hh} \tag{2.10}$$

$$\vec{E}_{He} = \mu_e[\vec{E}_E \times \vec{B}] = -\frac{1}{nq_e}[\vec{J}_e \times \vec{B}] = \frac{1}{nq}[\vec{J}_e \times \vec{B}] = -R_{He}[\vec{J}_e \times \vec{B}] \tag{2.11}$$

$$\vec{E}_{Hh} = -\mu_h[\vec{E}_E \times \vec{B}] = -\frac{1}{pq_h}[\vec{J}_h \times \vec{B}] = -\frac{1}{pq}[\vec{J}_h \times \vec{B}] = -R_{Hh}.[\vec{J}_h \times \vec{B}] \tag{2.12}$$

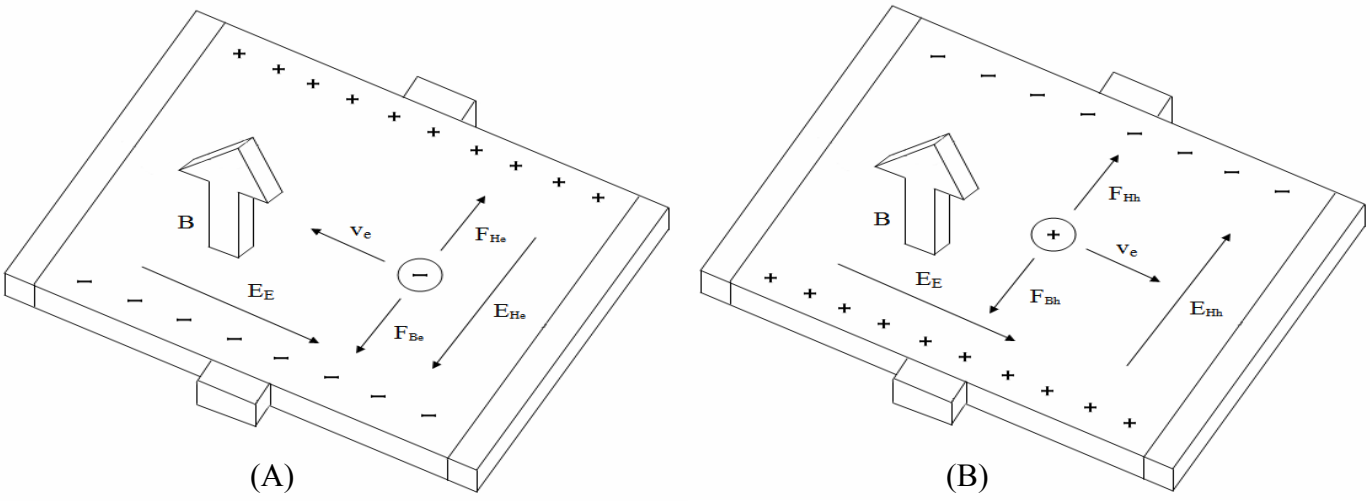

Figure 2.1 - *Hall effect on n-type (A) and p-type (B) long strips (l >> w >> t).*

Where R_H is the Hall coefficient, and for n-type and p-type materials is given by:

$$R_{He} = \frac{1}{nq_e} = -\frac{1}{nq} \tag{2.13}$$

$$R_{Hh} = \frac{1}{pq_h} = \frac{1}{pq} \tag{2.14}$$

2.2.2 Detailed Analysis

A more precise analysis can be carried out by solving the Boltzmann kinetic equation [19]. By taking into account the interactions of carriers with the crystal lattice, the Hall coefficient can be defined as:

$$R_{He} = \frac{r_H}{nq_e} = -\frac{r_H}{nq} \tag{2.15}$$

$$R_{Hh} = \frac{r_H}{pq_h} = \frac{r_H}{pq} \tag{2.16}$$

Where r_H is the Hall factor, which is given by

$$r_H = r_{H0}\alpha \tag{2.17}$$

In the previous formula r_{H0}, the Hall scattering factor, summarizes the influence of scattering, and α characterizes anisotropy and mixing effects [19]. The Hall scattering factor is equal to

$$r_{H0} = \frac{\langle \tau^2 \rangle}{\langle \tau \rangle^2} \tag{2.18}$$

Where τ is the relaxation time of the carriers involved and the angular brackets denote averaging over electron energies. The Hall scattering factor calculated under the assumption of a spherical intravalley acoustic scattering is equal to:

$$r_{H0} = \frac{3}{8}\pi = 1.18 \tag{2.19}$$

The Hall scattering factor for silicon has been modeled taking into account both isotropic and anisotropic scattering [23]. Its value varies both with doping concentration and temperature, as shown in Figure 2.2.

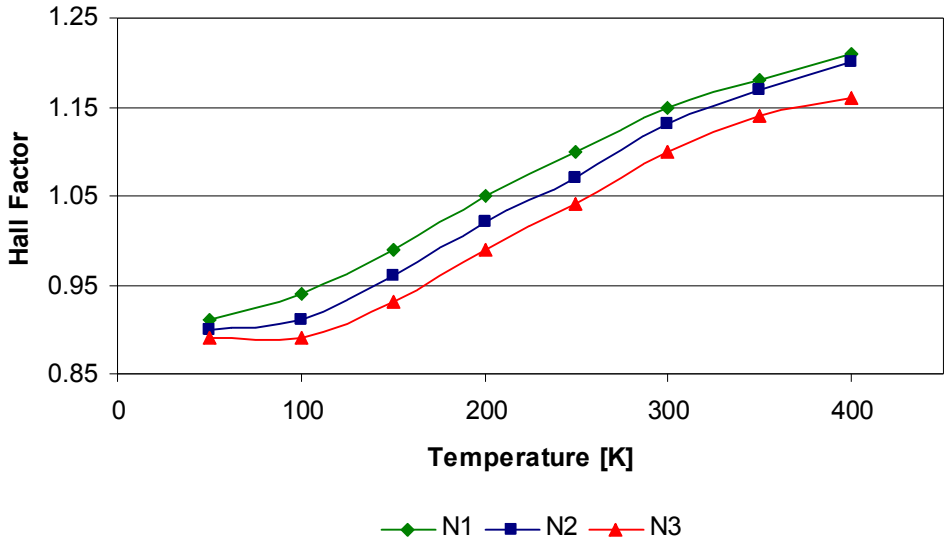

Figure 2.2 - *Hall Factor for different doping concentrations [23].*
N1 = 8.92x10^{13} cm^{-3}, N2 = 9.27 x10^{14} cm^{-3}, N3 = 7.26x10^{15} cm^{-3}.

2.2.3 Hall Voltage

The Hall voltage V_H can be obtained by integrating over the Hall electric field (2.11) and (2.12) between two points at either side of the strip. These two points are selected as to have the same electric potential if no magnetic field is present.

$$V_{He} = R_{He} J_e B w = \frac{IBR_{He}}{t} = \frac{r_H IB}{nq_e t} \tag{2.20}$$

$$V_{Hh} = R_{Hh} J_h B w = \frac{IBR_{Hh}}{t} = \frac{r_H IB}{pq_h t} \tag{2.21}$$

2.2.4 Hall Sensitivity

For the sake of simplicity, all the derivations will be done for an n-type semiconductor strip from now one. The sensitivity of a Hall effect sensor is given by the ratio of the Hall voltage to the applied magnetic field.

$$S|_{ideal} = \frac{V_H}{B} = \frac{IR_H}{t} \tag{2.22}$$

The resistance of the semiconductor strip is given by:

$$R = \frac{l}{nq\mu_e tw} \tag{2.23}$$

If the Hall device is not the ideal case of long strip with point contacts, the sensitivity of the Hall plate can be expressed as:

$$S = G_S S|_{ideal} = G_S \frac{IR_H}{t}, \tag{2.24}$$

where G_S is a geometrical correction factor. If R□ is the sheet resistance of the material with which the Hall plate is constructed, another geometrical correction factor, G_R, can be defined, such that R is:

$$R = G_R R\,\square \tag{2.25}$$

Values of G_S and G_R can be obtained for different shapes of Hall devices [24, 25].

2.2.5 Offset Voltage and Offset Compensation

If no external magnetic field is applied the measured voltage between the sensing terminals of an ideal Hall sensor should be zero. Because of contact misalignments, thermal effects, surface charges and stress this is usually not the case [26]. The value of the offset voltage is unpredictable, and will vary from sample to sample and with

temperature. Static magnetic field measurements are particularly affected. Fortunatelly, the Hall plate offset can be greatly reduced with spatial and time averaging techniques. To study these methods the Hall sensor will be approximated as a Wheatstone bridge [2], as seen in Figure 2.3. The arrow symbolizes the direction of the bias current flow, and V1 and V2 are the output signal terminals. One of the resistors is made different than the other three to model the offset.

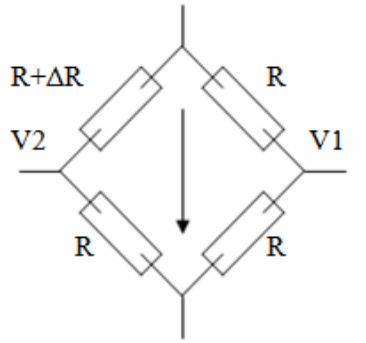

Figure 2.3 *- Simplified Hall plate model for offset analysis.*

If V is the bias voltage, the voltage in the sensing terminals will be:

$$V1 = V\frac{R}{2R} = \frac{V}{2} \tag{2.26}$$

$$V2 = V\frac{R}{2R + \Delta R} = \frac{V}{2 + \Delta R / R} \tag{2.27}$$

Because of the mismatched resistors, an offset *V2 - V1* will appear on the sensing terminals which cannot be readily distinguished from a magnetic signal.

2.2.5.1 Spatial Averaging

A commonly used spatial averaging implementation uses four Hall plates connected as shown in Figure 2.4. This arrangement is usually called a Quad Hall plate.

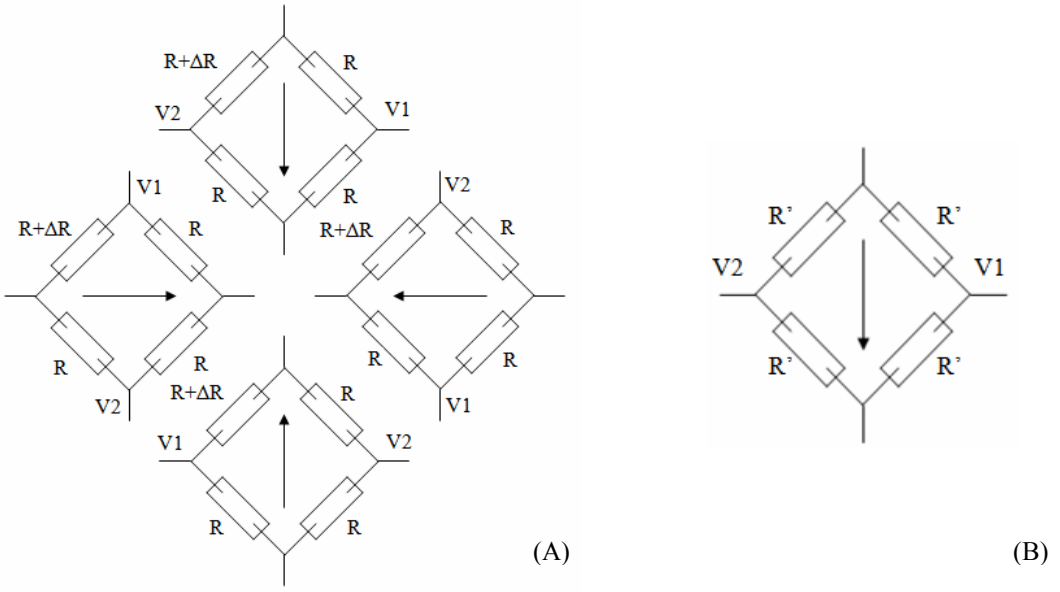

Figure 2.4 - *Spatial averaging offset compensation technique (A). Equivalent circuit (B).*

The connection between the four Hall plates shown in Figure 2.4 (A) is such that the equivalent resistance R' of each of the branches is the same.

$$R' = (R + \Delta R) // R // R // R \tag{2.28}$$

And

$$V1 = V2 = V\frac{R'}{2R'} = \frac{V}{2} \tag{2.29}$$

In an ideal case, the offset should be completely eliminated. In reality each of the Hall plates has a slightly different offset, causing the final offset to be non-zero. The resistance of the Quad Hall plate is four times smaller than that of a single Hall plate, the power consumption quadruples, and the thermal noise is halved.

2.2.5.2 Time Averaging

Time averaging, usually referred to as the spinning-current or chopping technique, consists of spinning the bias current through the Hall plate contacts. Because the Hall voltage rotates with the current, but the offset does not, both signals can be distinguished

and the offset cancelled. The bias current spinning can be discrete [2, 27] or continuous [28]. A simple discrete current spinning system can be implemented with two states (Figure 2.5).

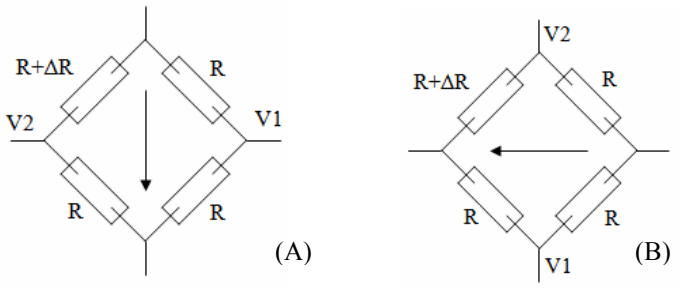

Figure 2.5 *- Example of spinning current implementation. State 1 (A), state 2 (B).*

An external magnetic field is applied such that the magnetic contribution to the output terminals voltage is ± V_B / 2. For state 1 the voltage in the output terminals is:

$$V1_1 = V\frac{R}{2R} + \frac{V_B}{2} = \frac{V}{2} + \frac{V_B}{2}, \qquad V2_1 = V\frac{R}{2R+\Delta R} - \frac{V_B}{2} \tag{2.30}$$

And for state 2,

$$V1_2 = V\frac{R}{2R} + \frac{V_B}{2} = \frac{V}{2} + \frac{V_B}{2}, \qquad V2_2 = V\frac{R+\Delta R}{2R+\Delta R} - \frac{V_B}{2} \tag{2.31}$$

The average of both states will be,

$$V1_{ave} = \frac{V1_1 + V1_2}{2} = \frac{1}{2}\left[\frac{V}{2} + \frac{V}{2} + V_B\right] = \frac{V}{2} + \frac{V_B}{2} \tag{2.32}$$

$$V2_{ave} = \frac{V2_1 + V2_2}{2} = \frac{1}{2}\left[V\frac{R}{2R+\Delta R} + V\frac{R+\Delta R}{2R+\Delta R} - V_B\right] = \frac{V}{2} - \frac{V_B}{2} \tag{2.33}$$

So the voltage difference between the outputs is:

$$V1_{ave} - V2_{ave} = V_B \tag{2.34}$$

A more precise model of the Hall plate uses six resistors [29]. With this model it can be shown that a current-driven Hall plate will provide better offset cancellation than a

voltage-driven Hall plate. Nonlinearities such as the back-bias effect [30] will cause a residual offset.

2.2.7 Current-Driven and Voltage-Driven Hall Plates

A Hall plate can be biased with a constant current or a constant voltage. In order to obtain a figure of merit independent of the biasing conditions, the current-driven and voltage-driven sensitivities will be defined. The Hall sensitivity was defined in Equation (2.24) as:

$$S = G_S \frac{IR_H}{t} \tag{2.35}$$

The current-driven sensitivity can thus be defined as:

$$S_I = \frac{S}{I} = G_S \frac{R_H}{t} = G_S \frac{r_H}{nqt} \tag{2.36}$$

To obtain the voltage-driven sensitivity we will first replace the bias current I with V, the bias voltage, over R, the Hall plate resistance seen from the biasing terminals. The Hall sensitivity as defined in Equation (2.24) can be re-written as:

$$S = G_S \frac{R_H}{t} \frac{V}{R} \tag{2.37}$$

The voltage-driven sensitivity for the long strip case is given by:

$$S_V = \frac{S}{V} = G_S \frac{R_H}{t} \frac{1}{R} = G_S \frac{r_H}{nqt} \frac{1}{R} = G_S \frac{r_H}{nqt} \frac{nq\mu_e tw}{l} = G_S \mu_e \frac{w}{l} r_H \tag{2.38}$$

And for an arbitrary geometry, equation (2.38) becomes:

$$S_V = \frac{G_S}{G_R} \mu_e r_H , \tag{2.39}$$

where G_R is a geometrical factor defined in Equation (2.25).

The sample to sample sensitivity spread for current-driven Hall sensors will depend on the doping and thickness tolerances of the process. As bias currents are usually derived from a constant voltage over a resistor, the sensitivity will also depend on the production spread of this resistor. The sensitivity drift of the current-driven Hall sensor has a small temperature coefficient, originating from r_H.

For voltage-driven Hall sensors, the sample to sample sensitivity spread depends only on the mobility, which makes it more reproducible. As a disadvantage, the sensitivity has a large temperature coefficient due to the mobility variation with temperature.

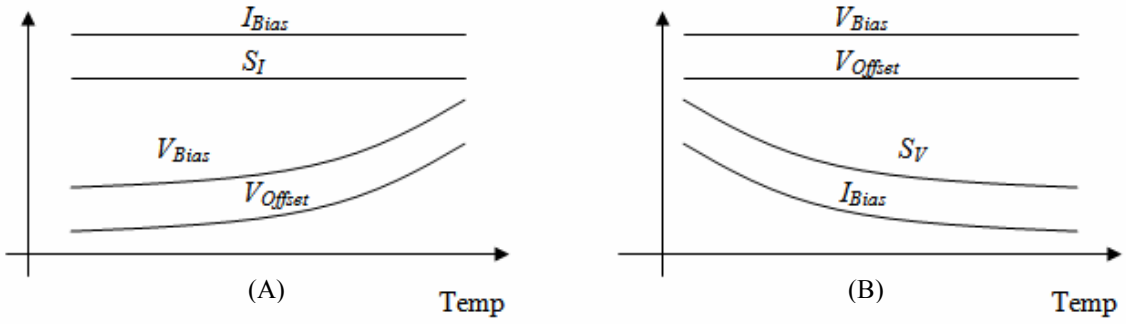

Figure 2.6 - *Current-driven n-EPI Hall plate (A) and voltage-driven n-EPI Hall plate (B) over temperature [31]. V_{Bias} and I_{Bias} are the Hall plate voltage bias and current bias. S_V and S_I are the voltage and current driven sensitivities. Vertical axis not to scale.*

CHAPTER III

STRESS IN SILICON INTEGRATED CIRCUITS

3.1 Silicon Crystalline Structure

The defining property of crystalline materials is that their atoms are ordered in repeating structures. The smallest repeating structure in a crystal is called a unit cell. For the cubic crystal system some common arrangements are simple cubic (SC), body-centered cubic (BCC), face-centered cubic (FCC), diamond (C) and ZincBlend (ZnS). Crystalline silicon has a diamond unit cell, as seen in Figure 3.1, which is comprised of two FCC sub-lattices shifted by one quarter of the diagonal.

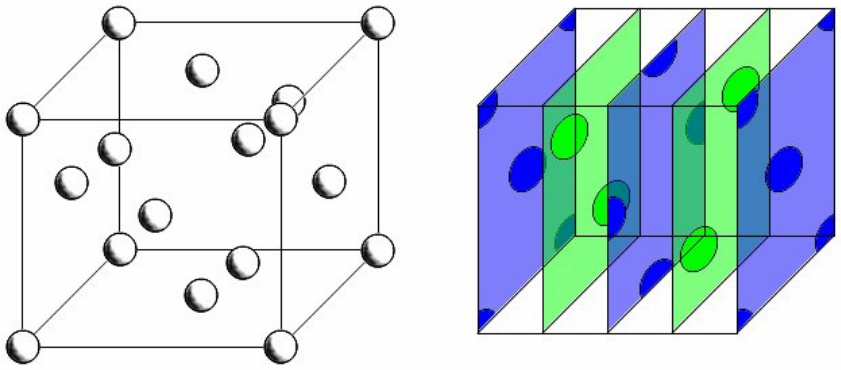

(A) (B)

Figure 3.1 - *Silicon unit cell (A), sliced view (B).*

The Miller indices describe the lattice directions and lattice planes in a crystal. Because of the silicon unit cell symmetry, it is easy to see that, for instance, the directions [100], [010] and [001] are equivalent, and can be grouped into the family of equivalent directions <100> (see Fig. 3.2). Lattice planes are defined by the lattice directions associated with them. For example, the lattice direction [100] is normal to the plane

(100), which, because of the crystal symmetry, can be included in the family of equivalent lattice planes {100}.

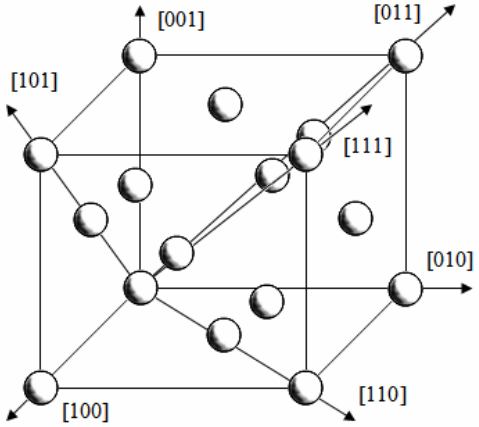

Figure 3.2 - *Common Miller indices.*

In general silicon ingots are grown such that when sliced into wafers their surface coincides with either {100} or {111} lattice planes. In order to identify different types of wafers (crystallographic orientation and type of doping), small parts are removed from the wafer to create what is know as flats. Figure 3.3 depicts a p-type {100} wafer, the type of wafer that is used in this work. The <110> lattice direction is parallel (and perpendicular) to the primary flat, and the <100> lattice direction has a ±45 degree angle with respect to the primary flat.

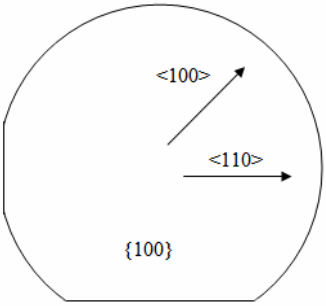

Figure 3.3 - *{100} p-type wafer.*

3.2 Stress

The concept of stress was introduced by Cauchy in 1822, while studying the theory of elasticity [32]. The stress σ can be defined as the force per unit area acting on the surface of an infinitesimal volume:

$$\sigma = \frac{dF}{dA}, \tag{3.1}$$

where dF is the differential force acting on the differential surface dA of the volume. The stress vector σ consists of normal stresses, which act perpendicular to the surface, and shear stresses, which act parallel to the surface area. For the surface normal to the x axis on the differential volume element, the normal stress is given by σ_x and the shear stresses by τ_{xy} and τ_{xz}. Figure 3.4 shows a representation of all the stress components acting on an infinitesimal volume.

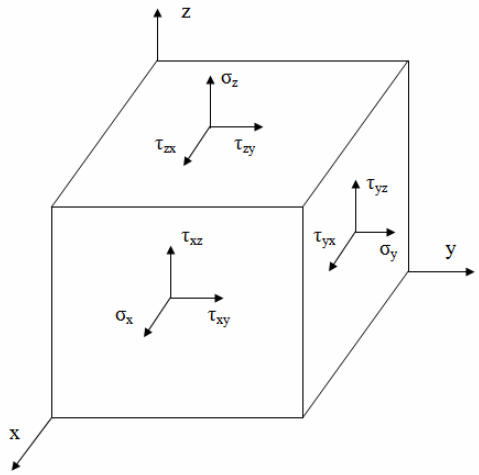

Figure 3.4 - *Stress components acting on an infinitesimal volume.*

The stress tensor can thus be defined as:

$$\sigma_{ij} = \begin{bmatrix} \sigma_x & \tau_{xy} & \tau_{xz} \\ \tau_{yx} & \sigma_y & \tau_{yz} \\ \tau_{zx} & \tau_{zy} & \sigma_z \end{bmatrix} = \begin{bmatrix} \sigma_{11} & \sigma_{12} & \sigma_{13} \\ \sigma_{21} & \sigma_{22} & \sigma_{23} \\ \sigma_{31} & \sigma_{32} & \sigma_{33} \end{bmatrix} \tag{3.2}$$

The differential volume is considered to be in static equilibrium, implying that there are no net forces or torques. Under this condition the stress matrix is symmetric, and has six independent components.

$$\tau_{xy} = \tau_{yx} \tag{3.3}$$

$$\tau_{yz} = \tau_{zy} \tag{3.4}$$

$$\tau_{xz} = \tau_{zx} \tag{3.5}$$

$$\sigma_{ij} = \begin{bmatrix} \sigma_x & \tau_{xy} & \tau_{xz} \\ \tau_{xy} & \sigma_y & \tau_{yz} \\ \tau_{xz} & \tau_{yz} & \sigma_z \end{bmatrix} = \begin{bmatrix} \sigma_{11} & \sigma_{12} & \sigma_{13} \\ \sigma_{12} & \sigma_{22} & \sigma_{23} \\ \sigma_{13} & \sigma_{23} & \sigma_{33} \end{bmatrix} \tag{3.6}$$

3.3 Origin of Stress in Silicon Circuits

The difference in thermal expansion coefficients between silicon and other materials is the main cause of induced thermo-mechanical stress [33]. The total stress induced in the IC can be divided into the stress produced during silicon wafer processing, and the stress induced from packaging.

The stress created during the silicon wafer processing can be categorized into: stress from the thermal processing and slip pattern, film stress and film-edge induced stress, stress problems of embedded structural elements, stress in planar and non-planar thermal oxide, and strain and misfit dislocations in doped lattices [34].

The stress from packaging is mainly due to the die attachment and plastic molding [35]. The process of die attachment occurs at temperatures that are usually higher than the operating temperature. Because of the different thermal expansion coefficients between the substrate and the die, a thermo-mechanical stress will appear when the

temperature is reduced. As with the die attachment process, the stress induced during the encapsulating process is mostly due to the mismatched thermal expansion coefficients of the molding compound and the silicon die. In addition, under a constant applied strain the encapsulating material can show a viscous response and relaxation, resulting in a time dependent stress to strain response [33].

3.4 Stress Induced Effects

There are several effects that arise when a material or device is subjected to stress. Some of these effects are the piezoresistive effect, the piezoelectric effect, the piezo-junction effect, the piezo-Hall effect and the piezo-tunneling effect. In this work, the attention will be focused on the piezoresistive and piezo-Hall effects.

3.4.1 Piezoresistive Effect

The electric field and current density vectors are related by the resistivity tensor ρ by the following expression:

$$\vec{E} = \rho\vec{J} \tag{3.7}$$

$$\begin{bmatrix} E_1 \\ E_2 \\ E_3 \end{bmatrix} = \begin{bmatrix} \rho_{11} & \rho_{12} & \rho_{13} \\ \rho_{21} & \rho_{22} & \rho_{23} \\ \rho_{31} & \rho_{32} & \rho_{33} \end{bmatrix} \begin{bmatrix} J_1 \\ J_2 \\ J_3 \end{bmatrix} \tag{3.8}$$

The piezoresistive effect describes the change in the resistance of a material when a stress is applied to it. The variation in resistivity can be defined in terms of the applied stress tensor σ, the piezoresistance tensor π, and the zero-stress resistivity ρ_o.

$$\frac{\Delta\rho_{ij}}{\rho_o} = \sum_{k,l} \pi_{ijkl}\sigma_{kl} \tag{3.9}$$

Because of its symmetry, the stress tensor can be re-written using the single suffix notation.

$$\sigma = \begin{bmatrix} \sigma_{11} & \sigma_{12} & \sigma_{13} \\ \sigma_{12} & \sigma_{22} & \sigma_{23} \\ \sigma_{13} & \sigma_{23} & \sigma_{33} \end{bmatrix} = \begin{bmatrix} \sigma_1 & \sigma_6 & \sigma_5 \\ \sigma_6 & \sigma_2 & \sigma_4 \\ \sigma_5 & \sigma_4 & \sigma_3 \end{bmatrix} \tag{3.10}$$

The change in resistivity can now be defined as:

$$\frac{\Delta\rho_i}{\rho_o} = \sum_{j} \pi_{ij}\sigma_j \tag{3.11}$$

Because of the cubic crystal symmetry in silicon, the piezoresistance tensor π has only three independent coefficients.

$$\pi_{ij} = \begin{bmatrix} \pi_{11} & \pi_{12} & \pi_{12} & 0 & 0 & 0 \\ \pi_{12} & \pi_{11} & \pi_{12} & 0 & 0 & 0 \\ \pi_{12} & \pi_{12} & \pi_{11} & 0 & 0 & 0 \\ 0 & 0 & 0 & \pi_{44} & 0 & 0 \\ 0 & 0 & 0 & 0 & \pi_{44} & 0 \\ 0 & 0 & 0 & 0 & 0 & \pi_{44} \end{bmatrix} \tag{3.12}$$

The resistivity can thus be written as:

$$\rho = \rho_o \begin{bmatrix} 1 \\ 1 \\ 1 \\ 0 \\ 0 \\ 0 \end{bmatrix} + \rho_o \begin{bmatrix} \pi_{11} & \pi_{12} & \pi_{12} & 0 & 0 & 0 \\ \pi_{12} & \pi_{11} & \pi_{12} & 0 & 0 & 0 \\ \pi_{12} & \pi_{12} & \pi_{11} & 0 & 0 & 0 \\ 0 & 0 & 0 & \pi_{44} & 0 & 0 \\ 0 & 0 & 0 & 0 & \pi_{44} & 0 \\ 0 & 0 & 0 & 0 & 0 & \pi_{44} \end{bmatrix} \begin{bmatrix} \sigma_1 \\ \sigma_2 \\ \sigma_3 \\ \sigma_4 \\ \sigma_5 \\ \sigma_6 \end{bmatrix} \tag{3.13}$$

The piezoresistive coefficients for silicon at room temperature are summarized in Table 3.1 [36]:

Table 3.1 - *Piezo-resistive coefficients in lightly doped silicon at 300K [36].*

	π_{11}	π_{12}	π_{44}
N-Type	-102.2 x 10^{-11} 1/Pa	53.4 x 10^{-11} 1/Pa	-13.6 x 10^{-11} 1/Pa
P-Type	6.6 x 10^{-11} 1/Pa	-1.1 x 10^{-11} 1/Pa	138.1 x 10^{-11} 1/Pa

When the current density is parallel to the electric field, as in long resistors, the piezoresistivity can be expressed by π_T and π_L, the transversal and longitudinal piezo-resistive coefficients. The resistance value of a resistor under in-plane stress is given by:

$$R = Ro.\left[1 + \pi_L.\sigma_L + \pi_T.\sigma_T\right] \tag{3.14}$$

For a long resistor with an arbitrary orientation on the {100} plane with an angle ϕ with respect to the <100> direction, π_L and π_T are given by [36]:

$$\pi_L = \pi_{11} - 2(\pi_{11} - \pi_{12} - \pi_{44})\cos^2\phi\sin^2\phi \tag{3.15}$$

$$\pi_T = \pi_{12} + 2(\pi_{11} - \pi_{12} - \pi_{44})\cos^2\phi\sin^2\phi \tag{3.16}$$

Figure 3.5 shows a graphical representation of the transversal and longitudinal piezoresistive coefficients in the {100} plane at room temperature.

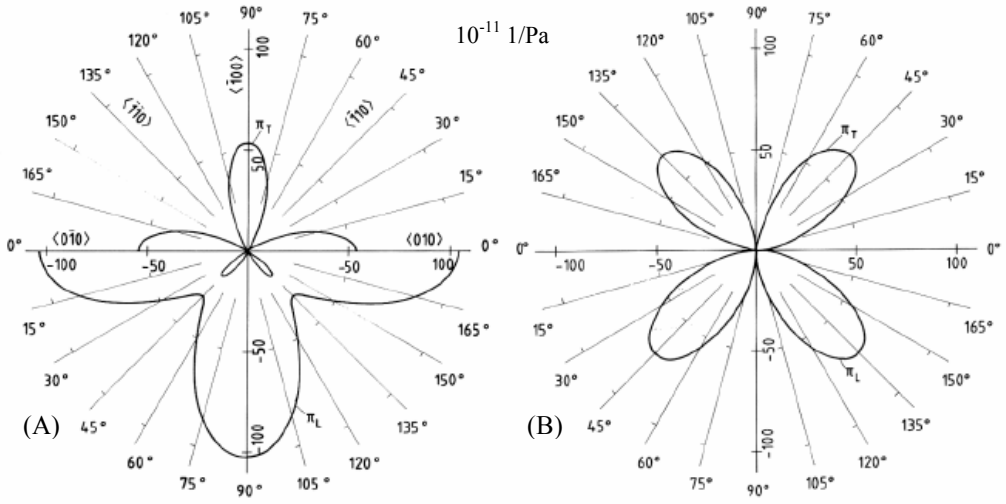

Figure 3.5 - *Transversal and longitudinal piezo-resistive coefficients π_T and π_L of silicon for arbitrary orientations in the {100} plane at 300K [36]. N-type (A). P-type (B).*

The piezoresistive coefficients in silicon vary with the doping concentration of the resistor's material, as seen in Figure 3.6. For low doping concentrations the piezoresistive coefficients remain constant, but start decreasing for higher doping levels.

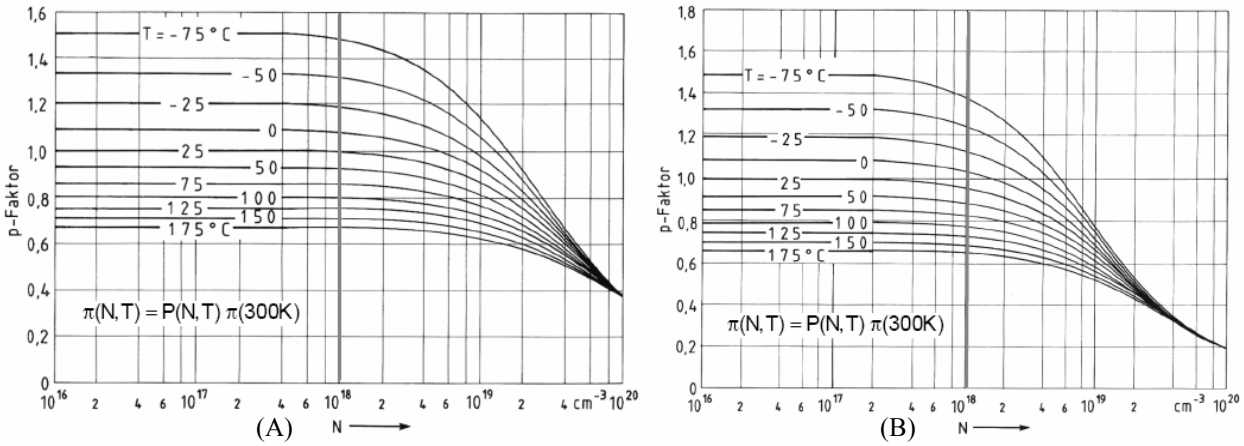

Figure 3.6 - *Effect of doping concentration and temperature on piezo-resistive coefficients of silicon. N-type (A). P-type (B) [36].*

For non-crystalline materials, such as polysilicon, the orientation of the resistor has no effect on its piezo-resistive coefficients. As in the case of crystalline silicon, the coefficients will vary with doping concentration (see Figure 3.7).

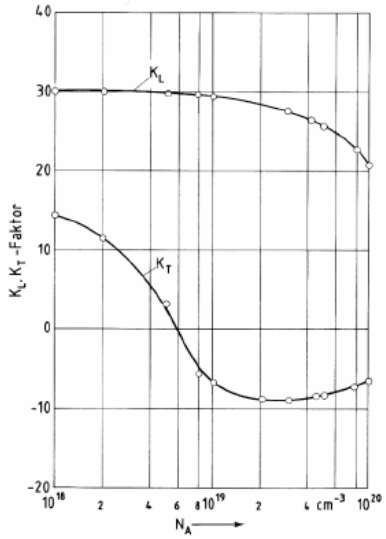

Figure 3.7 - *Effect of doping concentration on piezo-resistive coefficients for polysilicon at 300K [36]. To obtain π_L and π_T, K_L and K_T must be divided by the Young's modulus of the polysilicon film.*

3.4.2 Piezo-Hall Effect

Under the presence of a magnetic field, Equation (3.7) can be re-written as [6]:

$$\vec{E} = \rho\vec{J} - (R_H \vec{B}) \times \vec{J}\,, \tag{3.17}$$

where R_H is the Hall coefficient, as defined in Equations (2.15) and (2.16), and B is the magnetic field vector.

The piezo-Hall effect describes the variation in the Hall coefficient due to mechanical stress. The change in the Hall coefficient can be defined in terms of the applied stress tensor σ, the piezo-Hall tensor P, and the zero-stress Hall coefficient R_{Ho}.

$$\frac{\Delta R_{Hij}}{R_{Ho}} = \sum_{k,l} P_{ijkl}\sigma_{kl} \tag{3.18}$$

Because of its symmetry, the stress tensor can again be described using the single suffix notation, so the above formula can be re-written as:

$$\frac{\Delta R_{Hi}}{R_{Ho}} = \sum_{j} P_{ij}\sigma_{j} \tag{3.19}$$

The crystal symmetry of silicon causes the piezo-Hall tensor P to have only three independent coefficients:

$$P_{ij} = \begin{bmatrix} P_{11} & P_{12} & P_{12} & 0 & 0 & 0 \\ P_{12} & P_{11} & P_{12} & 0 & 0 & 0 \\ P_{12} & P_{12} & P_{11} & 0 & 0 & 0 \\ 0 & 0 & 0 & P_{44} & 0 & 0 \\ 0 & 0 & 0 & 0 & P_{44} & 0 \\ 0 & 0 & 0 & 0 & 0 & P_{44} \end{bmatrix} \tag{3.20}$$

The Hall coefficient tensor can thus be expressed as:

$$R_H = R_{Ho}\begin{bmatrix}1\\1\\1\\0\\0\\0\end{bmatrix} + R_{Ho}\begin{bmatrix}P_{11} & P_{12} & P_{12} & 0 & 0 & 0\\ P_{12} & P_{11} & P_{12} & 0 & 0 & 0\\ P_{12} & P_{12} & P_{11} & 0 & 0 & 0\\ 0 & 0 & 0 & P_{44} & 0 & 0\\ 0 & 0 & 0 & 0 & P_{44} & 0\\ 0 & 0 & 0 & 0 & 0 & P_{44}\end{bmatrix}\begin{bmatrix}\sigma_1\\ \sigma_2\\ \sigma_3\\ \sigma_4\\ \sigma_5\\ \sigma_6\end{bmatrix} \tag{3.21}$$

For n-type silicon, the piezo-Hall coefficients are summarized in Table 3.2 [6].

Table 3.2 - *Piezo-Hall coefficients in lightly doped n-type silicon at 300K [6].*

	P_{11}	P_{12}	P_{44}
N-Type	-93 x 10^{-11} 1/Pa	45 x 10^{-11} 1/Pa	6 x 10^{-11} 1/Pa

For a packaged Hall plate implemented on a {100} wafer, the out-of-plane shear stress components σ_4 and σ_5 are usually much smaller than the components of the in-plane stress state [37]. Similarly, the in-plane shear component σ_6 nearly disappears at a distance to the die edge equal to the die thickness [37]. Thus, the only relevant stress components are the in-plane normal stresses σ_1 and σ_2 and the out-of-plane normal stress σ_3. The current-driven Hall sensitivity variation due to stress for Hall sensors implemented in the {100} plane can thus be written as [38]:

$$\frac{\Delta S_I}{S_I} = P_{12}(\sigma_1 + \sigma_2) + P_{11}\sigma_3 \tag{3.22}$$

Where $\sigma_1 = \sigma_x$, $\sigma_2 = \sigma_y$ and $\sigma_3 = \sigma_z$. It is interesting to note for this particular plane ({100}) the piezo-Hall effect is isotropic, meaning that rotating the Hall device on the plane will not modify the relationship between stress and sensitivity change.

Because the silicon die and the plastic compounds used to package sensors have different expansion coefficients, as soon as the molten plastic compound applied over the die begins to cool a stress will appear in the silicon-package interface. The resulting stress will change with the operating temperature, causing the Hall plate sensitivity to vary due to the piezo-Hall effect [39].

3.4 Effect of Humidity on Stress

The plastic compounds used to package integrated circuits (and most magnetic sensors) are non-hermetic [40]. This causes the package to absorb moisture and swell in high humidity conditions [4], changing the stress seen by the silicon chip, and thus causing the Hall plate sensitivity to be altered [3, 5] due to the piezo-Hall effect. Both [3] and [5] present data that confirms the effect of humidity on the sensitivity stability, but no detailed measurements of the phenomenon have been done to date. In this work, the transient behavior, the reversibility and repeatability of the moisture absorption are investigated.

Commercial off-the-shelf Hall sensors have been used for this set of measurements. The plastic compound used to package these parts creates a compressive (negative) stress on the surface of the die at 25°C due to the larger thermal expansion coefficient of the plastic compound compared to the silicon die. Before each of the tests, the sensor to be measured is placed in a temperature chamber at 150°C for several days, with the objective of removing any moisture from the package. The magnetic field necessary to detect sensitivity changes is generated with a permanent magnet attached to the rear face of the sensor (see Figure 3.8). Glue is applied between the side faces of the

magnet and the back face of the sensor, being very careful to keep the contact surface between the magnet and sensor free of glue. It is assumed that the magnetic field generated by the permanent magnet will not be affected by the ambient humidity conditions.

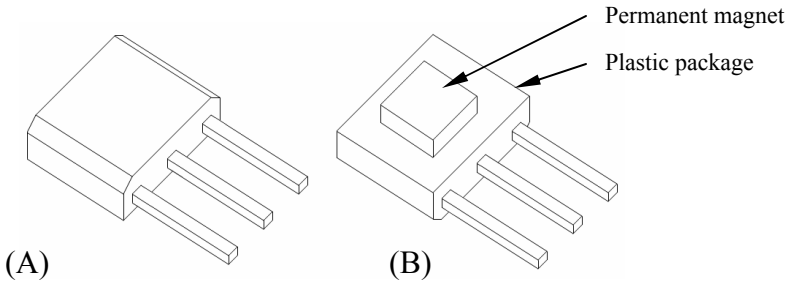

Figure 3.8 - *Magnetic sensor with permanent magnet attached to its back side. Front (A). Back (B).*

In a first experiment, the sample is first placed in a 90% relative humidity environment at 25°C for ten days, taking measurements every 30 minutes. Then, the moisture is removed from the package and the part is measured again in a 90% RH environment at 75°C.

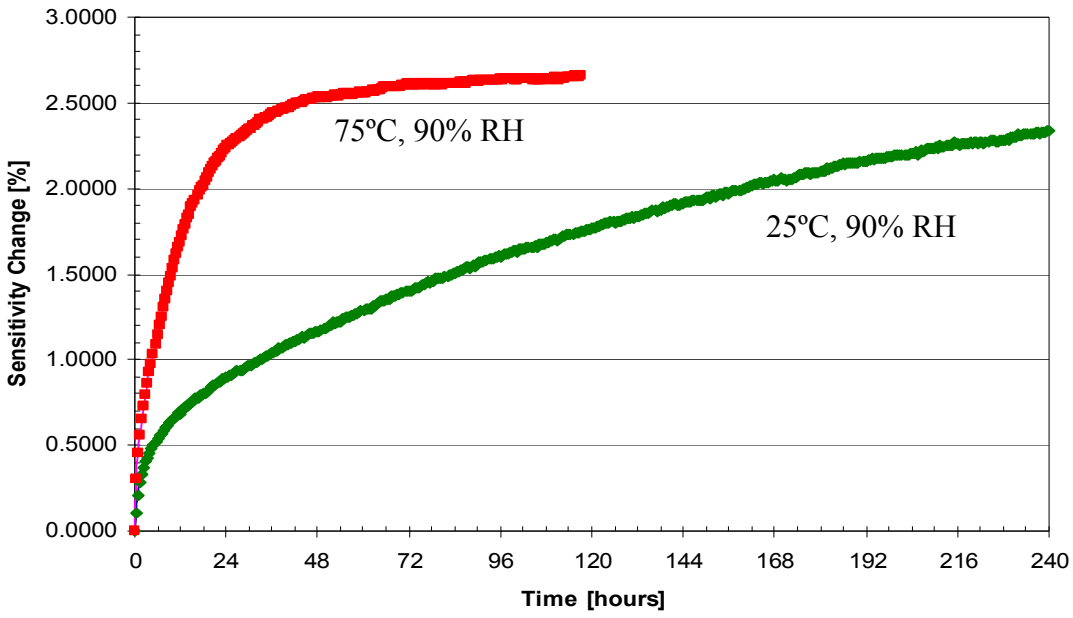

Figure 3.9 - *Sensitivity change of an initially "dry" sensor exposed to 90% RH at 25°C and 75°C. Moisture was removed from the package between cycles.*

Figure 3.9 shows the results of this test. As it can be seen, the operating temperature greatly affects the rate of sensitivity change in the Hall sensor. The positive sensitivity drift means that the package is swelling, causing the compressive (negative) stress in the silicon die to be reduced. The drift in the sensitivity will stabilize at above 2.5%. Depending on the application this sensitivity change can be significant.

In a second test, a Hall sensor is placed in the humidity chamber at 25°C, 90% RH for 10 days. Afterwards, the relative humidity is set to 45% for another 10 days. Finally the relative humidity is set back to 90%. Figure 3.10 shows the resulting sensitivity change over time for this experiment.

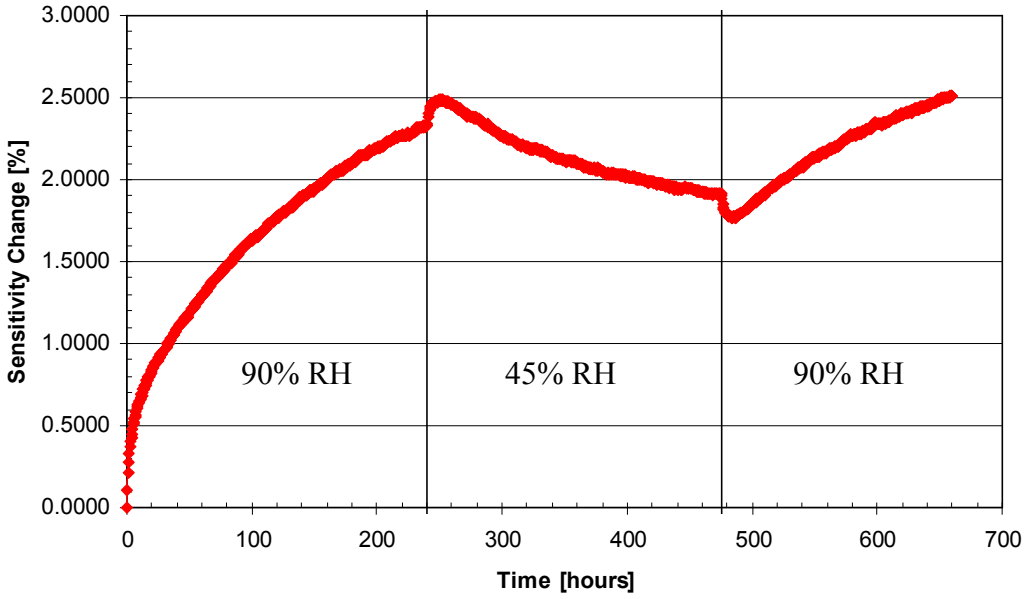

Figure 3.10 - *Sensitivity change of an initially "dry" sensor exposed sequentially to 90% RH, 45% RH and 90% RH, at 25°C.*

The sensitivity of the Hall sensor increases while the environment is set to 90% relative humidity. Once the humidity is reduced to 45% RH, the sensitivity starts to decrease. Finally, the sensitivity will continue increasing once the humidity is set back to 90%. This experiment confirms that the absorption of moisture by the plastic package is a

reversible effect. It is noted that signal overshoots appear when the relative humidity is changed from 90% to 45% and back again to 90%. The environmental chamber settling time is less than 30 minutes, but the overshoot length scale is about one day. An explanation for this effect is being investigated, but at this point the cause remains unknown.

The same experiment was repeated at 75°C. The rate of moisture absorption by the plastic package at this temperature is much faster than at 25°C, which helps to appreciate more clearly the absorption and desorption processes (see Figure 3.11). It is interesting to see that in this test the overshoots are not present.

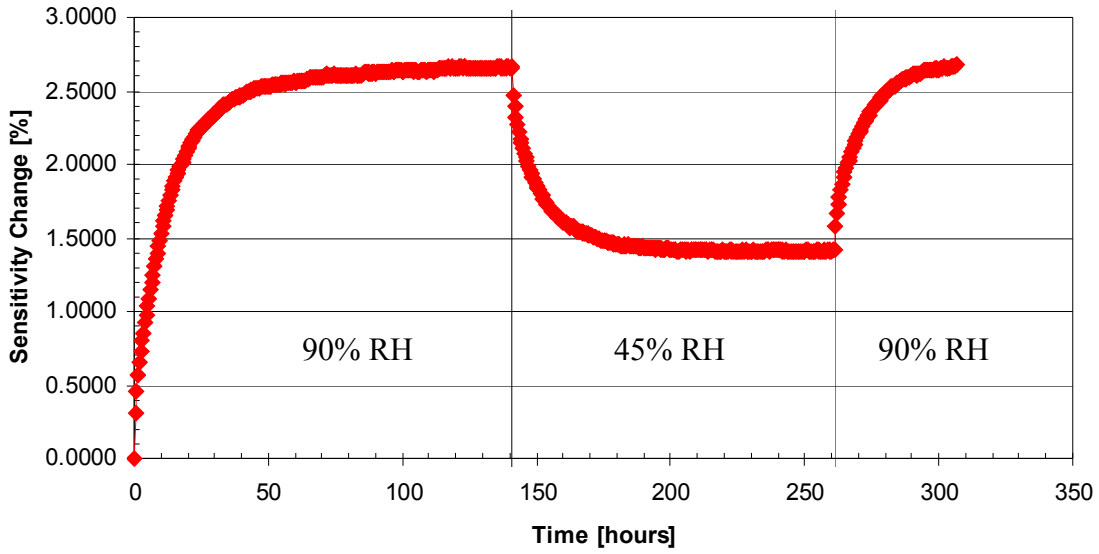

Figure 3.11 - *Sensitivity change of an initially "dry" sensor exposed sequentially to 90% RH, 45% RH and 90% RH, at 75°C.*

In a final experiment, a sensor is first placed in a high humidity environment (90% RH) at 25°C. After approximately four days, the temperature is raised to 150°C for two days to drive the moisture out of the package. Finally, the temperature is reduced

again to 25°C, and the humidity set to 90% RH. The resulting drift in the sensitivity can be seen in Figure 3.12.

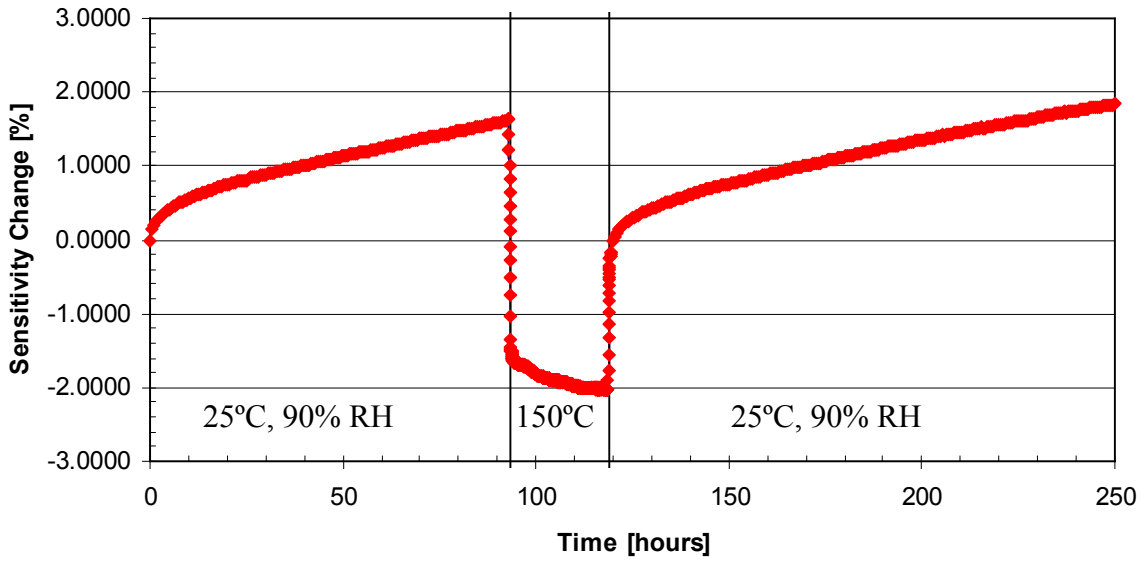

Figure 3.12 - *Sensitivity change of an initially "dry" sensor exposed sequentially to 90% RH 25°C; 150°C and 90% RH 25°C.*

The Hall sensor and the field generated by the permanent magnet both have small temperature coefficients, which explain the drop in sensitivity when going from 25°C to 150°C. Figure 3.13 compares the change in sensitivity over time for the initial part of this experiment at 25°C (series one), the sensitivity drift after staying at 150°C (series two), and a third series, which corresponds to a new measurement performed with the same device two months later. Two important conclusions can be obtained from this test. First, the rate of sensitivity change and thus the rate of moisture absorption by the plastic package for a given part is a deterministic and repeatable effect. Second, for the molding compound used for these sensors, is that a time period of two days at 150°C is sufficient to drive all the moisture out of the package.

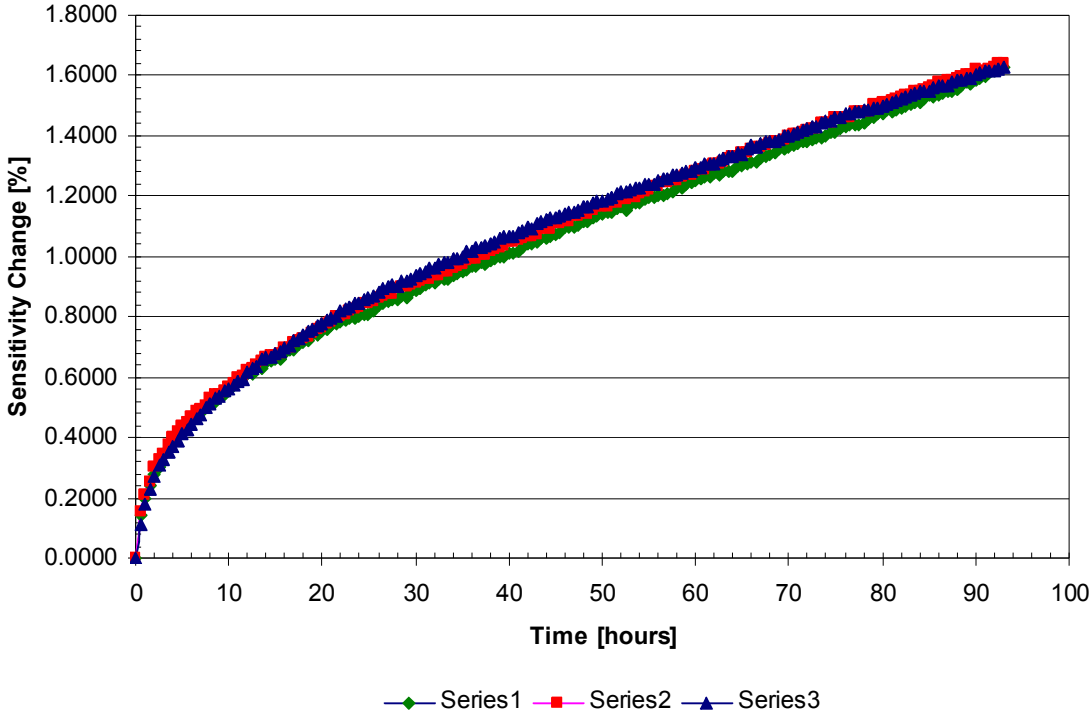

Figure 3.13 - *Three moisture absorption cycles at 90% RH, 25°C for the same part, showing the repeatability of the sensitivity drift.*

CHAPTER IV

COMPENSATION BY MECHANICAL STRESS FEEDBACK

4.1 Introduction

The main contribution to the long-term drift of the sensitivity of Hall sensors is caused by changes in the stress conditions at the die-package interface [3]. At constant temperature, these stress changes are mainly due to variations in the moisture content of the plastic package, and to the viscoelastic properties of the package material resulting in a time dependent stress to strain response.

The stress on the die surface can typically be considered to be homogeneous over small distances [41], so that resistors placed close to the Hall plate can be employed to measure the stress change via the piezoresistive effect. This information can then be used to compensate the Hall sensitivity drift [42, 43].

The main challenge of using the piezoresistive effect to detect stress changes is related to the fact that the resistance of integrated resistors does not only depend on stress, but also on temperature. In order to know if a change in resistance is due to stress or temperature variations, a temperature sensing mechanism must be implemented. The information obtained from the temperature sensor can then be used to cancel out temperature-induced resistance changes.

The objective of this chapter is to find out if this type of sensitivity compensation scheme can be successfully implemented. In the following sections a stress sensor is proposed, a test-chip is designed to prove the theory behind the compensation strategy and in the final section a system implementation is proposed.

4.2 Stress Sensor Implementation

4.2.1 Sensor Design

A Hall device implemented in the {100} plane is sensitive to the sum of the in-plane normal stresses $\sigma_x + \sigma_y$ (see Section 3.4.2), so the stress sensor should be designed to respond to the sum of in-plane normal stresses as well. As it will be shown below, a group of two series resistors of the same value laid out in orthogonal directions (L shape) [44] fulfill this requisite, regardless of the group orientation in the {100} plane.

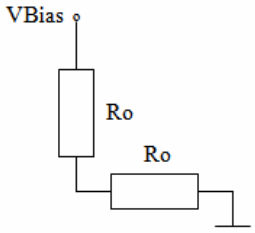

Figure 4.1 - *Resistor L configuration.*

The total resistance for the resistor group shown in Figure 4.1 is given by:

$$R = Ro\left[1 + \pi_{L1}\sigma_{L1} + \pi_{T1}\sigma_{T1}\right] + Ro\left[1 + \pi_{L2}\sigma_{L2} + \pi_{T2}\sigma_{T2}\right] \tag{4.1}$$

If both resistors are in close proximity, we can assume:

$$\sigma_{L1} = \sigma_{T2} \tag{4.2}$$

$$\sigma_{T1} = \sigma_{L2} \tag{4.3}$$

Thus, the series resistance can be rewritten as:

$$R = Ro\left[2 + \sigma_{L1}(\pi_{L1} + \pi_{T2}) + \sigma_{T1}(\pi_{T1} + \pi_{L2})\right] \tag{4.4}$$

The piezoresistive coefficients for these two resistors located on a {100} wafer plane (see Section 3.4.1) are:

$$\pi_{L1} = \pi_{11} - 2(\pi_{11} - \pi_{12} - \pi_{44})\cos^2\phi\sin^2\phi \tag{4.5}$$

$$\pi_{T1} = \pi_{12} + 2(\pi_{11} - \pi_{12} - \pi_{44})\cos^2\phi\sin^2\phi \tag{4.6}$$

$$\pi_{L2} = \pi_{11} - 2(\pi_{11} - \pi_{12} - \pi_{44})\cos^2(\phi + 90°)\sin^2(\phi + 90°) \tag{4.7}$$

$$\pi_{T2} = \pi_{12} + 2(\pi_{11} - \pi_{12} - \pi_{44})\cos^2(\phi + 90°)\sin^2(\phi + 90°), \tag{4.8}$$

where ϕ is the angle with respect to the <100> direction in the {100} plane. With:

$$\cos^2\phi\sin^2\phi = \cos^2(\phi + 90°)\sin^2(\phi + 90°), \tag{4.9}$$

we find:

$$\pi_{L1} + \pi_{T2} = \pi_{11} + \pi_{12} \tag{4.10}$$

$$\pi_{T1} + \pi_{L2} = \pi_{11} + \pi_{12} \tag{4.11}$$

$$R = 2Ro\left[1 + (\sigma_{L1} + \sigma_{T1})\frac{\pi_{11} + \pi_{12}}{2}\right] \tag{4.12}$$

It has been shown in [45] that the sum of the in-plane normal stresses is invariant to rotations in the wafer plane, so Eq. (4.12) can be re-written as:

$$R = 2Ro\left[1 + (\sigma_x + \sigma_y)\frac{\pi_{11} + \pi_{12}}{2}\right], \tag{4.13}$$

which proves the previous assertion. The change in resistance is thus given by:

$$\frac{\Delta R}{R} = (\sigma_x + \sigma_y)\frac{\pi_{11} + \pi_{12}}{2} \tag{4.14}$$

The orientation of the resistor group in the {100} plane does not modify the resistance change for a given in-plane stress.

4.2.2 Sensor Implementation

Various resistor types can be implemented in silicon to empirically test their sensitivity to stress fluctuations. It has been decided to use N-Epi resistors, P-Well

resistors and P+ resistors. Their expected change in resistance per GPa of stress can be calculated from Eq. (4.14), and is shown in Table 4.1. The N- and P-type piezoresistive coefficients are reproduced from Table 3.1.

Table 4.1 - *N- and P-type piezoresistive coefficients and variation in resistance per gigapascal for various types of resistors at 300K laid out as in Figure 4.1.*

Resistor	π_{11}	π_{12}	$\Delta R/R$
N-type Epi Resistor	-102.2 x 10^{-11} 1/Pa	53.4 x 10^{-11} 1/Pa	-24.4% / GPa
P-type Well Resistor	6.6 x 10^{-11} 1/Pa	-1.1 x 10^{-11} 1/Pa	2.8% / GPa
P+ Resistor	3.3 x 10^{-11} 1/Pa	-0.55 x 10^{-11} 1/Pa	1.3% / GPa

Higher doping concentrations cause a reduction in the piezoresistive coefficients (see Section 3.4.1). For this reason the piezoresistive coefficients of the P+ resistor are reduced by a factor of 0.5 with respect to a lightly doped P-type resistor.

4.3 Test Chip Implementation

4.3.1 Test Chip Design

Commercial Hall sensors, as most integrated circuits in the market, are sold in through-hole and surface mount packages. Single-in-line packages (SIP) with three and four pins are the most common through-hole implementation for Hall sensors.

In order to investigate the effects of moisture absorption, the test-chip must be encapsulated in a plastic package. A four-pin SIP is used to package the die in this work. Two of the package's pins are needed for the positive and negative supply lines, so only two pins are available as outputs. If we take into consideration that the Hall plate and the

integrated resistors will need to be measured, the number of output pins is not enough for a direct device-to-output connection, and a clever implementation will be needed. The proposed solution is to use an internal state machine, programmed via the positive supply pin (see Fig. 4.2). The operating voltage for this experiment will be 3V, so a 6V pulse can be used to signal a change in the state machine.

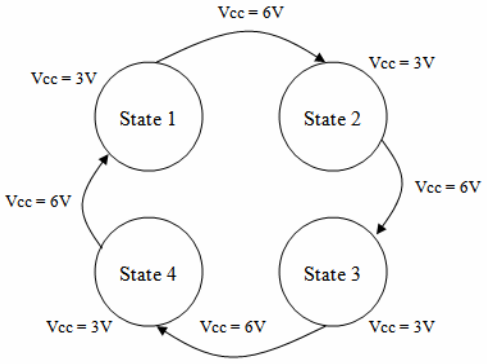

Figure 4.2 - *Example of the proposed state machine.*

For the Hall plate related measurements, we want to distinguish the sensor output caused by the external magnetic field from the Hall plate offset and the amplifier offset. This can be accomplished by modifying the connections between the Hall plate and the amplifier and the direction of the bias current in the Hall device, as shown in Fig. 4.3 (see also Section 2.2.5.2). The differential output signal for each of the states will be:

$$\Delta Vo_1 = Av\ \left(VB + VoffHall + VoffAmp\right) \tag{4.15}$$

$$\Delta Vo_2 = Av\ \left(VB - VoffHall + VoffAmp\right) \tag{4.16}$$

$$\Delta Vo_3 = Av\ \left(-VB - VoffHall + VoffAmp\right) \tag{4.17}$$

$$\Delta Vo_4 = Av\ \left(-VB + VoffHall + VoffAmp\right) \tag{4.18}$$

where *VB* is the signal due to the external magnetic field, *VoffAmp* is the amplifier offset and *VoffHall* is the Hall plate offset. *VB*, *VoffAmp* and *VoffHall* can be obtained from the output differential signals as follows:

$$VB = \frac{\Delta Vo2 - \Delta Vo3}{2} = \frac{\Delta Vo1 - \Delta Vo4}{2} \tag{4.19}$$

$$VoffAmp = \frac{\Delta Vo1 + \Delta Vo3}{2} = \frac{\Delta Vo2 + \Delta Vo4}{2} \tag{4.20}$$

$$VoffHall = \frac{\Delta Vo1 - \Delta Vo2}{2} = \frac{\Delta Vo4 - \Delta Vo3}{2} \tag{4.21}$$

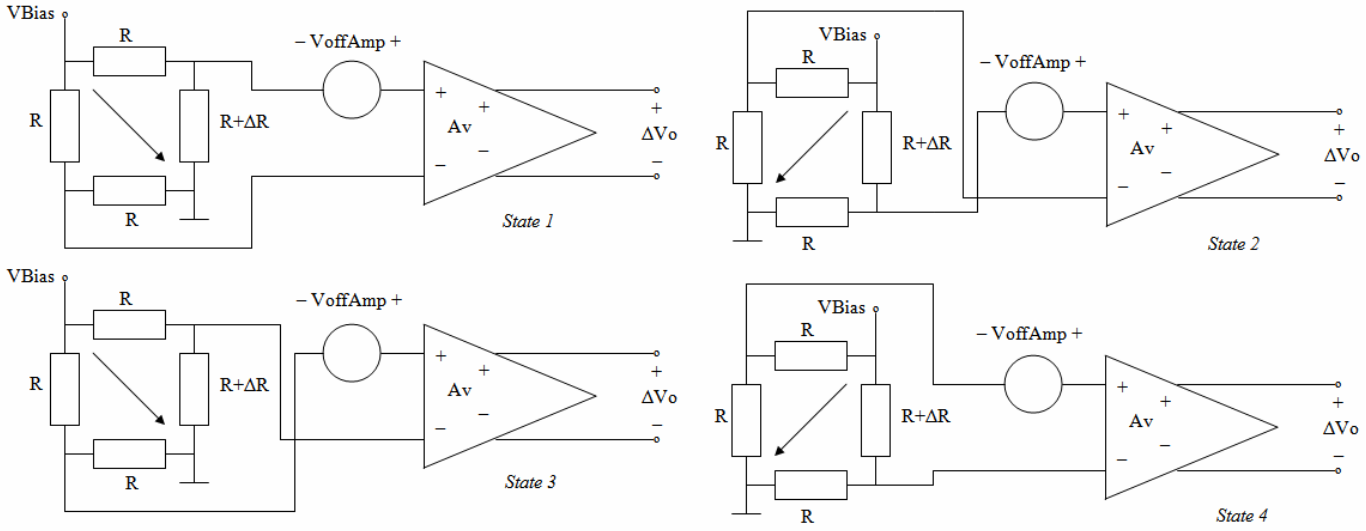

Figure 4.3 - *Electrical connections for the four states needed to recover the external magnetic field, amplifier offset and Hall plate offset. The Hall plates are represented as Wheatstone bridges to showcase their offset.*

Two different test configurations have been designed. The first one utilizes 160µm Hall plates and the second one Hall plates with 50µm side length. Each of the test chips has three different Hall plates: a quad Hall plate, and two single Hall plates, with one of them rotated 45 degrees with respect to the other. A total of 12 states will be required to implement this part of the system. The Hall plates in the test chips are

voltage-driven, because they are simpler to implement and their driving conditions are easier to control.

As stated in Section 4.2.2, N-Epi resistors, P-Well resistors and P+ resistors are implemented on the test chip. When selected by the state machine, one of their terminals is connected to one of the output pins, while the other terminal of the resistor "L" is connected to ground. To confirm Eq. (4.14) two groups of Epi resistors are implemented: one in the <100> direction and the other one in the <110> direction in the {100} plane.

The single Hall plate diagonal resistance is also made available at the output pins. In one state the two output pins are connected to one diagonal, and in the following state they are connected to the other Hall plate diagonal.

The test chips use a total of 16 states. Table 4.2 summarizes the device/signal available at the output terminals in each state, and its configuration.

Table 4.2 - *Summary of device and its configuration at the output pins for each of the 16 test chip states.*

State	1	2	3	4
Device	Quad Hall, 160 μm or 50 μm side			
Measurement	$\Delta V = Av(VB + Voff_{Hall} + Voff_{Amp})$	$\Delta V = Av(VB - Voff_{Hall} + Voff_{Amp}$	$\Delta V = Av(- VB - Voff_{Hall} + Voff_{Amp})$	$\Delta V = Av(- VB - Voff_{Hall} + Voff_{Amp})$

State	5	6	7	8
Device	Single Hall, 160 μm or 50 μm side			
Measurement	$\Delta V = Av(VB + Voff_{Hall} + Voff_{Amp})$	$\Delta V = Av(VB - Voff_{Hall} + Voff_{Amp})$	$\Delta V = Av(- VB - Voff_{Hall} + Voff_{Amp})$	$\Delta V = Av(- VB - Voff_{Hall} + Voff_{Amp})$

State	9	10	11	12
Device	Single Hall, 160 μm or 50 μm side, tilted 45 degrees			
Measurement	$\Delta V = Av(VB + Voff_{Hall} + Voff_{Amp})$	$\Delta V = Av(VB - Voff_{Hall} + Voff_{Amp})$	$\Delta V = - Av.VResDiv + Voff_{Amp}$	$\Delta V = Av.VResDiv + Voff_{Amp}$

State	13	14	15	16
Device	Single Hall 1st diagonal	Single Hall 2nd diagonal	Epi Resistors	P+ Resistors Pwell Resistors
Measurement	Resistance between output terminals	Resistance between output terminals	Resistor Pair <100> to Vout+ Resistor Pair <110> to Vout-	P+ Resistors to Vout+ Pwell Resistors to Vout-

4.3.2 Silicon Implementation

Figure 4.4 shows a simplified representation of the implemented system. The stress test chips are comprised, as mentioned in the previous section, of Hall plates, integrated resistors, an amplifier and several supporting blocks. The Bias Reference block is used to generate temperature independent currents to bias the rest of the blocks and a reference voltage to establish the amplifier's output common mode voltage. The Bandgap block provides a constant voltage, independent of temperature and VCC, to be used as the programming voltage reference. The VCC programming block compares this reference voltage with VCC and changes the state of its output when the programming voltage has been reached, causing the system to move to the next state. The Select LV block provides the signaling required for each of the states. The power and signal switches blocks are used to connect the Hall plates with the amplifier as needed. The following subsections briefly describe each of the blocks. Simulations of these blocks were performed with Cadence, an IC design software widely used by the industry.

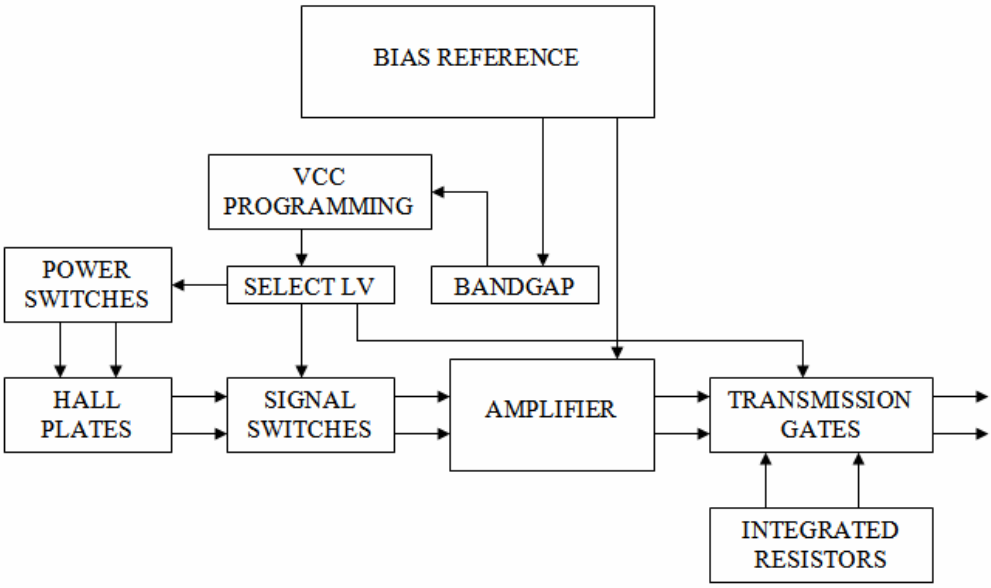

Figure 4.4 - *Simplified block diagram.*

4.3.2.1 Bias Reference Block

The Bias Reference circuit is used to generate a current that is, to some degree, constant over temperature and a reference voltage proportional to VCC to set the common mode at the output of the amplifier. The schematic view of the block is presented in Figure 4.5. Because the response of the circuits being biased by this block are independent of the actual value of the current being fed into them, a simple biasing structure was implemented.

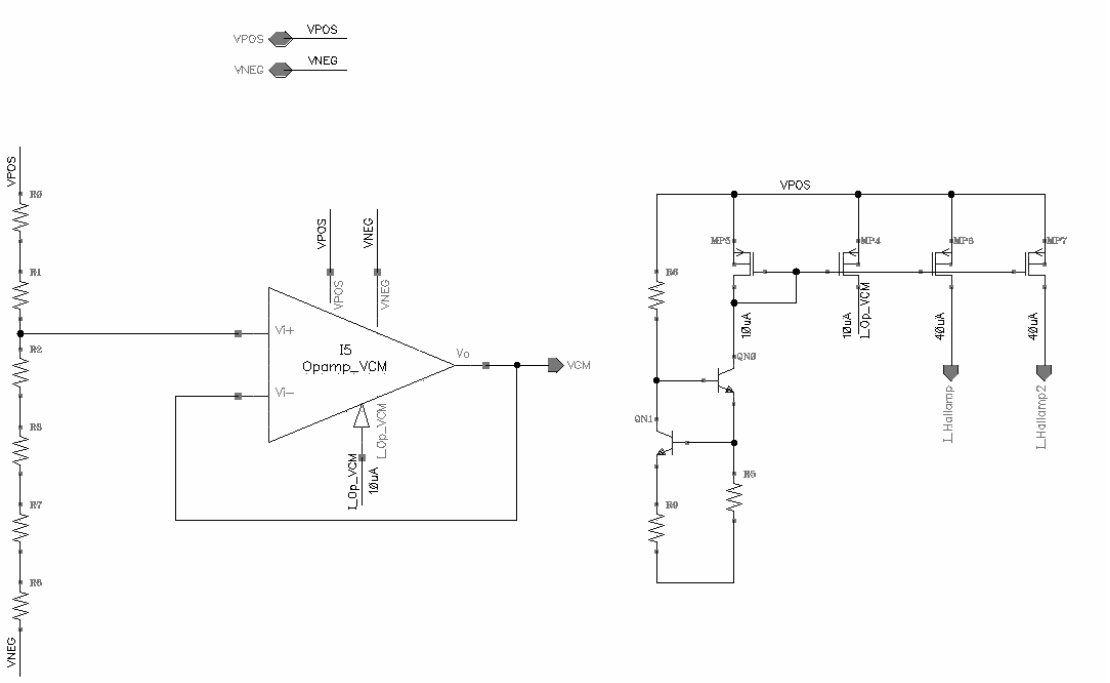

Figure 4.5 *- Schematic of Bias Reference Block.*

The simulations over temperature and for process corners show that the output bias currents vary approximately ± 20% due to the process variations, which is a satisfactory number for this application.

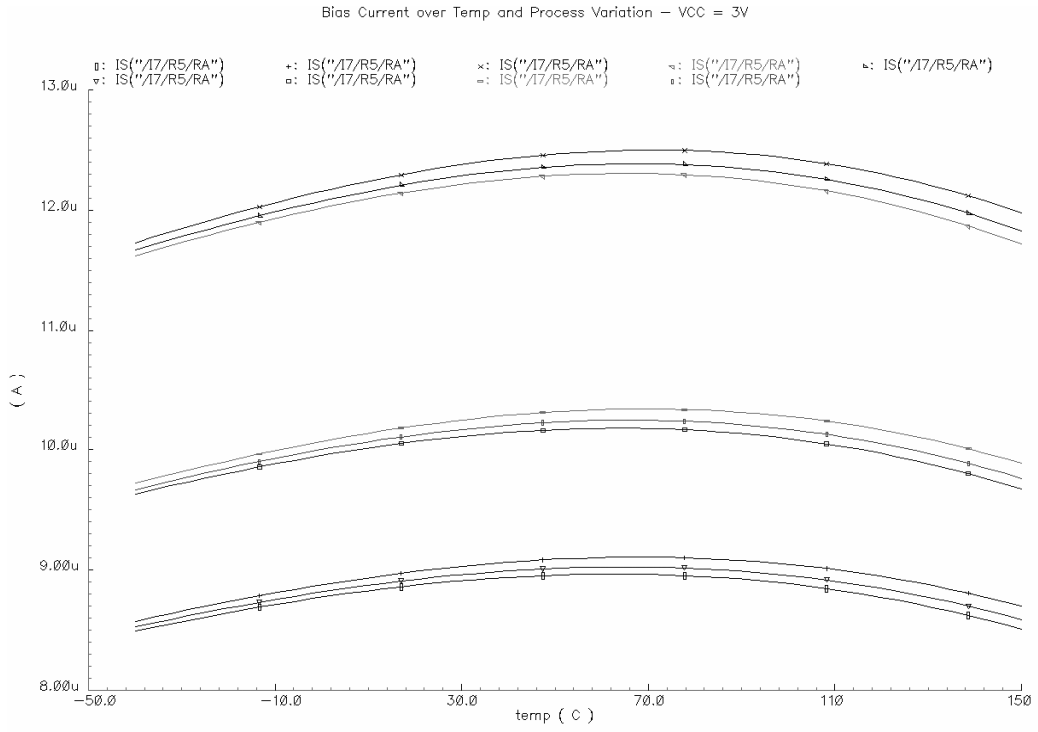

Figure 4.6 *- Bias current as a function of temperature, including effects of process variations. Nominal value = 10μA, Vcc=3V.*

4.3.2.2 Bandgap Block

The Bangap block is used to generate a stable, temperature independent, reference voltage for the Vcc programming block. A small constant current is injected into the circuit to assure proper startup. The value of the resistors R1 and R2 in Figure 4.7 were adjusted to provide a flat response over temperature at the output of the Vcc Programming block (see Figures 4.10, 4.11 and 4.12).

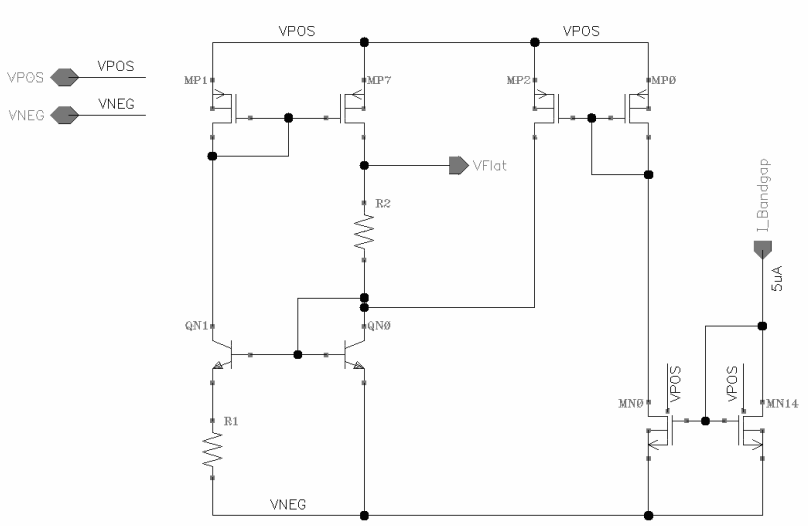

Figure 4.7 *- Schematic of Bandgap Block.*

4.3.2.3 Vcc Programming Block

The Vcc programming block (Figure 4.8) compares a voltage proportional to Vcc with the reference voltage obtained from the Bandgap block. The result of this comparison in fed into the Select LV block, which toggles the system to the next state. A Schmitt-trigger was implemented to avoid chatter during transients.

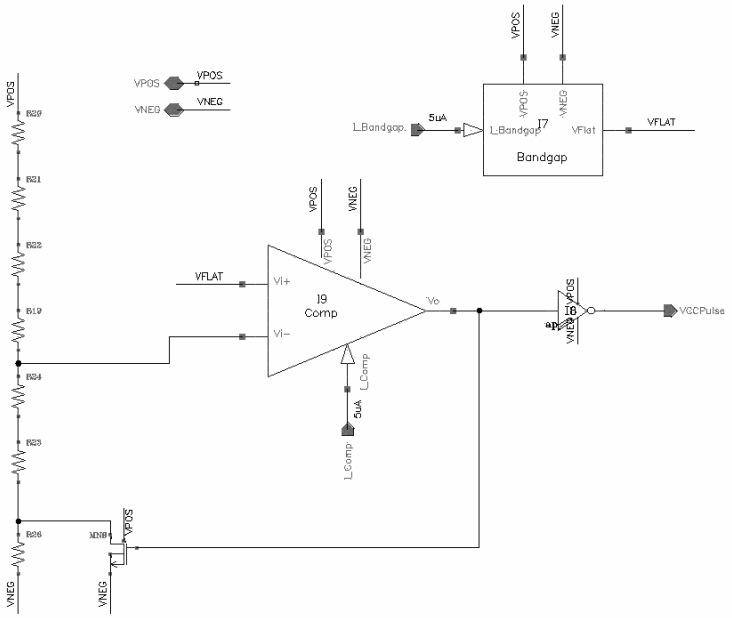

Figure 4.8 *- Schematic of Vcc Programming Block.*

The comparator circuit (Fig. 4.9), used in the Vcc Programming Block, has an integrated delay to prevent noise in the Vcc line to cause false triggers. Along with the Schmitt-trigger circuit, this creates robust protection against unwanted pulses.

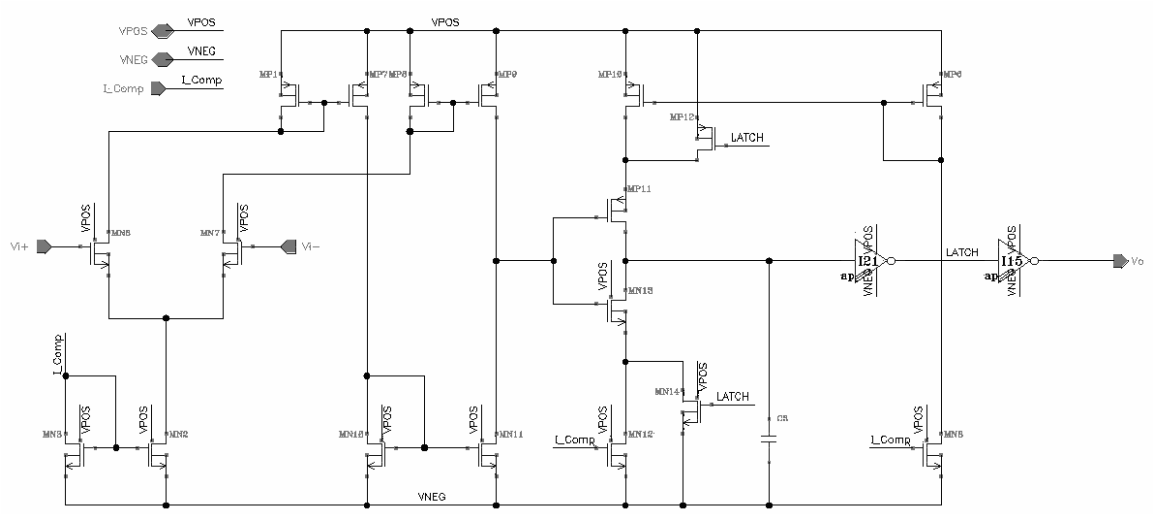

Figure 4.9 *- Schematic of Comparator Block.*

Figures 4.10, 4.11 and 4.12 show the Vcc Programming Block output versus Vcc over temperature and process parameters. The Vcc Pulse signal is "on" when Vcc is higher than Vc_{High} (the Schmitt trigger high), and is "off" when Vcc is lower than Vc_{Low} (the Schmitt trigger low).

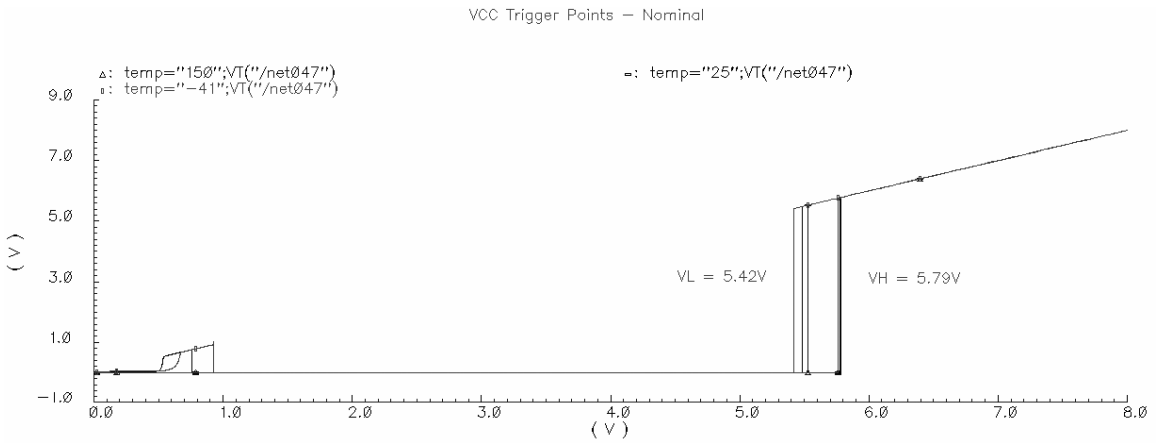

Figure 4.10 *- Vcc sweep with nominal process parameters at -40°C, 25°C and 150°C. Vc_{High} = 5.79V, Vc_{Low} = 5.42V.*

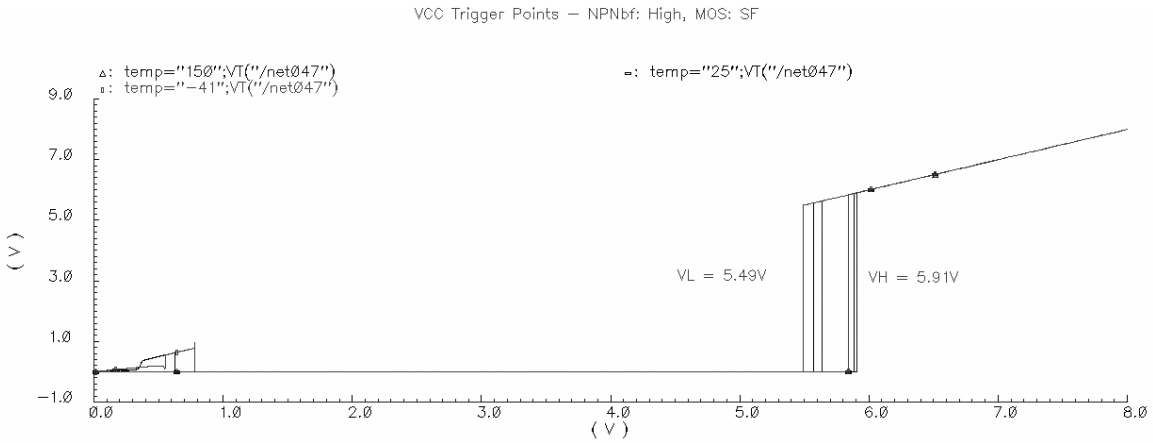

Figure 4.11 - *Vcc sweep with NPN β High, MOS SF at -40°C, 25°C and 150°C. Vc_{High} = 5.91V, Vc_{Low} = 5.49V.*

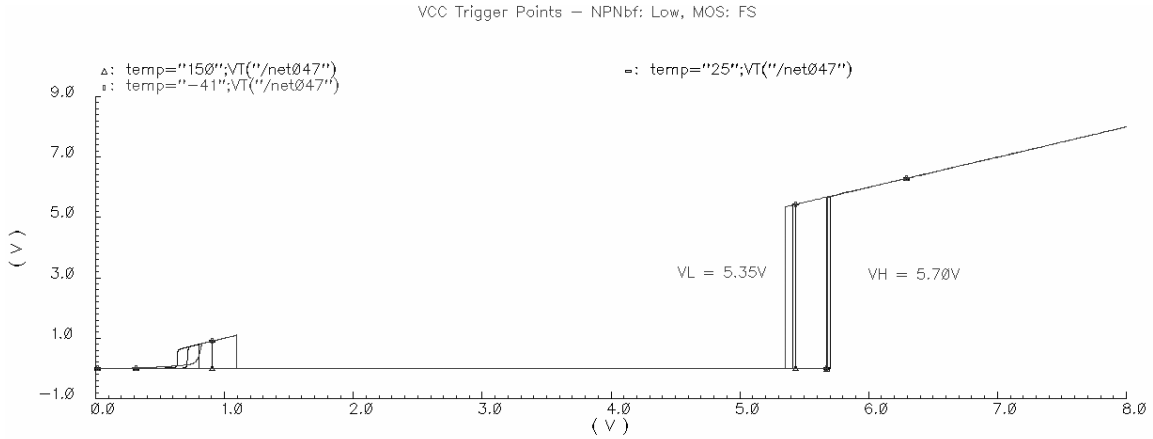

Figure 4.12 - *Vcc sweep with NPN β Low, MOS FS at -40°C, 25°C and 150°C. Vc_{High} = 5.70V, Vc_{Low} = 5.35V*

4.3.2.4 Hall Amplifier Block

The amplifier used in this project is of the open-loop type. Its gain is defined from the ratio of the output to input resistors. The gain has been set to 50, taking into consideration that the maximum signal at the amplifier input must not saturate its output. The design of the amplifier is proprietary and cannot be disclosed in this work.

4.3.2.5 Select LV Block

This block controls the selection of the device to be connected to the output pins with the pulses received from the VCC Programming Block. It consists of four flip-flops to establish the 16 system states and logic circuitry to define the device configuration (see Fig.4.13).

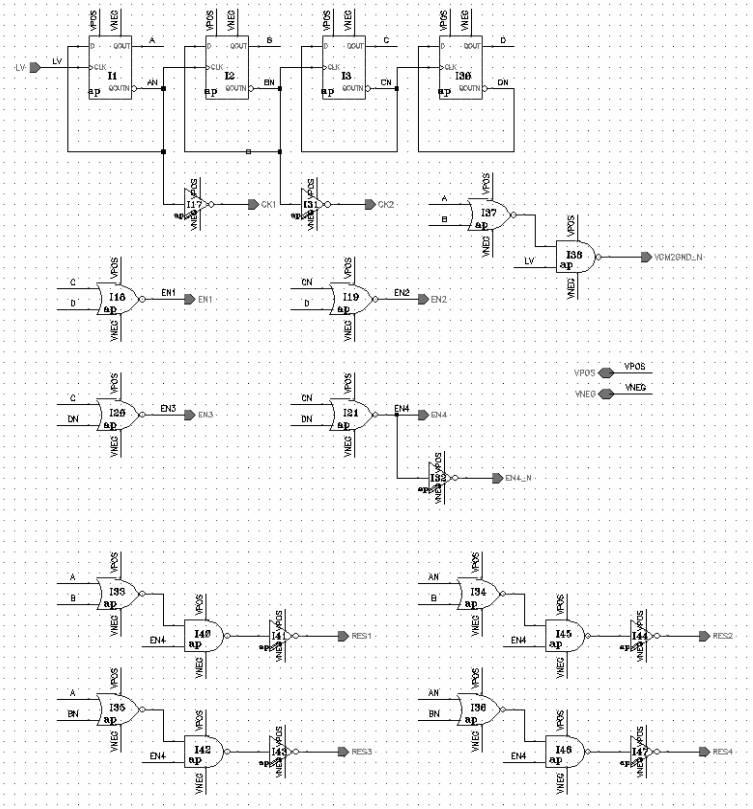

Figure 4.13 *- Schematic of Select LV Block.*

4.3.2.6 Hall Power Switches Block

This block is used to connect the Hall plate to the Vcc and ground lines. When the quad Hall plate and the 45° tilted single Hall plate are not selected, two of its terminals are connected to ground via this block. For the single Hall plate, on the contrary, when it is not selected all four transistors (see Fig. 4.14) are turned off to allow the Hall plate resistance to be measured at the output pins (see Table 4.2).

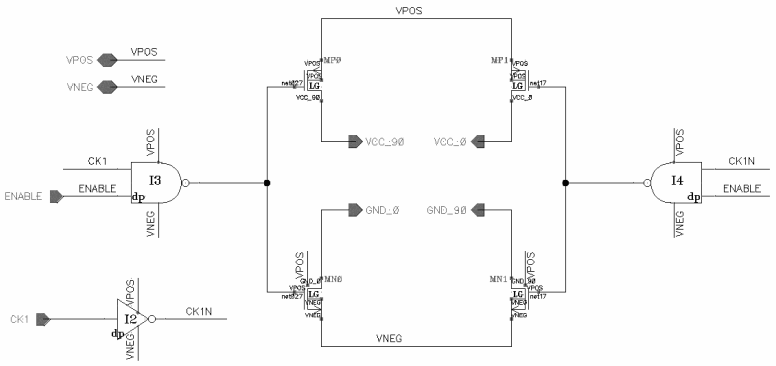

Figure 4.14 *- Schematic of Hall Power Block.*

4.3.2.7 Signal Switches Block

This block is used to connect the Hall plate to the amplifier. The complexity of the block is due to the fact that the external magnetic field, the Hall plate offset and the amplifier offset will need to be measured. Since there is almost no current flow, the voltage drop across the transmission gates is very small.

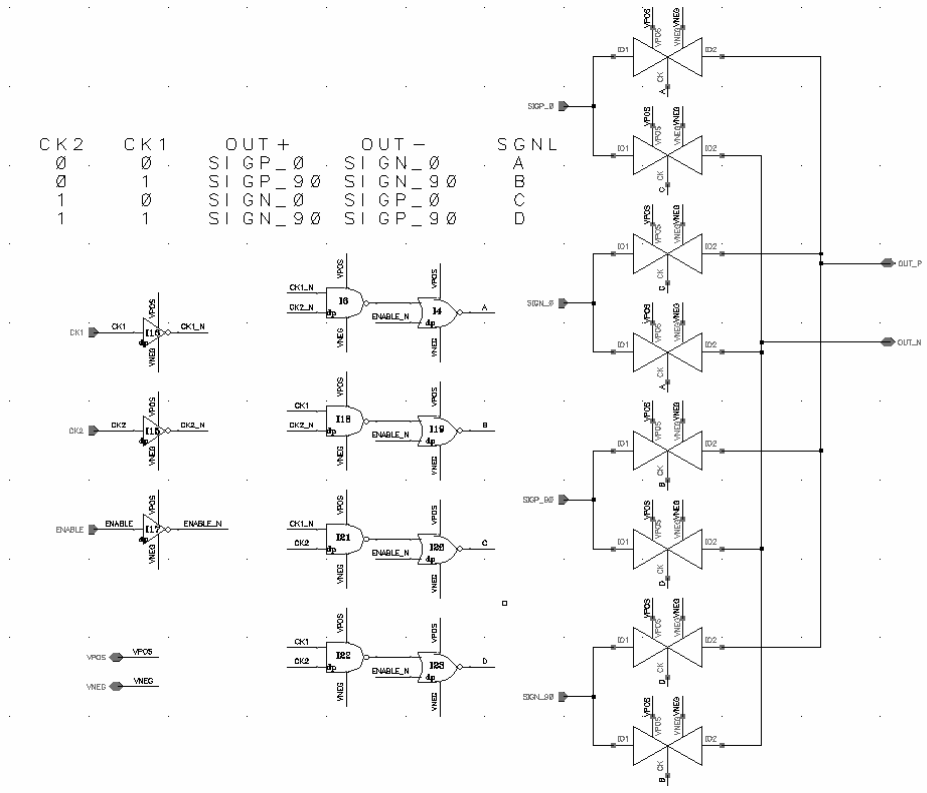

Figure 4.15 *- Schematic of Signal Switches Block.*

4.3.2.8 Schematic View, Layout View and Silicon Photographs

The test chip schematic and layout views are presented in Figure 4.16. The Hall plates, integrated resistors and Hall amplifier can be clearly seen. Figure 4.17 show photographs of the silicon chips.

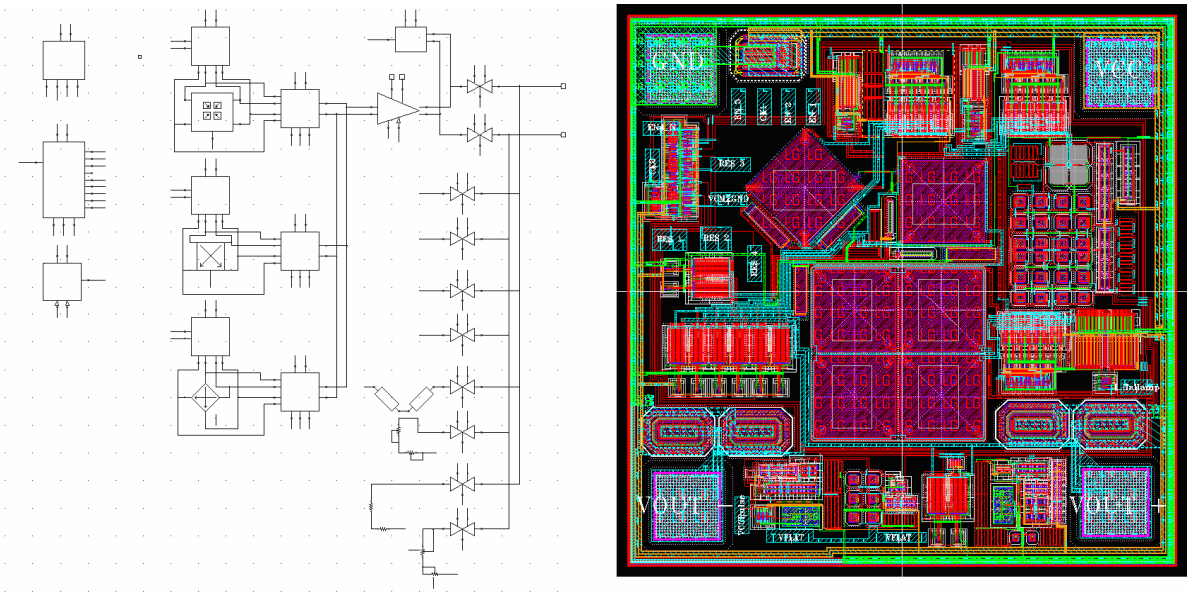

Figure 4.16 *- Top Level schematic and layout views of the test chip with 160µm Hall plates.*

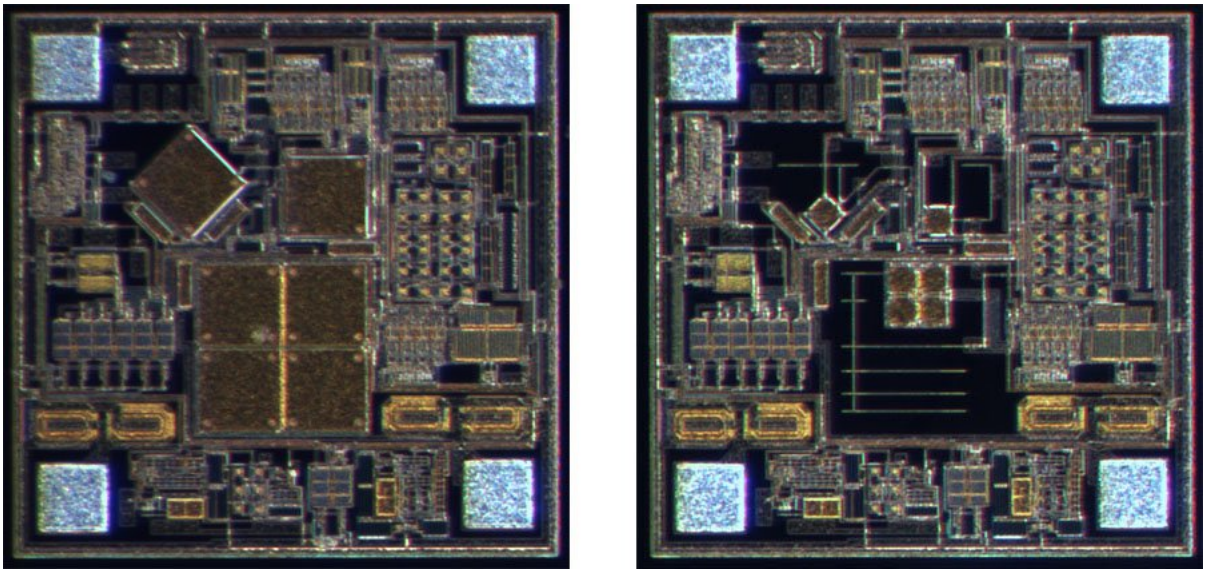

(A) (B)

Figure 4.17 *- Photographs of the test chips with 160µm Hall plates (A) and 50µm Hall plates (B).*

4.4 Measurements Results

In order to measure the effect of humidity changes on the Hall sensor sensitivity, the test chips must be encapsulated in plastic packages. In addition, ceramic packages were used to test the system without the stress created by the plastic compound. Figure 4.18 shows a picture of both packages.

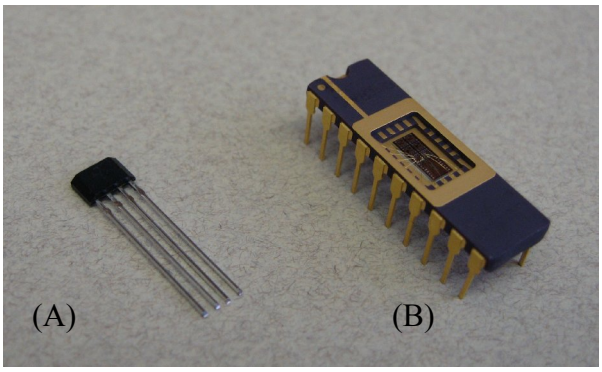

Figure 4.18 - *Packaged test chips. Plastic package (A). Ceramic package (B).*

4.4.1 Hall Plate Sensitivity and Linearity

The first set of measurements performed on the encapsulated parts was intended to test the functionality of the sensors. For this reason the sensitivity of the 160µm and 50µm Hall plates was measured at 25°C using a using a FW BELL 5180 Gaussmeter with the magnetic field generated by as system similar to the one depicted in Figure 4.19.

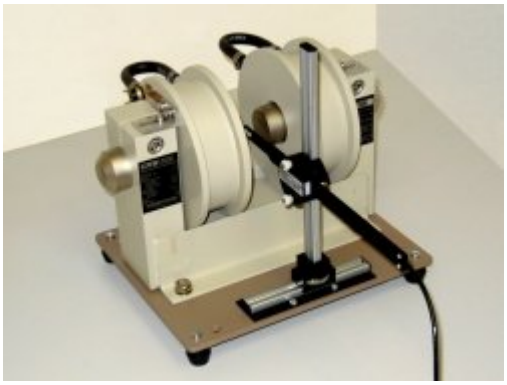

Figure 4.19 - *GMW Model 3470 Magnet System.*

The measurements of the sensitivity at room temperature with a biasing voltage of 3V and a constant magnetic field of 500G (50mT) are shown in table 4.3. Due to the limited amount of chips no statistical information is presented.

Table 4.3 - *Magnetic sensitivity for different Hall plate sizes and packages with Vcc=3V at 25°C.*

Size	Type of Hall Plate	Ceramic Package	Plastic Package
160µm	Single Hall Plate	19.9 uV/G	17.1 uV/G
	Quad Hall Plate	19.6 uV/G	17.0 uV/G
50µm	Single Hall Plate	18.3 uV/G	15.6 uV/G
	Quad Hall Plate	18.0 uV/G	15.4 uV/G

Table 4.3 indicates that the sensitivity of the Quad Hall plate is always slightly smaller than the one of an identical Single Hall plate. The current needed to drive a Quad Hall plate is four times larger than for a Single Hall plate, and the internal switches used to commutate the Hall plates were scaled up to cope with the increased current and assure an insignificant voltage drop over them. The fact that the sensitivity is smaller for the Quad Hall plates when compared with the Single Hall plates means that the effective voltage seen by the Quad Hall plate is slightly less than the voltage seen by the Single Hall plate and the precautions taken during the switch design might not have been enough.

The sensitivity of the plastic packaged parts is considerably lower than that of the ceramic packaged parts because of stress effects. In particular, this means that the plastic compound is generating a compressive force on the Hall plate.

After this first test all the following measurements were performed with the plastic encapsulated devices. This is due to the fact that we are interested on the effect of humidity, which can only be measured with these parts. The linearity of the magnetic sensors was tested with magnetic fields up to 1000G (0.1T). Figure 4.20 shows the results

obtained with the 160µm Hall plates, and Figure 4.21 shows the same data, but for the 50µm sensors. The linearity measurement (±0.1%) is limited primarily by the resolution of the Gaussmeter being used (FW BELL 5180 Hand Held Gaussmeter with 3 $^{2}/_{3}$ digits).

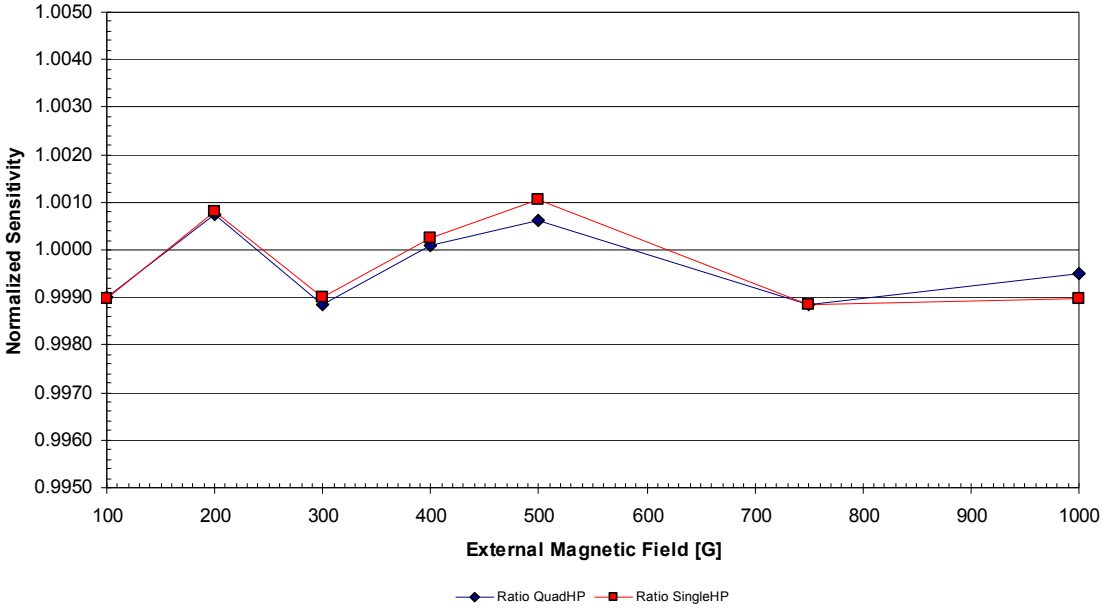

Figure 4.20 *- Sensitivity linearity of 160µm Hall plates.*

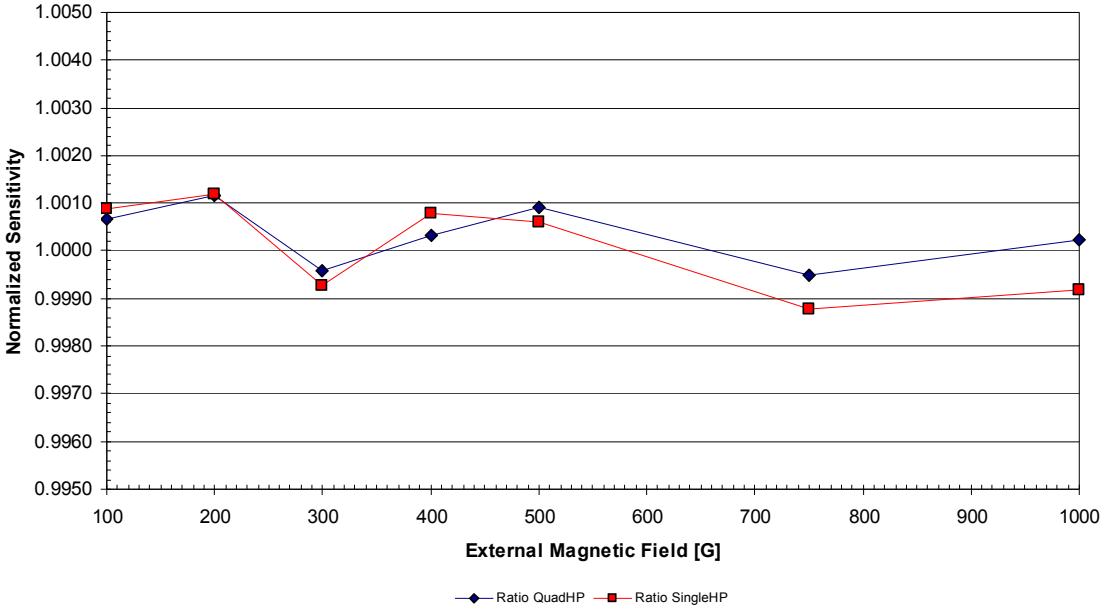

Figure 4.21 *- Sensitivity linearity of 50µm Hall plates.*

4.4.2 Temperature Dependence of Stress Sensors

It is the purpose of the stress compensation scheme to use the change in value of an integrated resistor pair to compensate for variations in the Hall sensitivity due to stress changes. For this reason it is important to know the drift of the resistors over temperature. Figure 4.22 shows the resistance change for various resistors measured from -40°C to 150°C, normalized at 25°C. Because the test chips are encapsulated in plastic packages, a change in temperature will cause the stress seen by the resistors to vary due to mismatched expansion coefficients, adding to the resistance change.

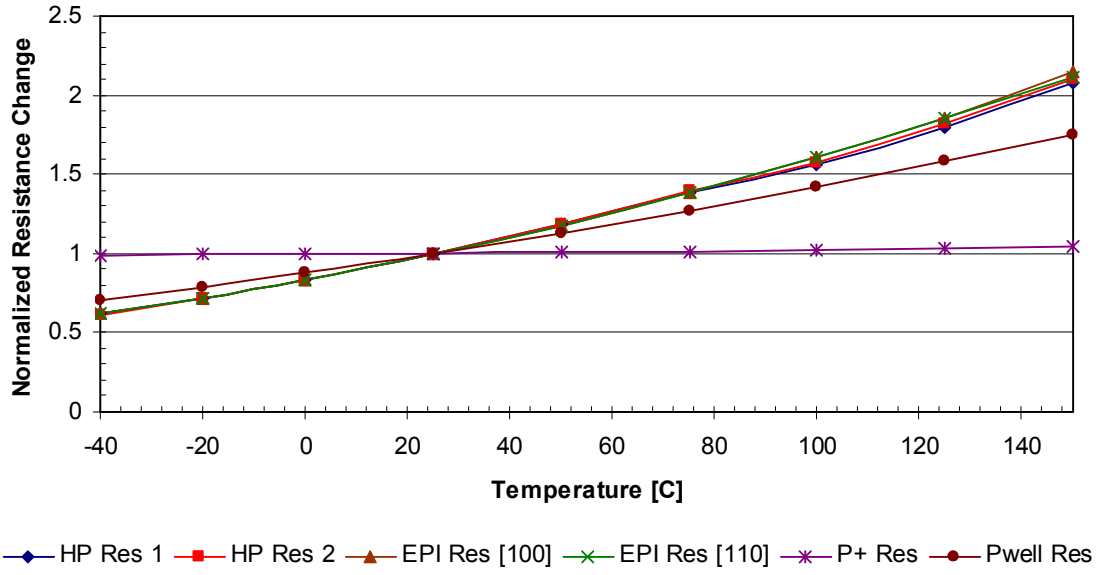

Figure 4.22 *- Resistance of the piezoresistors on the test chip as a function of temperature. (HP Res 1 and HP Res 2 denote the resistance of the Hall plate along the two diagonals).*

As expected the Epi resistors and the Hall plate diagonal resistance exhibit the same temperature behavior regardless of their orientation in the {100} plane. The Pwell resistor has a somewhat lower temperature drift than the Epi resistors. The highly doped P+ resistor value changes only 5% from -40°C to 150°C. This would make it a good

candidate for stress sensing, if it weren't for the fact that it has an order of magnitude less sensitivity to stress changes than the Epi resistors (see Table 4.1).

4.4.3 Temperature Dependence of the Hall plate Sensitivity

To obtain the sensitivity change over the operating temperature range, the plastic encapsulated Hall sensors were placed inside the environmental chamber with a permanent magnet placed on their back face, as in Figure 3.8. The voltage-driven sensitivity drift was extracted directly from the measurements, taking into account the temperature drift of the SmCo magnet (-0.03%/°C). The current-driven sensitivity drift was obtained from the voltage-driven sensitivity and the Hall plate resistance at each temperature.

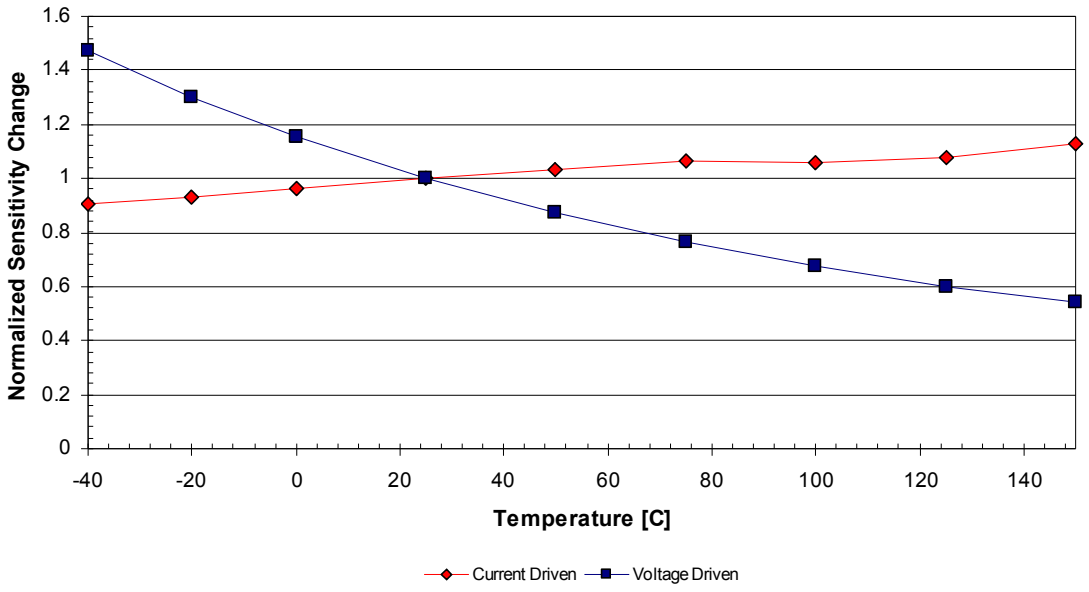

Figure 4.23 - *Voltage and current-driven Hall sensor sensitivity as a function of temperature.*

As it can be seen in Figure 4.23, the voltage-driven sensitivity decreases with temperature (as explained in Section 2.2.7). The current-driven sensitivity is not as flat as one might expect, because of the temperature dependence of the Hall coefficient (Section 2.2.2) and because of the change in stress seen by the Hall plate at different temperatures due to the different thermal expansion coefficients of the silicon die and the plastic compound [39].

4.4.4 Humidity Measurements

For this experiment the parts were first placed in an environmental chamber at 150°C for a couple of days to drive the moisture out of the package. Afterwards the conditions were set to 25°C 90% relative humidity. Permanent magnets were attached to the back of the parts to generate a constant magnetic field, as in previous tests.

The parts were measured in these conditions every 24 hours for four days. Tables 4.4 and 4.5 show the effect of moisture absorption by the plastic package on several devices' parameters for the test chips with 160μm and 50μm Hall plates. Included in the tables are the voltage-driven sensitivity, the current-driven sensitivity (obtained from the measured voltage-driven sensitivity and the Hall plate resistance), the averaged resistance of the two Hall plate diagonals, the averaged resistance of the two Epi resistor groups and the resistance of the P+ and Pwell resistor pairs. It is interesting to see that the rate of the parameters' change in the two test chips is different, which may mean that the moisture absorption rate was different in each part. The Pwell resistors rate of change is smaller than for the P+ resistors, an unexpected result taking into account that the Pwell resistors have lower doping concentration.

Table 4.4 - *Effect of humidity absorption on test chip parameters at 25°C, 90%RH for 160μm Hall plates.*

Days	Voltage Driven Sensitivity Change [%]	Current Driven Sensitivity Change [%]	Averaged Diagonal HP Resistance Change [%]	Averaged Epi Resistance Change [%]	P+ Resistance Change [%]	Pwell Resistance Change [%]
0	0.000	0.000	0.000	0.000	0.000	0.000
1	1.729	1.059	-0.661	-0.568	0.158	-0.024
2	2.337	1.471	-0.849	-0.755	0.234	0.002
3	2.859	1.801	-1.032	-0.909	0.312	0.073
4	3.332	2.094	-1.202	-0.965	0.407	0.215

Table 4.5 - *Effect of humidity absorption on several test chip at 25°C, 90%RH for 50μm Hall plates.*

Days	Voltage Driven Sensitivity Change [%]	Current Driven Sensitivity Change [%]	Averaged Diagonal HP Resistance Change [%]	Averaged Epi Resistance Change [%]	P+ Resistance Change [%]	Pwell Resistance Change [%]
0	0.000	0.000	0.000	0.000	0.000	0.000
1	1.786	1.281	-0.496	-0.573	0.216	0.112
2	2.364	1.713	-0.636	-0.735	0.296	0.163
3	2.761	1.951	-0.787	-0.888	0.346	0.205
4	3.027	2.070	-0.929	-1.040	0.347	0.159

The change in the sum of the in-plane stress components ($\sigma_x + \sigma_y$) can be obtained from the integrated resistors (see Eq.4.14).

$$\sigma_x + \sigma_y = \frac{\Delta R}{R}\frac{2}{\pi_{11} + \pi_{12}} \tag{4.22}$$

From the tested resistors, the n-type Epi resistors are most sensitive to stress, in agreement with the theory (Table 4.1). This fact makes them the best option to sense stress variations. The change in stress at 25°C will be given by:

$$\sigma_x + \sigma_y = \frac{\Delta R_{Epi}}{R_{Epi}}\frac{2}{\pi_{11} + \pi_{12}} = \frac{1}{-24.4\times10^{-11}\,1/Pa}\frac{\Delta R_{Epi}}{R_{Epi}} \tag{4.23}$$

If we neglect the effect of the normal stress σ_z, the current-driven sensitivity change can be estimated using Eq. (3.22) from the change in stress values obtained from Eq. (4.23).

$$\frac{\Delta S_I}{S_I} = P_{12}(\sigma_x + \sigma_y) = 45 \times 10^{-11}\, 1/Pa \;\; (\sigma_x + \sigma_y) \tag{4.24}$$

Tables 4.6 and 4.7 present the calculated change in the sum of in-plane stresses, the estimated current-driven sensitivity change, and the corrected sensitivity change that would result from using the estimated current-driven sensitivity change to compensate for the effect of stress.

Table 4.6 *- Calculated stress, measured and estimated current-driven sensitivity and corrected sensitivity at 25°C, 90%RH for 160μm Hall plates.*

Days	ΔStress [MPa]	Measured Current Driven Sensitivity Change [%]	Estimated Current Driven Sensitivity Change [%]	Stress Corrected Current Driven Sensitivity Change [%]
0	0.000	0.000	0.000	0.000
1	23.27	1.059	1.047	0.012
2	30.95	1.471	1.393	0.078
3	37.24	1.801	1.676	0.125
4	39.55	2.094	1.780	0.314

Table 4.7 *- Calculated stress, measured and estimated current-driven sensitivity and corrected sensitivity at 25°C, 90%RH for 50μm Hall plates.*

Days	ΔStress [MPa]	Measured Current Driven Sensitivity Change [%]	Estimated Current Driven Sensitivity Change [%]	Stress Corrected Current Driven Sensitivity Change [%]
0	0.000	0.000	0.000	0.000
1	23.49	1.281	1.057	0.224
2	30.14	1.713	1.356	0.357
3	36.40	1.951	1.638	0.313
4	42.62	2.070	1.918	0.153

Figures 4.24 and 4.25 compare the change in voltage-driven sensitivity, current-driven sensitivity and the stress-corrected current-driven sensitivity drifts due to moisture absorption by the plastic package. It can be clearly seen that with the proposed scheme the sensitivity drift is reduced almost by an order of magnitude.

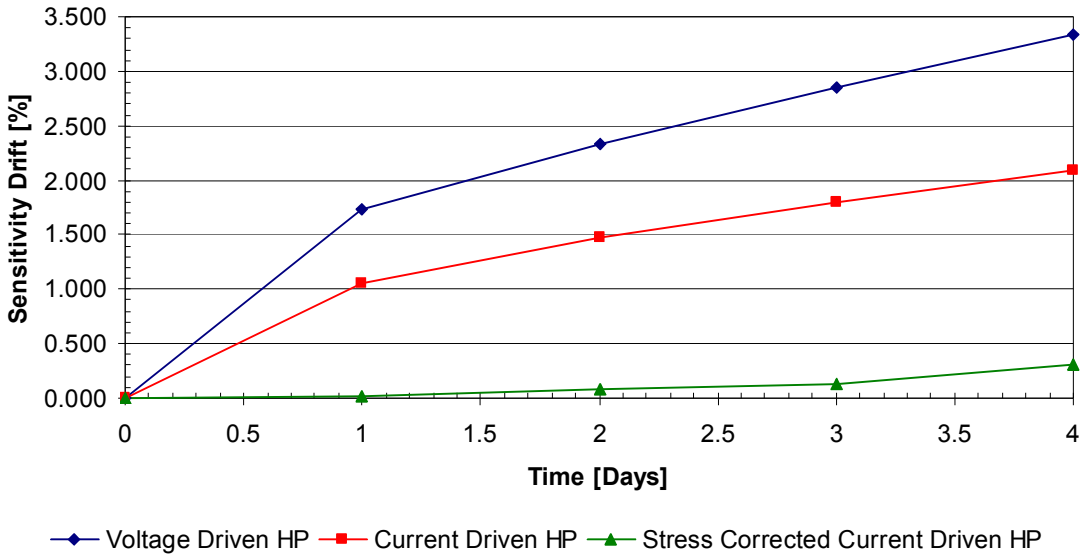

Figure 4.24 *- Sensitivity drift for 160µm Hall plate subject to 90%RH, 25°C.*

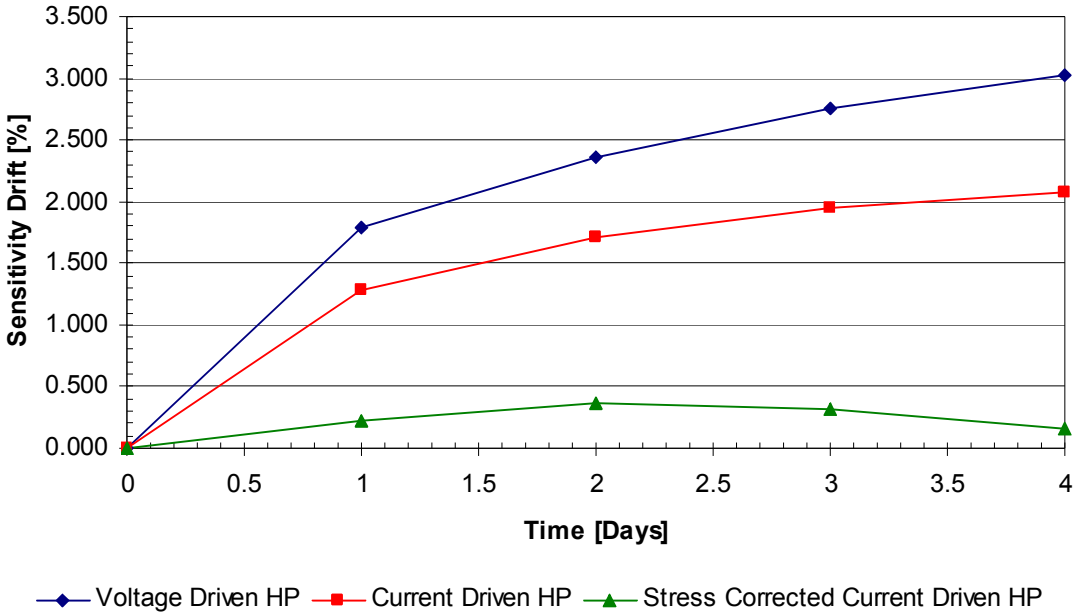

Figure 4.25 *- Sensitivity drift for 50µm Hall plate subject to 90%RH, 25°C.*

The same set of measurements was repeated at 75°C, 90%RH for the 50um Hall plates test chip. Due to the change in temperature, the piezoresistive and piezo-Hall coefficients must be modified. The correction factor for the piezoresistive coefficients can be obtained from Figure 3.6, and has a value of 0.87. For the n-Epi resistors, which are laid out in an L shape configuration, the new piezoresistive coefficient is:

$$0.87\frac{\pi_{11}+\pi_{12}}{2} = -21.23\times10^{-11}\frac{1}{Pa} \tag{4.25}$$

Hälg [38] reports that the piezo-Hall coefficient P_{12} has a temperature coefficient of roughly -8x10^{-13} Pa^{-1}/°C, so the Piezo-Hall coefficient at 75°C will be:

$$P_{12}\big|_{25°C} + \Delta T\left(-8\times10^{-13}\frac{Pa^{-1}}{\circ C}\right) = 41\times10^{-11}\frac{1}{Pa} \tag{4.26}$$

The part was measured every 24 hours for four days. Table 4.8 shows the effect of moisture absorption by the plastic package on several device parameters. Also included in the table is the current-driven sensitivity, obtained from the measured voltage-driven sensitivity and the Hall plate resistance.

Table 4.8 *- Effect of humidity absorption on test chip parameters at 75°C, 90%RH for 50μm Hall plates.*

Days	Voltage Driven Sensitivity Change [%]	Current Driven Sensitivity Change [%]	Averaged Diagonal HP Resistance Change [%]	Averaged Epi Resistance Change [%]	P+ Resistance Change [%]	Pwell Resistance Change [%]
0	0.000	0.000	0.000	0.000	0.000	0.000
1	2.305	1.583	-0.706	-0.869	0.312	0.164
2	2.181	1.437	-0.728	-0.874	0.285	0.178
3	2.223	1.451	-0.756	-0.908	0.292	0.170
4	2.232	1.470	-0.746	-0.899	0.309	0.180

Table 4.9 presents the calculated change in the sum of the in-plane stresses, the estimated current-driven sensitivity change, and the corrected sensitivity change that

would result from using the estimated current-driven sensitivity change to compensate for the effect of stress.

Table 4.9 - *Calculated stress, measured and estimated current-driven sensitivity and corrected sensitivity at 75°C, 90%RH for 50μm Hall plates.*

Days	ΔStress [MPa]	Measured Current Driven Sensitivity Change [%]	Estimated Current Driven Sensitivity Change [%]	Stress Corrected Current Driven Sensitivity Change [%]
0	0.000	0.000	0.000	0.000
1	40.94	1.583	1.678	-0.096
2	41.15	1.437	1.687	-0.250
3	42.76	1.451	1.753	-0.302
4	42.36	1.470	1.737	-0.267

A plot comparing the change in voltage-driven sensitivity, current-driven sensitivity and the stress-corrected current-driven sensitivity drifts due to moisture absorption by the plastic package is shown in Figure 4.26. As in the previous cases, the proposed scheme significantly reduces the sensitivity drift.

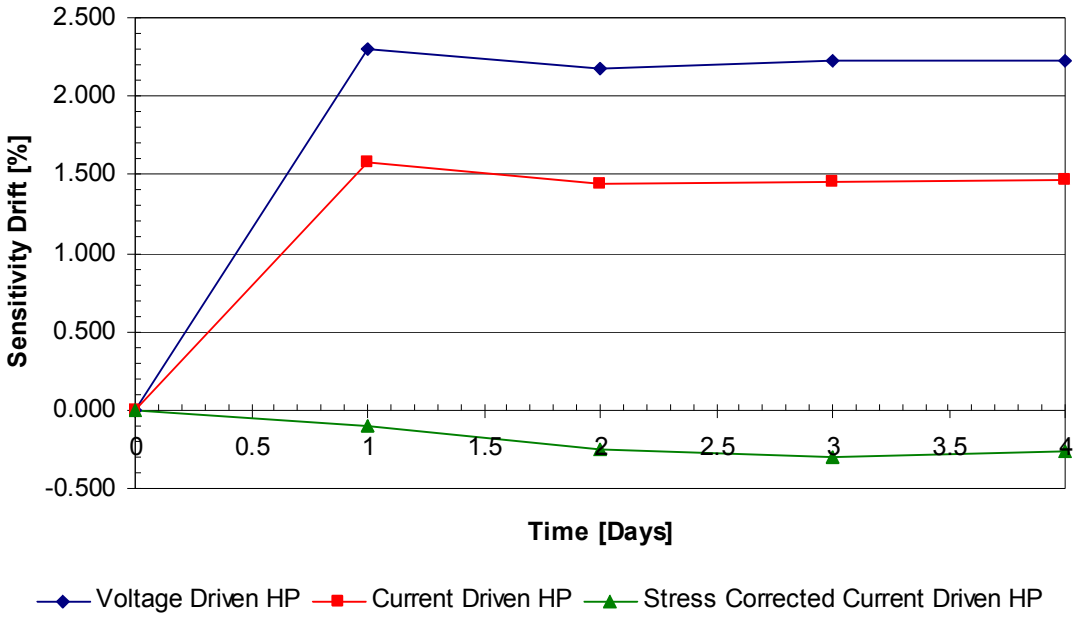

Figure 4.26 - *Sensitivity drift for 50μm Hall plate subject to 90%RH, 75°C.*

4.5 System Implementation

4.5.1 Effect of Temperature on the Piezoresistive and Piezo-Hall Coefficients

Both the silicon piezoresistive and Piezo-Hall coefficients have a temperature dependency. The variation of these parameters with temperature has to be taken into account when the Hall sensitivity is being compensated, as was done in Section 4.4.3 for the measurements at 75°C. Because Epi resistors are used to estimate the in-plane stress, the attention will be focused on the n-doped piezoresistive coefficients. The temperature dependence of the piezoresistive coefficients can be obtained from Figure 3.6. For the piezo-Hall coefficient P_{12}, the estimation in [38] is used, which proposes a temperature coefficient of -8×10^{-13} 1/Pa°C. Figure 4.27 shows the piezoresistive and piezo-Hall coefficients drift with temperature, normalized to 25°C.

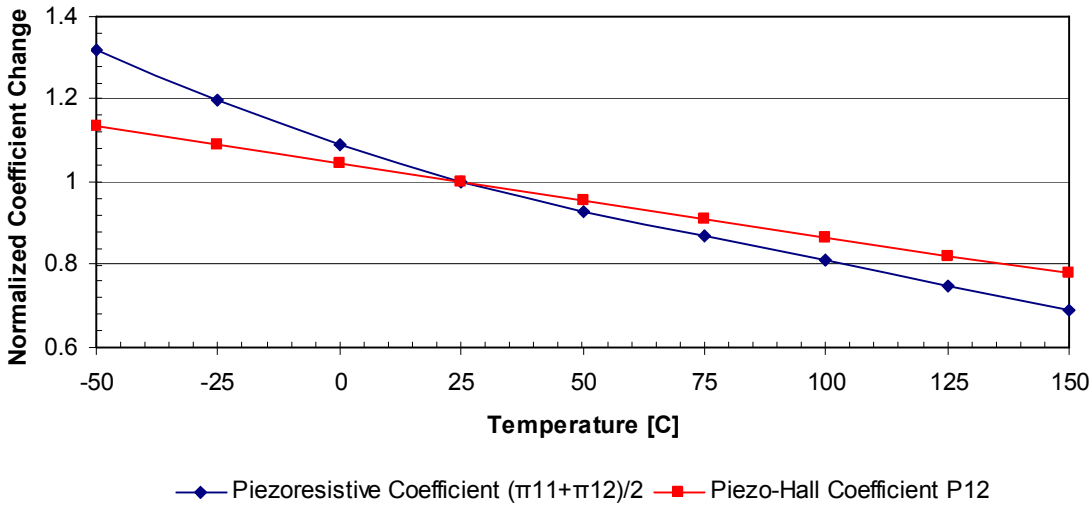

Figure 4.27 - *Normalized piezoresistive [36] and Piezo-Hall [38] coefficients as a function of temperature.*

4.5.2 Effect of Stress and Temperature on the Stress-sensing Resistors

As mentioned earlier, n-Epi resistors are used to sense changes in the in-plane stress because they show the largest stress sensitivity. The piezoresistive coefficients vary with temperature (as was seen in Section 4.5.1), which means that for a given stress change, the integrated resistor's value variation will depend on the operating temperature. It can be clearly seen from Figure 4.27 (and Fig. 3.6) that for lower temperatures the effect of the stress will be more noticeable, because the piezoresistive coefficient is bigger. At this point it is important to define the temperature and stress operating range of the sensor. This range will help in the understanding of the coefficients' variation, but by no means limit the operating range of the sensor. For temperature, the automotive standard range of -40°C to 150°C is selected. The stress variation range is defined to be from 0 to 50MPa, based on the results in Section 4.4.4 (note that the actual stress seen by the die can be any number, here we only define the range of stress change due to humidity absorption by the plastic package).

The effect of the piezoresistive coefficient variation with temperature on the resistance change can be calculated using the operating range just defined. The N-Epi resistor "L" (Fig. 4.1) value is normalized at zero stress variation for the whole temperature range, which in essence removes the temperature coefficient of the resistance. A graphical representation of the resistance change is shown in Figure 4.28. It can be clearly seen that the effect of the piezoresistive coefficient variation with temperature on the output of the stress sensor is very noticeable, and by no means can be disregarded.

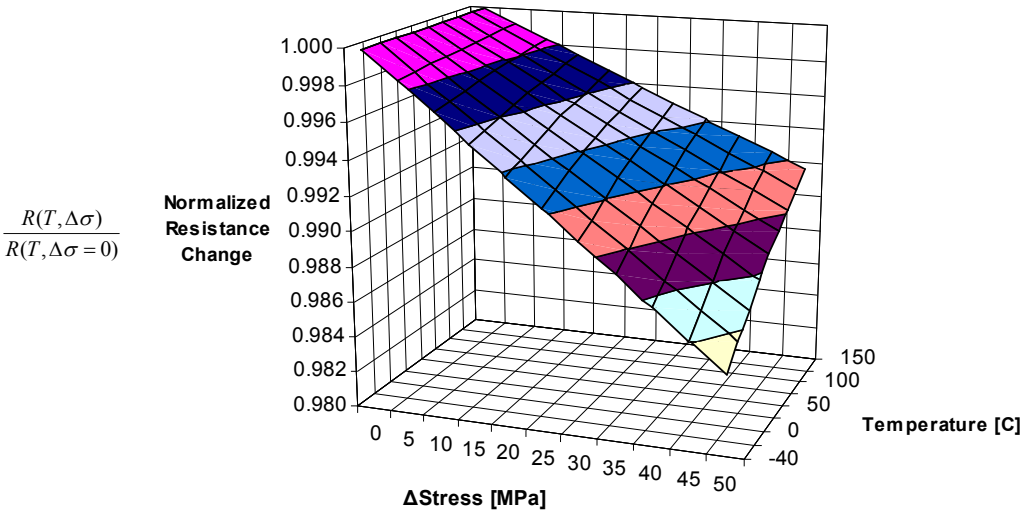

Figure 4.28 - *Effect of the piezoresistive coefficient variation with temperature on the n-Epi resistance change.*

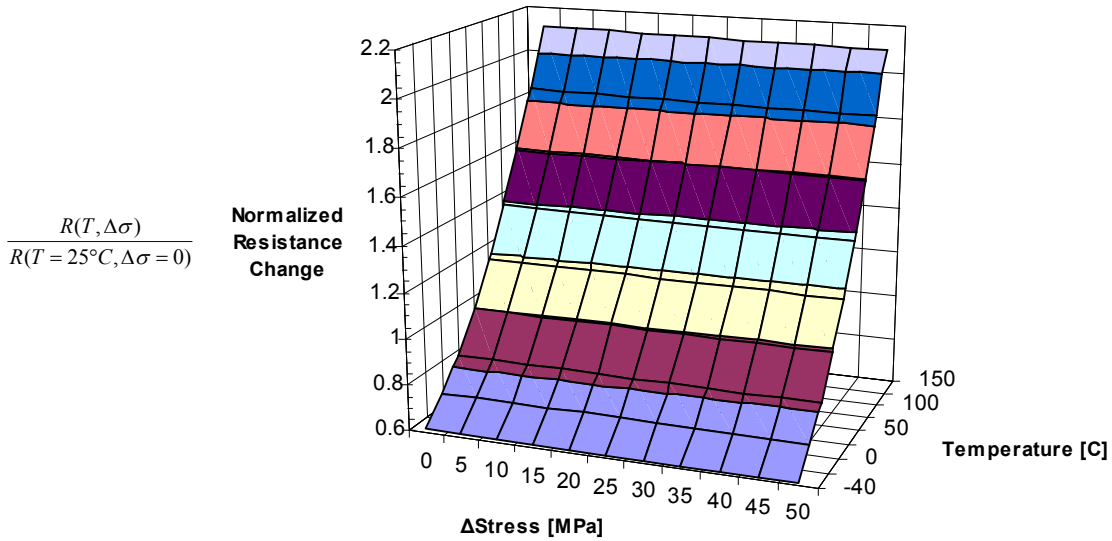

Figure 4.29 - *N-Epi resistance change with stress and temperature. Normalized at 25°C*

If the temperature coefficient of the stress sensor resistance is taken into consideration, normalizing the resistance only at 25°C, the stress and temperature sensitivities of the stress sensor can be compared. In Figure 4.29, if no stress change is present, the resistance variation with temperature is identical to the one shown in Figure

4.22. It can be clearly seen in Figure 4.29 that for the defined range, the n-Epi resistors are two orders of magnitude more sensitive to temperature than stress. Close attention will have to be put in the design of the temperature sensor to obtain the required level of precision needed to cancel out the effects of temperature in the stress sensing resistors.

4.5.3 Proposed System

The proposed system implementation is shown in Figure 4.30. It consists of a Hall device, a signal amplifier, a group of integrated n-Epi resistors placed close to the Hall plate, a temperature sensor and a processing unit. This last block is responsible for managing the data obtained from the integrated piezoresistors and the temperature sensor and output the required Hall plate bias current to compensate the system gain.

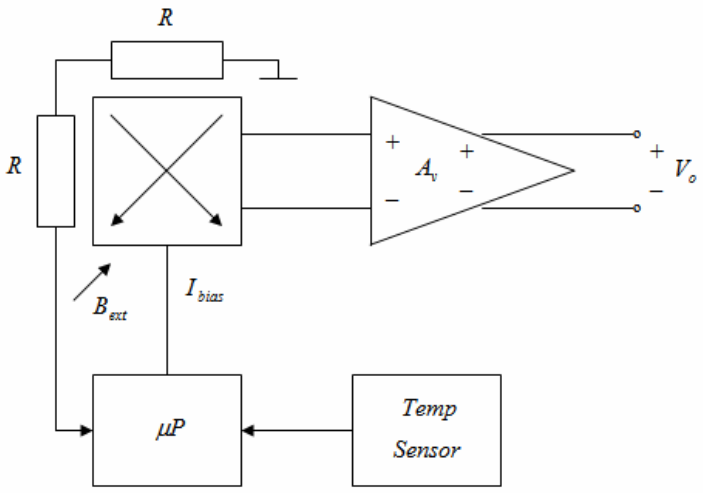

Figure 4.30 *- System implementation.*

From the previous sections we know that if only the in-plane normal stresses are considered, then:

$$\frac{\Delta S_I}{S_I} = P_{12}(\sigma_x + \sigma_y) \tag{4.27}$$

$$\frac{\Delta R}{R} = \frac{\pi_{11} + \pi_{12}}{2}(\sigma_x + \sigma_y) \tag{4.28}$$

If the resistance change ΔR/R of the n-Epi resistors due to stress variations has been obtained, the change in sensitivity will be given by:

$$\frac{\Delta S_I}{S_I} = \frac{\Delta R}{R}\frac{2P_{12}}{\pi_{11} + \pi_{12}} \tag{4.29}$$

$$\frac{\Delta S_I}{S_I} = \frac{\Delta R}{R}\frac{2P_{12}\big|_{25C}}{\pi_{11}\big|_{25C} + \pi_{12}\big|_{25C}}\frac{k_P(T)}{k_\pi(T)}, \tag{4.30}$$

where $k_P(T)$ and $k_\pi(T)$ are the normalized temperature factors of the piezo-Hall and piezoresistive coefficients, plotted in Figure 4.27. A new factor $k(T)$ can be defined, such that:

$$k(T) = \frac{2P_{12}\big|_{25C}}{\pi_{11}\big|_{25C} + \pi_{12}\big|_{25C}}\frac{k_P(T)}{k_\pi(T)} \tag{4.31}$$

$$\frac{\Delta S_I}{S_I} = \frac{\Delta R}{R}k(T) \tag{4.32}$$

Provided that the change in resistance due to stress is known, the sensitivity change can simply be found by multiplying ΔR/R by $k(T)$. A graphical representation of $k(T)$ over temperature is shown in Figure 4.31.

If the signal processing is done in the digital domain, analog to digital converters will have to be implemented to translate the inputs from the stress-sensing resistors and the temperature sensor. In addition, a signal processor will have to be designed and a memory block will have to be included to store the different variables while they are

being processed. It remains to be proven if the compensation scheme can be implemented entirely in the analog domain.

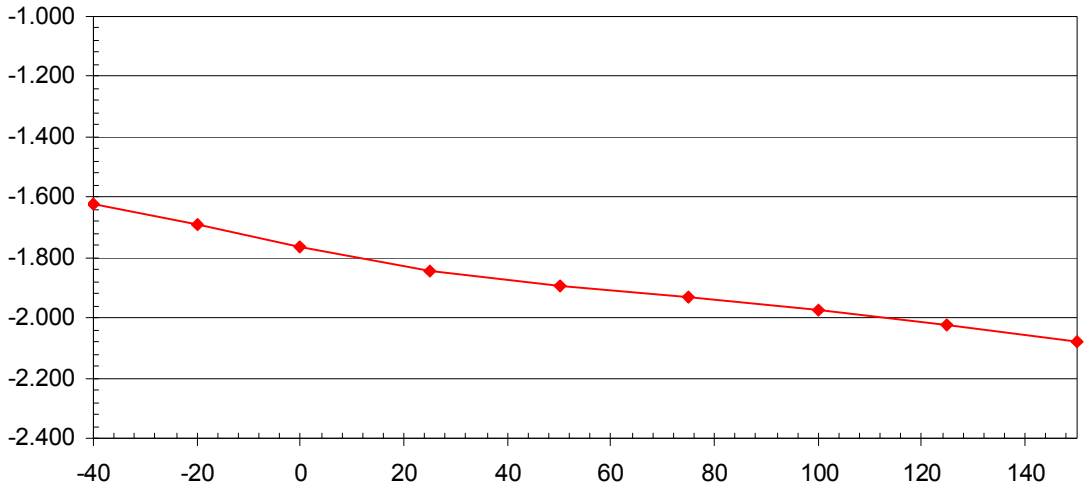

Figure 4.31 - *Conversion factor k(T) over temperature.*

The proposed compensation system is of the open-loop type, which means that if some effect other than stress causes the system gain to vary, the compensation scheme will not be able to correct it. It is also important to state that only the effect of the in-plane normal stresses is being taken into account to compensate the sensitivity.

CHAPTER V

COMPENSATION BY MAGNETIC FEEDBACK

5.1 Introduction

The gain of a system is defined by the ratio of its output to input signals. If a linear system's gain is needed to be found, a signal of known amplitude can be fed to the system's input while the output is monitored. Any subsequent changes in the output signal strength will mean that the system gain has changed. If a Hall sensor is placed under a magnetic signal of known strength, the same principle can be applied to obtain the Hall sensitivity, and to detect changes in its value.

The reference magnetic signal can be generated either by a permanent magnet or a coil. If a permanent magnet were to be used, both the distance to the Hall plate and the magnetic field strength should be kept constant under varying external conditions. If, on the other hand, a discrete coil is used, its structure, its distance to the Hall plate and the current flowing through the coil should remain invariable. These requisites are usually difficult to achieve to the required degree of accuracy (must detect a 0.1% sensitivity change, see Section 5.5.1).

If instead of being discrete, the coil is integrated in the silicon chip, its geometry and distance to the Hall plate will remain essentially constant with changes in temperature and humidity (to the extents of our needs). If the coil's bias current is trimmed to be flat over temperature, a constant magnetic field will be obtained.

The reference magnetic field must be distinguishable from the external magnetic field, which can be achieved either by time multiplexing or spatial separation of the fields. For single sensing-element magnetic sensors spatial separation is not possible. Time multiplexing with permanent magnets is impractical, because it would be cumbersome to change the magnet's polarity by physically flipping it, and would be impossible to shut its magnetic field off. Because of these issues, the permanent magnet solution must be discarded. The direction of the current in an integrated coil, on the other hand, can be easily switched, so, provided that the Nyquist frequency is met, it is possible to achieve time multiplexing.

Implementations of integrated coils and the systems that support them have been reported in the literature. The first publication, by J. Trontelj et al., dates from 1994 [46]; their coil can generate 1G/mA. The following paper, by P.L.C. Simon et al. in 1996 [47], achieves 0.3G/mA with a Hall plate size of 100μm by 200μm. The big Hall sensor may help explain the poor coil performance. In 1999, J. Trontelj published another paper [48], in which the integrated coil generates 1.5G/mA. A paper in 2002 by M. Demierre et al. [49] claims 3.92G/mA, using a small, 2.4μm by 2.4μm, Hall plate. Because of the reduced size of the magnetic sensor, the Hall sensitivity is only 180V/AT, which greatly reduces the advantage of the coil performance. M. Pastre et al. published two papers in 2005 with a full system implementation [50, 51] and later patented it [52] (no information about the performance of the integrated coil was provided).

The objective of this chapter is to present a coil implementation that can match or exceed the performance of previous papers, and propose a closed loop system implementation that can stabilize the Hall plate sensitivity and the overall system gain.

In the following section a closed-form formula for the magnetic field generated by an ideal coil (whose metal lines have no width or height) will be theoretically obtained. Afterwards, single turn coils will be simulated using finite element models. These simulations will provide a higher degree of accuracy, because the metal lines will be geometrically and electrically accurate, matching the parameters of the process where the coils will be implemented. With the insight obtained from the single turn simulations two coils will be proposed, and finite element simulations and silicon based measurements will be presented. The final subsection of this chapter will propose a system using an integrated coil as the gain stabilizing mechanism.

5.2 Integrated Coil Design

5.2.1 Theoretical Analysis

The contribution to the magnetic field at an arbitrary point P generated by a current flowing through a conductor segment *dl* can be described by the Biot–Savart law:

$$d\vec{B}_P = \frac{\mu_o \mu_r I\left(d\vec{l} \times \vec{r}\right)}{4\pi\left|\vec{r}\right|^3}, \tag{5.1}$$

where μ_o is the permeability of vacuum, μ_r is the relative permeability of the medium, *dl* is a vector representing an infinitesimal segment of a conductor with direction equal to the current flow, *I* is the magnitude of the electric current, and *r* is a vector whose magnitude is the distance from the infinitesimal conductor to the point *P* and its direction is from the conductor to the point *P*. A graphical representation of the Biot-Savart law can be seen on Figure 5.1.

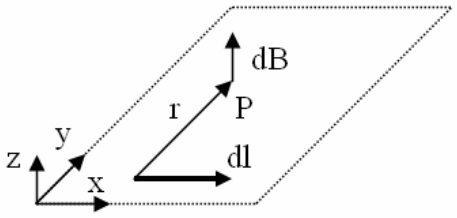

Figure 5.1 - *Representation of the Biot-Savart law.*

Equation (5.1) can be used to calculate the magnetic field distribution on the surface of a Hall plate due to a current flowing through a square-shaped coil. Because of the superposition principle, the contribution of each of the four coil sides can be calculated independently. Figure 5.2 (A) shows a graphical representation of one of these sides, with the nomenclature that will be used to solve for the magnetic field. The point *P* is in the same plane as the square shaped coil.

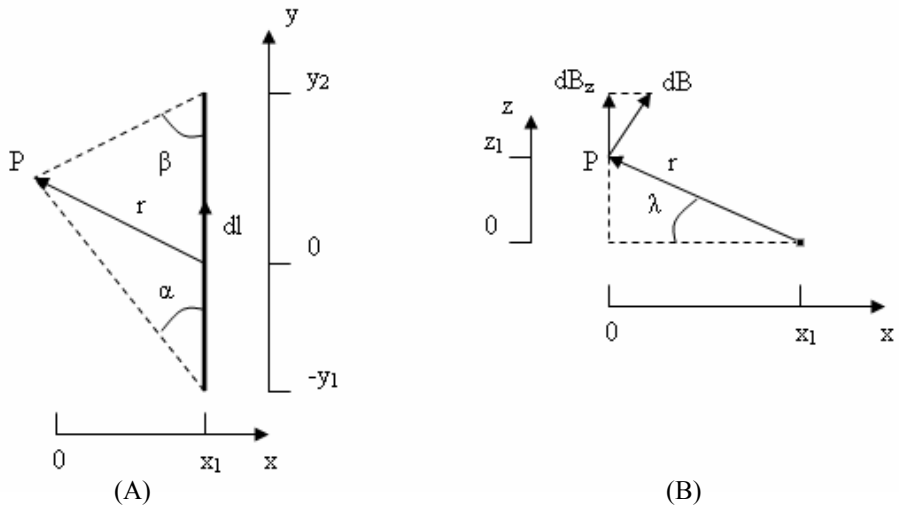

Figure 5.2 - *Representation of one of the four coil sides with case (A): point P is in the same plane of the coil and case (B): point P is out of plane.*

From Figure 5.2 (A) it becomes apparent that:

$$\left|d\vec{l} \times \vec{r}\right| = x_1 dl \tag{5.2}$$

$$d\vec{l} = d\vec{y} \tag{5.3}$$

$$|r| = \sqrt{x_1^{\,2} + y^2} \tag{5.4}$$

This way Equation (5.1) can be rewritten as:

$$dB_P = \frac{\mu_o \mu_r I x_1 dy}{4\pi \sqrt{x_1^{\,2} + y^2}^{\,3}} \tag{5.5}$$

The magnetic field due to the coil segment can be calculated by integrating over the length of the coil segment.

$$B_P = \frac{\mu_o \mu_r I x_1}{4\pi} \int_{-y1}^{y2} \frac{dy}{\sqrt{x_1^{\,2} + y^2}^{\,3}} \tag{5.6}$$

$$B_P = \frac{\mu_o \mu_r I x_1}{4\pi} \left[\frac{y}{x_1^{\,2} \sqrt{x_1^{\,2} + y^2}} \right]_{-y1}^{y2} \tag{5.7}$$

$$B_P = \frac{\mu_o \mu_r I}{4\pi x_1} \left[\frac{y_2}{\sqrt{x_1^{\,2} + y_2^{\,2}}} + \frac{y_1}{\sqrt{x_1^{\,2} + y_1^{\,2}}} \right] \tag{5.8}$$

From Figure 5.2 (A) it can be clearly seen that:

$$\cos(\alpha) = \frac{y_1}{\sqrt{x_1^{\,2} + y_1^{\,2}}} \tag{5.9}$$

$$\cos(\beta) = \frac{y_2}{\sqrt{x_1^{\,2} + y_2^{\,2}}} \tag{5.10}$$

Thus, the magnetic field at point *P* due to a segment of the square shaped coil can be rewritten as:

$$B_P = \frac{\mu_o \mu_r I}{4\pi x_1} \left[\cos(\alpha) + \cos(\beta) \right] \tag{5.11}$$

If the point P is not in the same plane as the coil, as in Figure 5.2 (B), it is easy to see that the magnetic field at P will be given by:

$$B_P = \frac{\mu_o \mu_r I}{4\pi\sqrt{x_1^{\,2} + z_1^{\,2}}}\left[\frac{y_1}{\sqrt{x_1^{\,2} + y_1^{\,2} + z_1^{\,2}}} + \frac{y_2}{\sqrt{x_1^{\,2} + y_2^{\,2} + z_1^{\,2}}}\right] \tag{5.12}$$

The angles α and β are redefined as:

$$\cos(\alpha) = \frac{y_1}{\sqrt{x_1^{\,2} + y_1^{\,2} + z_1^{\,2}}} \tag{5.13}$$

$$\cos(\beta) = \frac{y_2}{\sqrt{x_1^{\,2} + y_2^{\,2} + z_1^{\,2}}} \tag{5.14}$$

The magnetic field component in the z direction can be calculated as:

$$Bz_P = B_P \cos(\lambda)\,, \tag{5.15}$$

$$\cos(\lambda) = \frac{x_1}{\sqrt{x_1^{\,2} + z_1^{\,2}}} \tag{5.16}$$

So Bz_p is equal to:

$$Bz_P = \frac{\mu_o \mu_r I x_1}{4\pi(x_1^{\,2} + z_1^{\,2})}\left[\frac{y_1}{\sqrt{x_1^{\,2} + y_1^{\,2} + z_1^{\,2}}} + \frac{y_2}{\sqrt{x_1^{\,2} + y_2^{\,2} + z_1^{\,2}}}\right] \tag{5.17}$$

$$Bz_P = \frac{\mu_o \mu_r I x_1}{4\pi(x_1^{\,2} + z_1^{\,2})}\left[\cos(\alpha) + \cos(\beta)\right] \tag{5.18}$$

Applying the superposition principle, the magnetic field at point P due to the complete one-turn square shaped coil can now be obtained. Figure 5.3 depicts the coil and the point P, along with the nomenclature to be used. The origin of the coordinate system has been set to the coil's center, a and b are the distances from the origin to the point P, x_1, x_2, y_1 and y_2 are the distances from the point P to the edges of the coil, and l is

the length of the coil. The point *P* is not in the same plane as the coil, but at a vertical distance z_1.

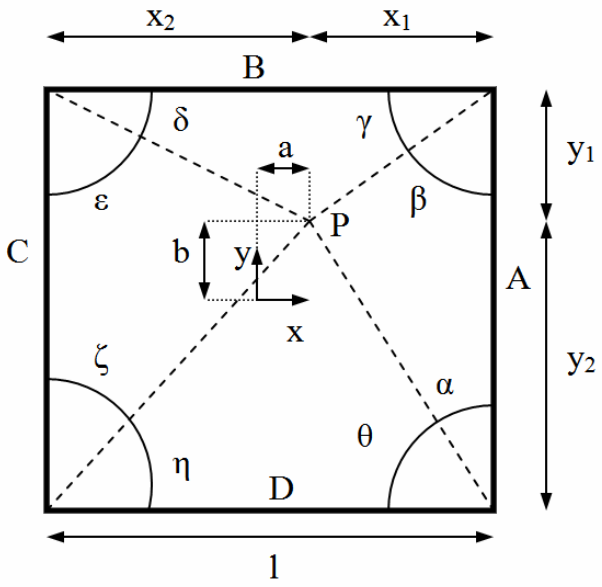

Figure 5.3 - *Representation of the square shaped coil and the point P where the magnetic field will be found. The point P is not in the plane of the coil.*

The distances x_1, x_2, y_1 and y_2 can be defined as a function of the coil length and the point *P* coordinates.

$$x_1 = \frac{l}{2} - a \quad , \quad x_2 = \frac{l}{2} + a \tag{5.19}$$

$$y_1 = \frac{l}{2} - b \quad , \quad y_2 = \frac{l}{2} + b \tag{5.20}$$

The angles from the coil edges to the point P are given by:

$$\cos(\alpha) = \frac{y_2}{\sqrt{x_1^{\,2} + y_2^{\,2} + z_1^{\,2}}} \tag{5.21}$$

$$\cos(\beta) = \frac{y_1}{\sqrt{x_1^{\,2} + y_1^{\,2} + z_1^{\,2}}} \tag{5.22}$$

$$\cos(\gamma) = \frac{x_1}{\sqrt{x_1^{\,2} + y_1^{\,2} + z_1^{\,2}}} \tag{5.23}$$

$$\cos(\delta) = \frac{x_2}{\sqrt{x_2^{\,2} + y_1^{\,2} + z_1^{\,2}}} \tag{5.24}$$

$$\cos(\varepsilon) = \frac{y_1}{\sqrt{x_2^{\,2} + y_1^{\,2} + z_1^{\,2}}} \tag{5.25}$$

$$\cos(\zeta) = \frac{y_2}{\sqrt{x_2^{\,2} + y_2^{\,2} + z_1^{\,2}}} \tag{5.26}$$

$$\cos(\eta) = \frac{x_2}{\sqrt{x_2^{\,2} + y_2^{\,2} + z_1^{\,2}}} \tag{5.27}$$

$$\cos(\theta) = \frac{x_1}{\sqrt{x_1^{\,2} + y_2^{\,2} + z_1^{\,2}}} \tag{5.28}$$

Thus, the magnetic field due to each of the coil segments is:

$$Bz_P\big|_A = \frac{\mu_o \mu_r I x_1}{4\pi(x_1^{\,2} + z_1^{\,2})}\left[\cos(\alpha) + \cos(\beta)\right] \tag{5.29}$$

$$Bz_P\big|_B = \frac{\mu_o \mu_r I y_1}{4\pi(y_1^{\,2} + z_1^{\,2})}\left[\cos(\gamma) + \cos(\delta)\right] \tag{5.30}$$

$$Bz_P\big|_C = \frac{\mu_o \mu_r I x_2}{4\pi(x_2^{\,2} + z_1^{\,2})}\left[\cos(\varepsilon) + \cos(\zeta)\right] \tag{5.31}$$

$$Bz_P\big|_D = \frac{\mu_o \mu_r I y_2}{4\pi(y_2^{\,2} + z_1^{\,2})}\left[\cos(\eta) + \cos(\theta)\right] \tag{5.32}$$

The total magnetic field at point *P* is equal to:

$$Bz_P = Bz_P\big|_A + Bz_P\big|_B + Bz_P\big|_C + Bz_P\big|_D \tag{5.33}$$

In order to gain insight into the magnetic field distribution, Eq. (5.33) was solved on the surface of a Hall plate with an area of 50μm x 50μm. Figure 5.4 shows the plots obtained for two different coils. Figure 5.4(A) corresponds to the magnetic field distribution due to a 5mA current flowing through a 40μm wide coil. The magnetic field

is positive in the area inside of the coil, and negative outside of it. Figure 5.4(B) shows the magnetic field distribution due to a 60µm wide coil. In this case the magnetic field is positive throughout the whole Hall plate surface area.

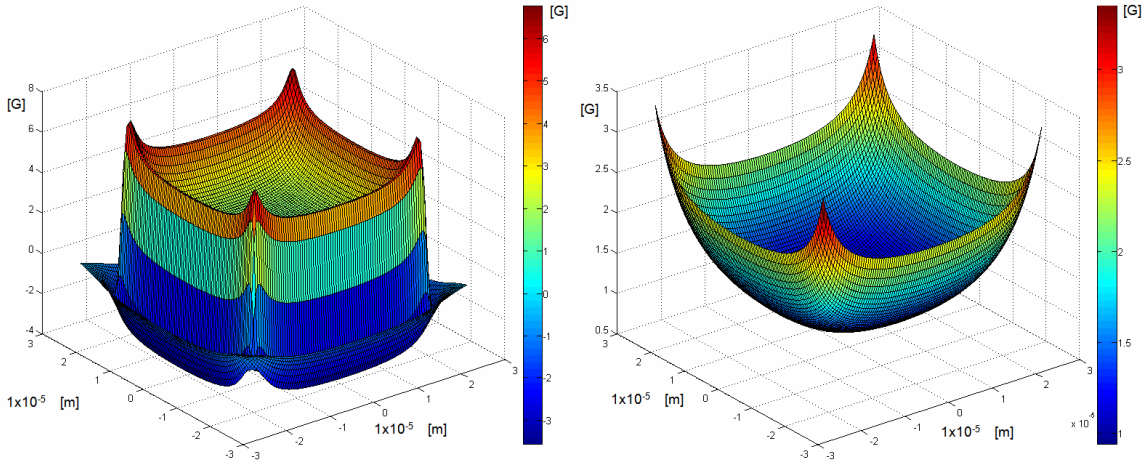

(A) (B)

Figure 5.4 - *Distribution of the magnetic field Bz on the Hall plate surface in Gauss. Assumed is a 50µm Hall Plate, a coil current of 5mA and a z-axis spacing between coil and Hall plate of 1.2 µm. Case (A) is for 40 µm coil, case (B) for a 60 µm coil.*

Coils with more than one turn can also be calculated using Equation (5.33). Based on the superposition principle, the contribution of the extra coil segments can be added to the total magnetic field.

5.2.2 Finite Element Analysis

5.2.2.1 Single loop coils

The formulas obtained in the previous section remain accurate only while the width and height of the metal lines that form the coil are much smaller than the width of the coil turn. The theoretical formulas could be modified to include the metal lines cross-section area, but instead the coil geometry is implemented using finite element models.

The distance between metal layers, the geometry of the metal lines and their conductivity match those of the semiconductor process where the coils are implemented. The magnetic field generated by the integrated single-turn coils is obtained using an electrostatic-magnetostatic coupled system. Figure 5.5 shows the magnetic field distribution on the Hall plate surface for three different coil sizes. In all cases, a current of 5mA is flowing through the coil.

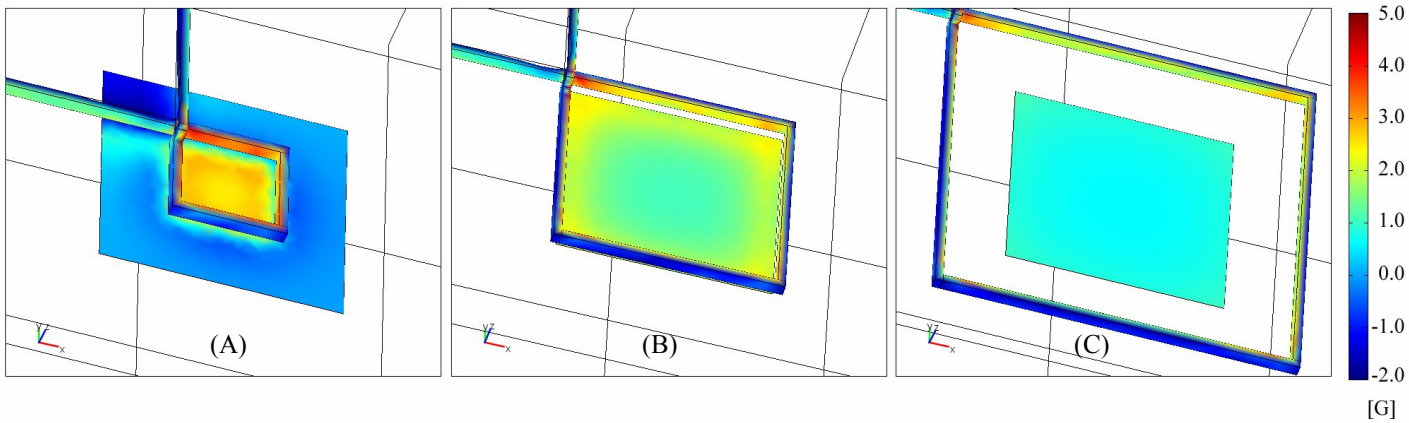

Figure 5.5 - *Magnetic field normal to the Hall plate surface for different coil sizes. Hall plate size : 50µm side length. Bias current: 5mA. Distance from Hall plate edge to coil: (A) -15µm, (B) 0µm, (C) 15µm.*

Figure 5.6 shows a plot of the magnetic field averaged over the surface area of a 50µm Hall plate and generated by a single turn coil implemented using each of the two metal layers available in the process (Metal 1 and Metal Top) as a function of the spacing between coil and Hall plate edge. It can be clearly seen that the magnetic field contribution is biggest for coils with its geometry near the outer edge of the Hall plate. In general, the first metal layer (closer to the plane of the Hall plate) generates a slightly larger field. It is also interesting to see that for coils with diameter smaller than the Hall plate size (as in Figure 5.5 (A)) the average magnetic field contribution on the Hall plate area is still positive.

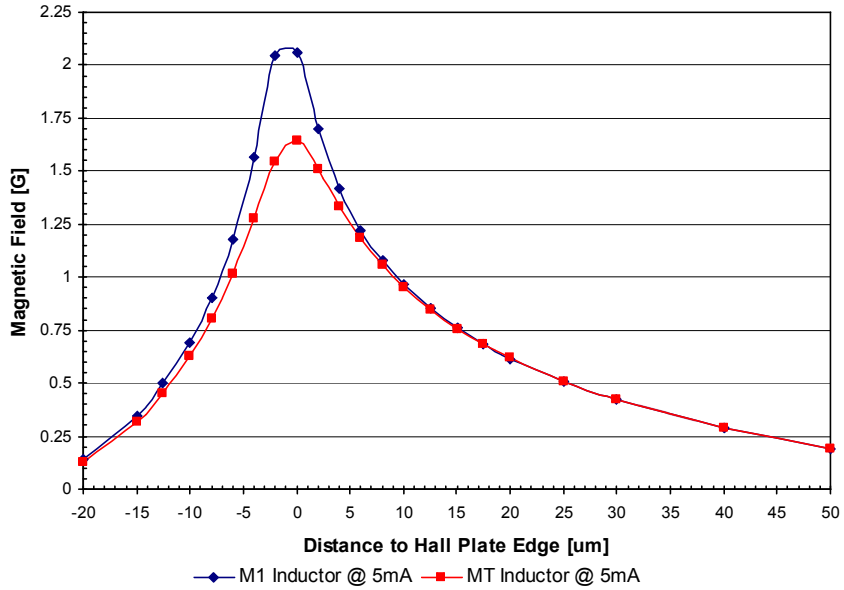

Figure 5.6 - *Magnetic field normal to the Hall plate surface and averaged over the Hall plate area as a function of distance to the Hall plate edge. Hall Plate: 50μm per side. Bias current: 5mA.*

The information of Figure 5.6 can be normalized with respect to the maximum magnetic field to more clearly show the contribution of each turn as a function of distance between coil and Hall plate edge (see Fig. 5.7).

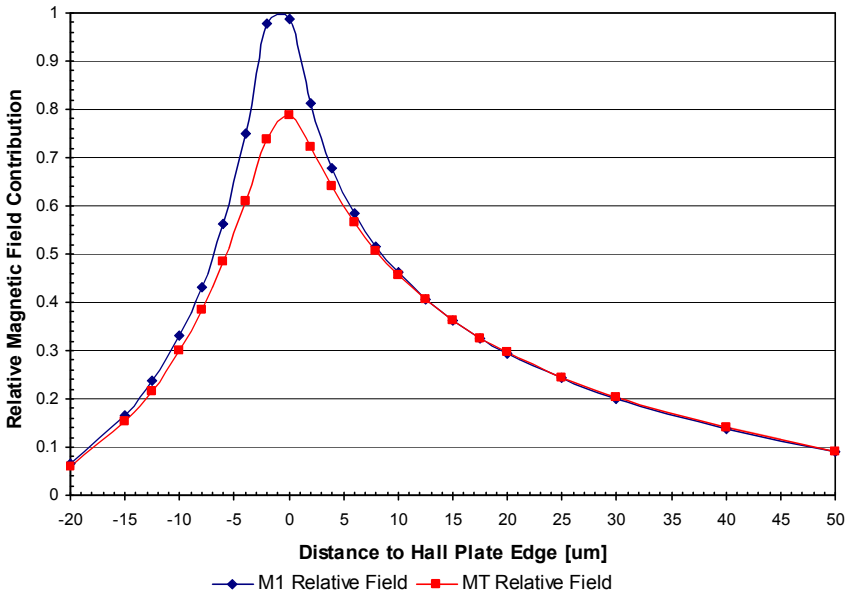

Figure 5.7 - *Relative contribution to the total magnetic field per coil turn as a function of distance to the Hall plate edge, normalized with respect to the maximum magnetic field.*

It is important to keep in mind while designing the coils that the Hall plate has four terminals (plus a substrate contact), and that these terminals have to be contacted preferably with metal lines.

5.2.2.2 Coil Design Using Simple Metal Layer (Coil A)

The first coil is implemented using only the Metal Top layer. The simplicity of its design will be helpful to asses the accuracy of the simulations when confronted with measured data. The first coil turn is overlapping the Hall plate area, with a 7.5µm distance from the Hall plate edge to the inner coil. The outmost turn is at a distance of 35µm from the Hall plate edge. Considering that the Hall device is 50µm per side, the coil structure has a width of 120µm. Figure 5.8 shows the result of an electrical finite element simulation of this design. As a result of a 5mA current flowing through the coil, a 0.124V voltage drop is generated. This gives us a resistance of 24.8Ω for the coil.

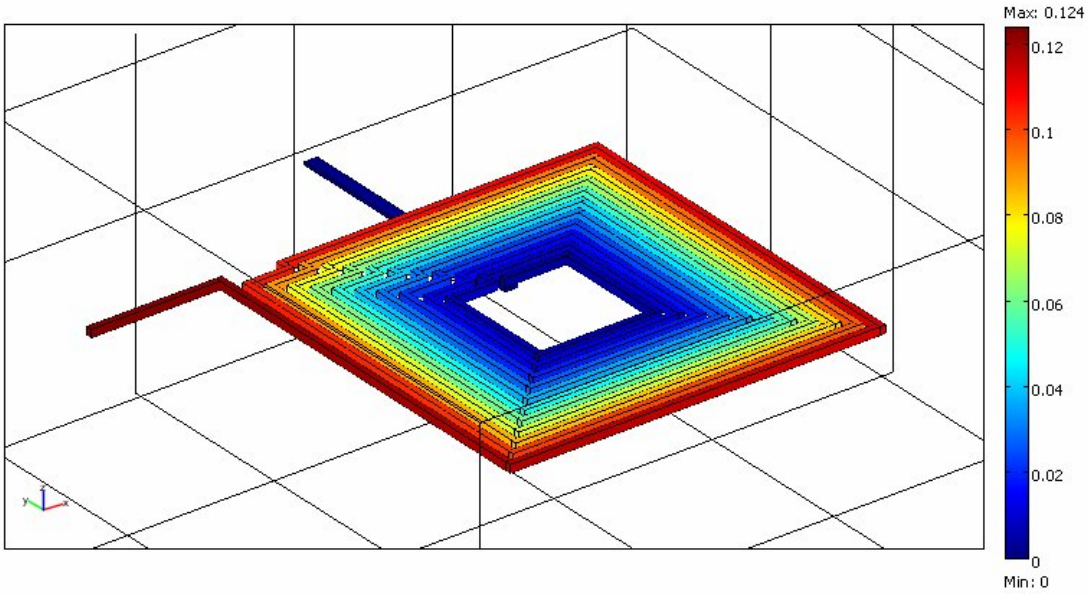

Figure 5.8 - *Structure of Integrated Coil A.*
For a 5mA bias current, the voltage drop in the coil is 0.124V

The 5mA current flowing through the coil will generate an average magnetic field of 8.84G (0.884mT) across the surface of the Hall plate. The results of a coupled electrostatic-magnetostatic simulation, shown in Figure 5.9, illustrate the magnetic field distribution on the Hall plate surface.

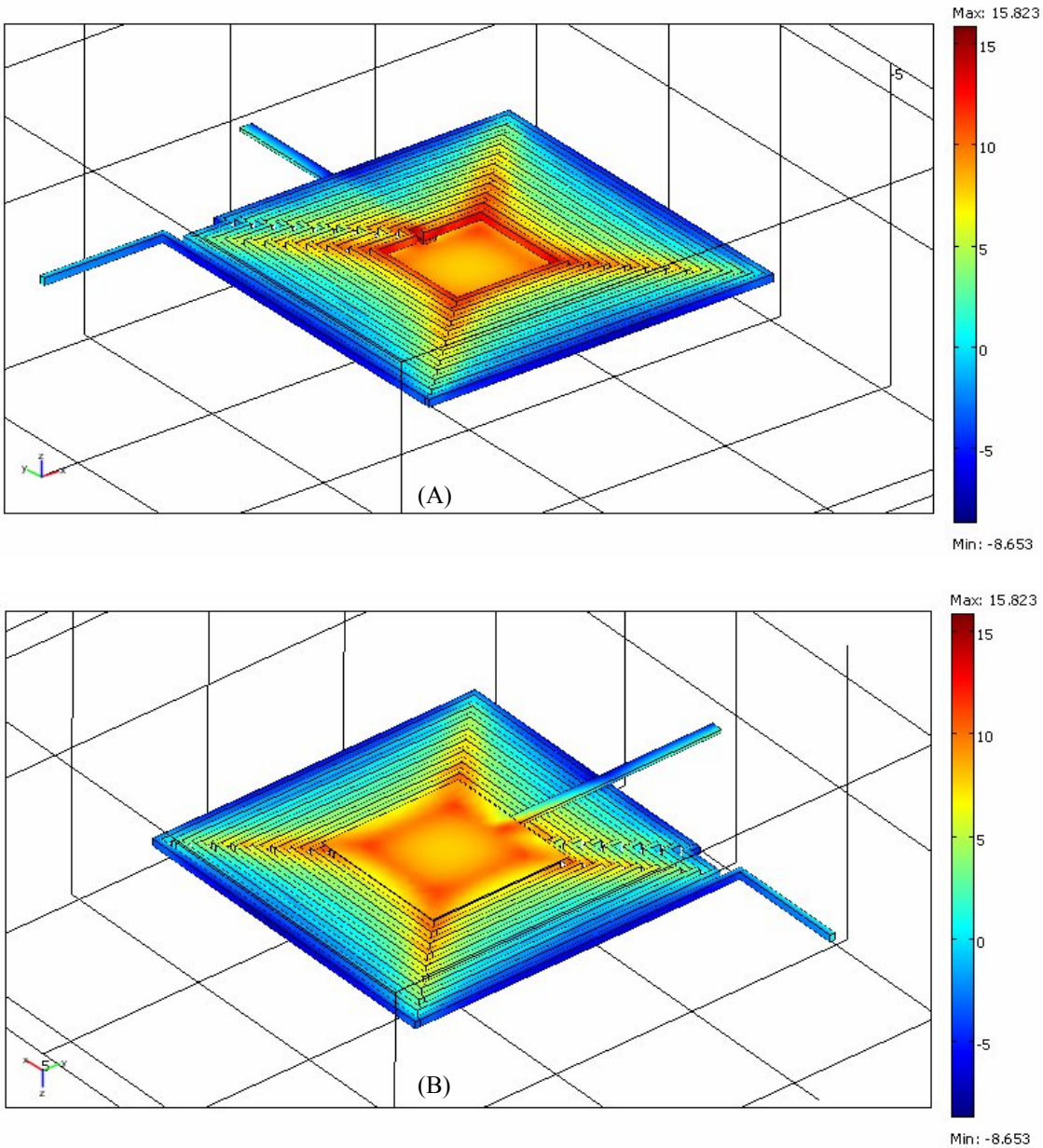

Figure 5.9 - *Z component of the magnetic field on the Hall plate surface. (A): Top view. (B): Bottom view. Units in Gauss.*

It is interesting to note that because the coil partially overlaps the Hall plate area, the region of maximum field strength is not at the edge of the Hall plate, but close to the innermost coil turn. The coil parameters obtained from the simulations are summarized in Table 5.1.

Table 5.1 - *Coil A main parameters, obtained from finite elements simulations*

Average Magnetic Field on the Hall Plate @ 5mA	8.84 G
Resistance	24.8 Ω
Inductance	8.51 nH

5.2.2.3 Coil Design Using Two Metal Layers (Coil B)

The second coil design is constructed using both metal layers. The main objective is to increase the number of turns close to the Hall plate, while still allowing the Hall plate terminals to be contacted with metal lines.

Figure 5.10 shows the result of an electrical finite element simulation of this design. Most of the voltage drop occurs in the lower metal layer, because of its higher resistivity. Table 5.2 presents the results of the simulations for coil B. The average magnetic field obtained in the Hall plate surface is 17% bigger than with the previous design.

Table 5.2 - *Coil B main parameters, obtained from finite elements simulations*

Average Magnetic Field on the Hall Plate @ 5mA	10.33 G
Resistance	63.4 Ω
Inductance	6.62 nH

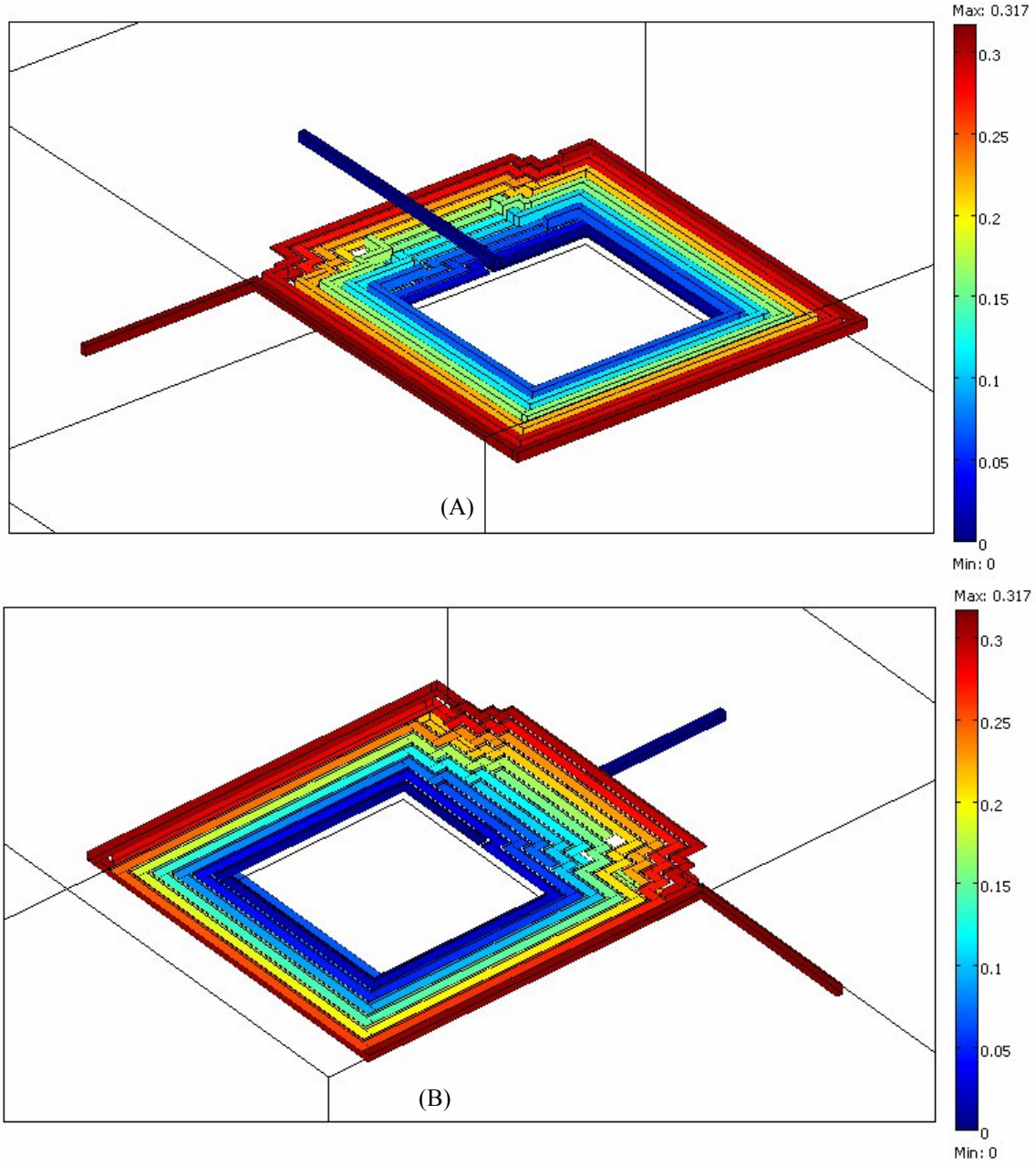

Figure 5.10 *- Structure of Integrated Coil B. (A): Top view. (B): Bottom view. For a 5mA bias current, the voltage drop in the coil is 0.317V*

5.2.2.4 Supplemental Simulations

Additional coil structures have been simulated, trying to take advantage of the fact that a positive contribution to the total magnetic field can be obtained from coil turns smaller than the Hall plate width. Because of their structure, two factors make their

implementation challenging. The first is the use of vias connecting the two metal layers inside the Hall plate area. It is customary not to place contacts (sometimes not even metal lines) over active areas. The second is the use of a layer different than metal to connect the Hall plate terminals. The Polysilicon or N+ layers could be used to contact the Hall plate, with the penalty of having a higher voltage drop along the bias lines.

The first structure to be presented consists of two coils, one implemented in Metal 1 and the other in Metal Top, interconnected at the center of the Hall plate (Figure 5.11). The average magnetic field in the Hall plate surface for this structure is 5.07G. If combined with the coil structure presented in Section 5.2.2.3, the total magnetic field would be 15.40G, an increase of 49.1%, at the price of placing a via connecting the two metal layers at the center of the Hall plate. With this combined structure the Hall plate terminals can still be contacted with metal lines.

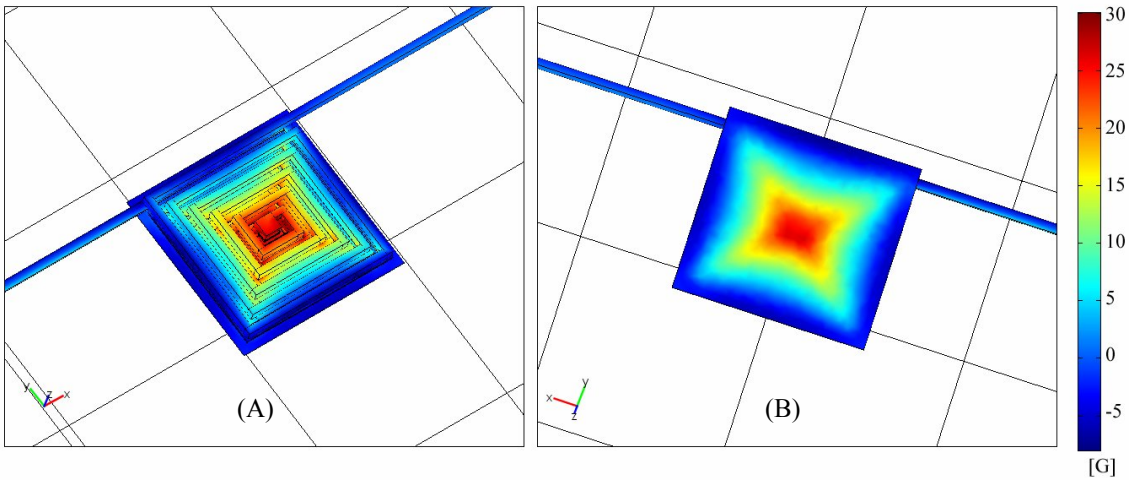

Figure 5.11 - *Z component of the magnetic field on the Hall plate surface. (A): Top view. (B): Bottom view. Units in Gauss.*

The second simulated structure expands on the ideas used in the previous coil. It consists of a Metal Top layer coil starting with a maximum width of 120μm which winds all the way to the center of the Hall plate area. At that point it is contacted with a Metal 1 coil which winds outwards to a maximum width of 120μm. The total magnetic field with this coil is 19.2G, an 86% improvement when compared to the coil in Section 5.2.2.3. The structure has a via at the center of the Hall plate, and the Hall plate terminals must be contacted either with Poly or N+ layers.

Both structures should be implemented on a future project, to measure their effects on the Hall plate sensitivity, linearity and offset distribution.

5.3 Integrated Coil Implementation

Two silicon chips have been implemented in silicon, one of them using coil A and the other using coil B. For each case, the test chip consists of a 50μm Hall plate, the integrated coil and an amplifier identical to the one used in Section 4.3.2.4. A biasing block for the amplifier was also included. For supplementary measurements a Quad Hall plate was implemented using four Hall-plate-plus-coil blocks. Also, a Hall plate with its coil but without amplification was added to the experiment.

The top level schematic view of the test chips is shown in Figure 5.12.

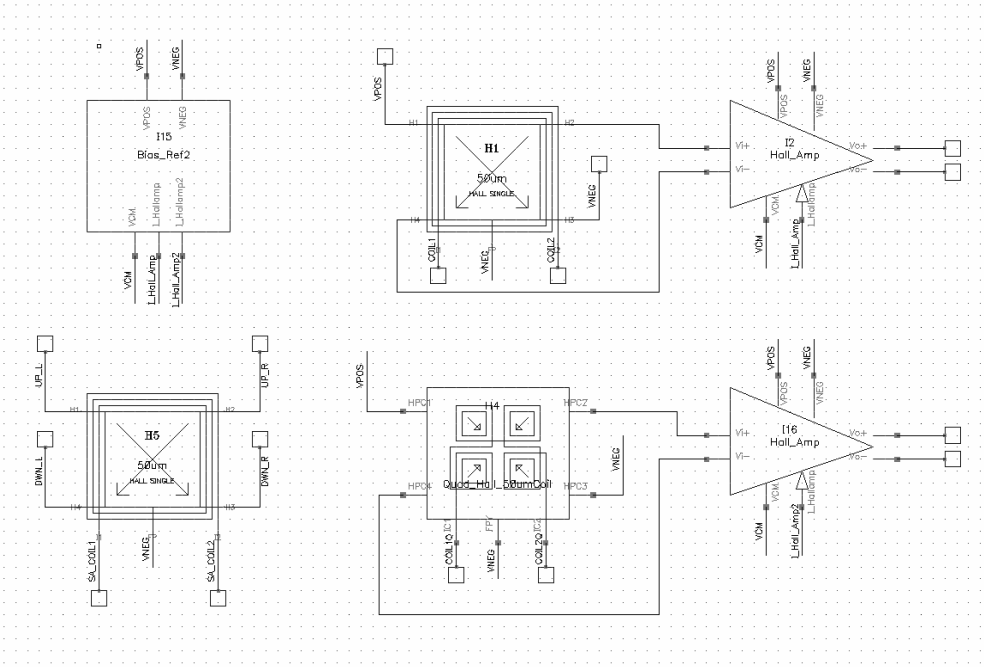

Figure 5.12 - *Top level schematic of magnetic compensation test chips.*

Figure 5.13 shows photographs of the actual test chips. The three Hall plates (two Single, one Quad), two amplifiers and the bias reference blocks can be clearly seen.

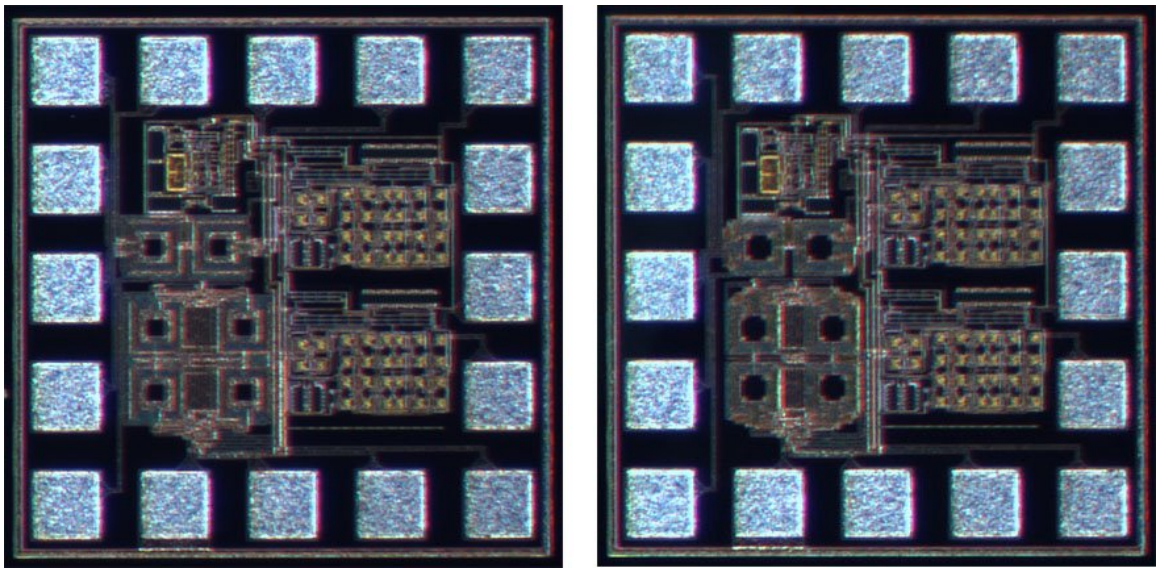

(A) (B)

Figure 5.13 *- Photographs of two test chips implemented with (A) Coil A and (B) Coil B.*

5.4 Measurements Results

5.4.1 Coil A

The test chip was wire-bonded in a ceramic package and the magnetic field generated by the coil was measured for different bias currents and external magnetic fields.

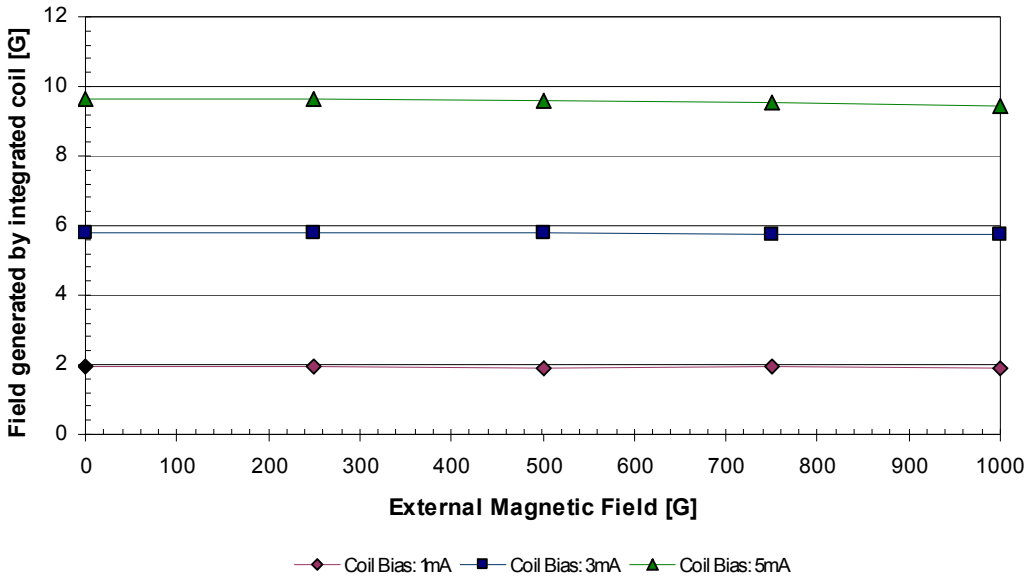

Figure 5.14 - *Magnetic field generated by Coil A for different coil bias currents and external fields. Measurements taken at 25°C.*

The magnetic field generated by the coil slightly decreases with increasing external field (see Fig. 5.14), which is an unexpected result. It was later found that the ceramic package is ferromagnetic, which might help explain this behavior. Plastic packaged parts are currently being assembled, but at the time this work was ready to be presented they were still not available. Figure 5.15 shows a plot of the magnetic field produced per mA of coil current. The reduction in coil efficiency as the external magnetic field increases is more visible in this graph. The results for the 1mA biasing current are affected in a greater way by the system noise, which explains its larger data spread.

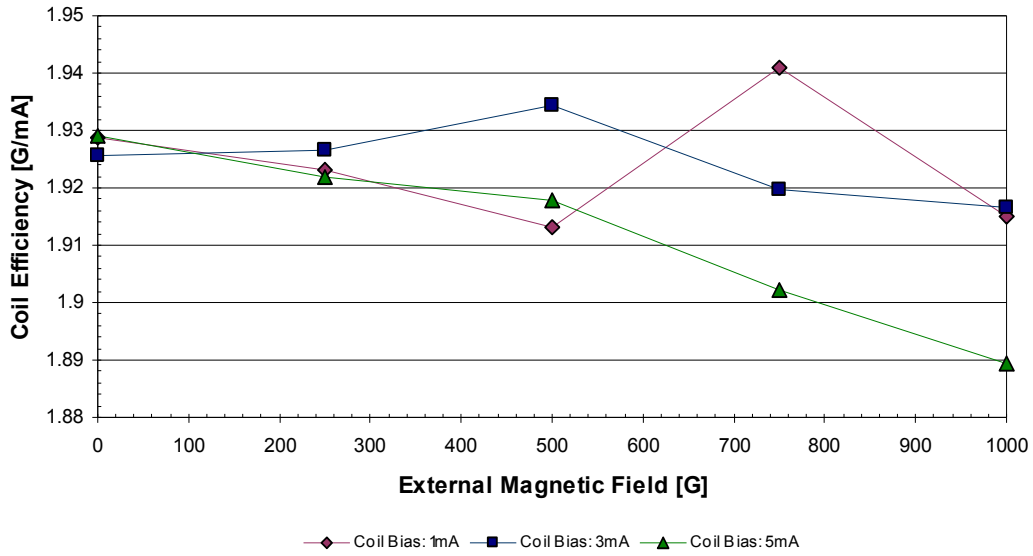

Figure 5.15 - *Coil A efficiency for different external fields. Measurements taken at 25°C.*

Table 5.3 presents a comparison of the simulated and measured parameters with no external magnetic field applied and a biasing current of 5mA. To obtain the inductance of the coil a Maxwell-Wein bridge was implemented. The coil's very low inductance and resistance values forces the rest of the components in the bridge (a capacitor and three resistors) to also have small values. This in turn causes the bridge driving voltage to be small, in order not to have an excessive current flowing through the coil. Because of all of the above, the inductance value obtained with the bridge is only a rough approximation.

Table 5.3 - *Comparison of simulated and measured Coil A parameters*

	Simulated	Measured
Average Magnetic Field on the Hall Plate @ 5mA	8.84 G	9.6 G
Resistance	24.8 Ω	29.62 Ω
Inductance	8.51 nH	< 24 nH

5.4.2 Coil B

The procedure applied to obtain the data for coil A was repeated for coil B. In Figure 5.16, the magnetic field generated by the integrated coil for different external magnetic fields and biasing conditions is presented. Again, the field generated by the coil slightly decreases with increased external field, likely again caused by the magnetic behavior of the ceramic package.

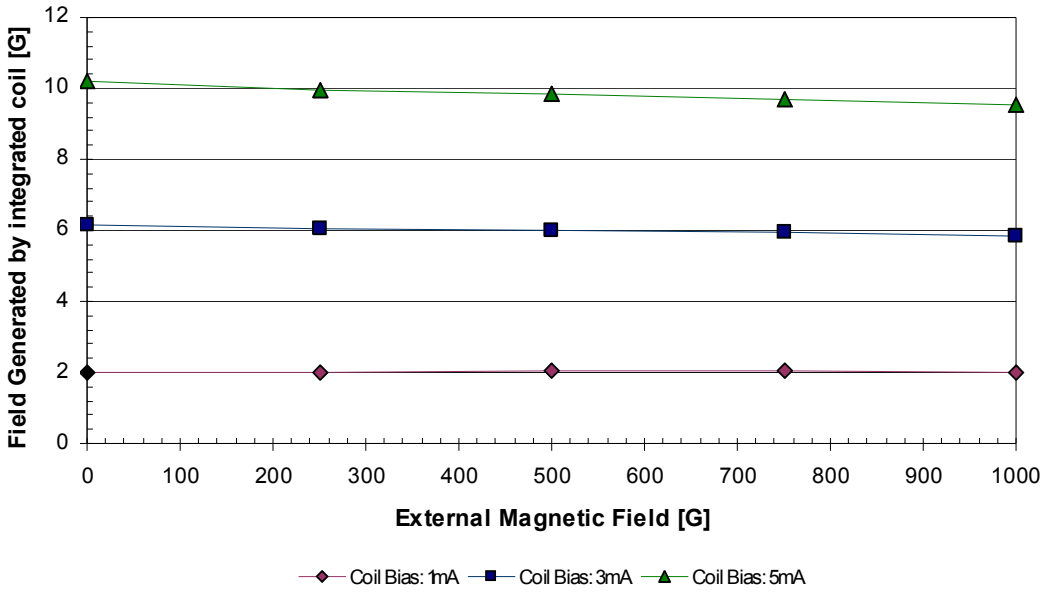

Figure 5.16 - *Magnetic field generated by Coil B for different coil bias currents and external fields. Measurements taken at 25°C.*

The reduction in magnetic field generated by the coil is more clearly seen in Figure 5.17, showing the coil efficiency as a function of the applied external field.

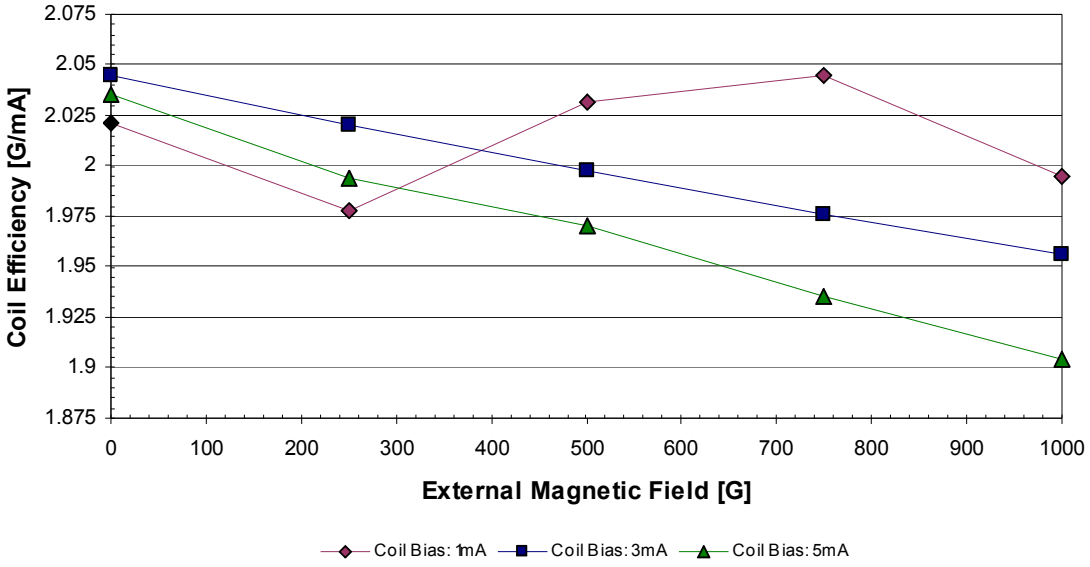

Figure 5.17 - *Coil B efficiency for different external fields. Measurements taken at 25°C.*

Table 5.4 presents a comparison between the finite element simulation and the actual behavior of the coil for a biasing current of 5mA and no external magnetic field. As with coil A, the sets of simulated and measured parameters are very close.

Table 5.4 - *Comparison of simulated and measured Coil B parameters*

	Simulated	Measured
Average Magnetic Field on the Hall Plate @ 5mA	10.33 G	10.18 G
Resistance	63.4 Ω	78.6 Ω
Inductance	6.62 nH	< 28.8 nH

5.4.3 Comparison with Previous Coil Implementations

Table 5.5 compares the performance of integrated coils reported in the past with the results from this work. There is a 67% improvement with respect to the previous best result, and a potential 217% increase if the structure proposed in 5.2.2.4 were to be implemented.

Table 5.5 - *Summary of performance data of integrated coil designs.*

Authors	Year	Hall plate size	Coil Performance	Hall Plate sensitivity[α]	Normalized Hall Plate Output[β]	Comments
J. Trontelj et al. [46]	1994	Approx. 10μm by 10μm	1G/mA	N/A	N/A	
P.L.C. Simon et al. [47]	1996	100μm by 200μm	0.3G/mA	N/A	N/A	
J. Trontelj [48]	1999	Approx. 20μm by 20μm	1.5G/mA	N/A	N/A	
M. Demierre et al. [49]	2002	2.4μm by 2.4μm	3.92G/mA	180V/AT	70.6V/A^2	Small Hall plate improves coil performance at the expense of poor sensitivity.
This work	2008	50μm by 50μm	Measured: [γ] 2G/mA Proposed: [γ] 3.8G/mA	Measured: 590V/AT	Measured: [γ] 118V/A^2 Proposed: [γ] 224.2V/A^2	

[α] Current-driven sensitivity.
[β] Output voltage per ampere of Hall plate bias and ampere of coil bias.
[γ] Measured: Empirical results from coil B. Proposed: Finite element simulation results from section 5.2.2.4.

5.5 System Implementation

5.5.1 Noise Considerations

To know the conditions where the integrated magnetic signal will be usable, it is very important to estimate the magnitude of the noise present at the Hall plate output. The most important contributions to the overall noise are the Hall device itself and the first stage of the amplifier.

The thermal noise generated by the Hall element is given by:

$$Vn_{Hall} = \sqrt{4kTR\Delta f} \tag{5.34}$$

Where k is the Boltzmann constant, T is the temperature in Kelvin, R is the resistance of the Hall plate and Δf is the frequency bandwidth of interest. The above formula can be re-written to obtain the noise contribution per unit of frequency.

$$Vn_{Hall} / \sqrt{Hz} = \sqrt{4kTR} \tag{5.35}$$

The resistance of the Hall sensor in the process where the system has been implemented is 9.7kΩ at 25ºC (see measurements obtained in Chapter 4), so the noise voltage generated by the Hall plate is:

$$Vn_{Hall} / \sqrt{Hz} = 12.6 \frac{nV}{\sqrt{Hz}} \tag{5.36}$$

In the literature, the reported input referred amplifier noise voltage for state-of-the-art amplifiers is around 20nV/√Hz [50, 53]. The total noise at the Hall plate terminals is thus equal to:

$$Vni = \sqrt{(Vn_{Amplifier}{}^2 + Vn_{Hall}{}^2)} = 23.6 \frac{nV}{\sqrt{Hz}} \tag{5.37}$$

The magnetic field generated by coil B with a 5mA biasing current is 10G, per Section 5.4.2. The sensitivity of the 50μm Hall plate encapsulated in a plastic package with a biasing voltage of 3V is equal to 15.6μV/G (Table 4.3). Thus, the electrical signal generated by the Hall element when the magnetic field generated by the coil is present is:

$$V_{Hall} = 156 \mu V \tag{5.38}$$

For the integrated magnetic signal to be usable, the signal to noise ratio should be at least 6dB. If the system must detect changes in the sensitivity of the order of 0.1%, the bandwidth should be no bigger than:

$$BW = \left[\frac{V_{Hall} / 1000}{SNR \cdot Vni} \right]^2 = \left[\frac{156nV}{2 \times 23.6 \frac{nV}{\sqrt{Hz}}} \right]^2 = 11.5Hz \tag{5.39}$$

The required low-pass filter can be implemented using a MOSFET-C filter [54].

5.5.2 Integrated Coil Switching

In order to distinguish the magnetic signal generated by the integrated coil from the external magnetic field, the direction of the coil's biasing current must be switched. A synchronized detector will later recover the amplified signal from the coil and use it to compensate the sensitivity drift. The impedance of the coil is given by:

$$Z_{Coil} = R_S + 2\pi f L_S \tag{5.40}$$

Where L_S is the inductance of the coil, R_S is its series resistance and f is the switching frequency. There is a maximum frequency at which the coil can be switched, and above it the combined impedance of the inductance and its series resistance will be such that the power supply voltage Vcc will not be able to generate the desired biasing current I_{bias} through the coil. This maximum frequency is given by:

$$f_{\max} = \frac{\frac{Vcc}{I_{bias}} - R_S}{2\pi L_S} \tag{5.41}$$

If the coil is being driven with a square wave signal, f_{max} should be equal to the x^{th} harmonic, where the harmonic is selected based on the desired level of signal distortion. With the values of inductance and resistance obtained in Sections 5.4.1 and 5.4.2, the maximum frequency will be in the GHz range. This proves that switching the integrated coil will not be a problem.

5.5.3 Proposed System

A magnetic field sensing system that automatically compensates changes in its gain because of variations in stress and temperature is presented in this section. Figure 5.18 shows its schematic diagram.

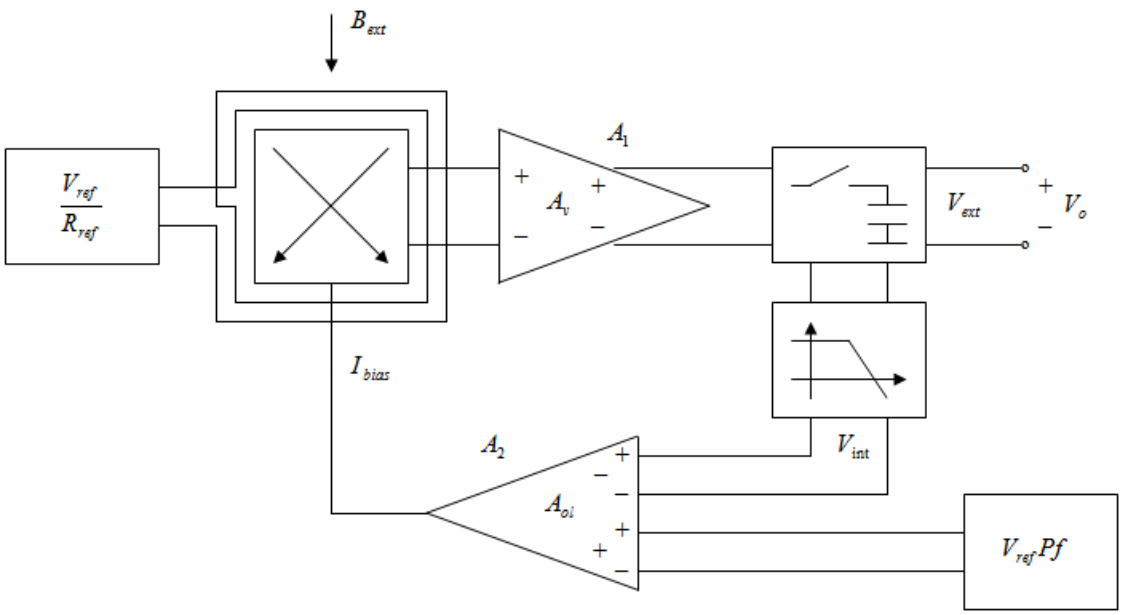

Figure 5.18 - *Schematic diagram of the proposed magnetic compensation system.*

The signal path consists of the Hall device with an integrated coil surrounding it, the amplifier A_1 (with a closed-loop voltage gain A_v) and a subsystem to discriminate the external magnetic field, the internal magnetic field and the Hall-plate-plus-amplifier offset. The feedback loop consists of a low-pass filter (Section 5.5.1) and the amplifier A_2, which controls the Hall plate bias current I_{bias}, and has an open-loop gain equal to A_{ol}. The reference to which the voltage generated by the integrated coil is compared is obtained from a reference voltage V_{ref} scaled by a unit-less proportionality factor Pf.

The output of the system due to an external magnetic field is given by:

$$V_o = B_{ext} S_I I_{bias} A_v, \tag{5.42}$$

where B_{ext} is the external magnetic field being sensed, S_I is the current-driven Hall plate sensitivity, I_{bias} is bias current of the Hall plate and A_v is the closed-loop gain of amplifier A_1. If the sensitivity in the previous equation is replaced with Equation (2.36), the expression for the output voltage is:

$$V_o = V_{ext} = B_{ext} \frac{G_S I_{bias} R_H}{t} A_v \tag{5.43}$$

It is important to notice that several parameters in the above equation depend on temperature and stress. The objective of the proposed system is to sense changes in the system gain, and compensate these variations via the Hall plate bias current.

The magnetic field generated by the integrated coil is given by:

$$B_{\text{int}} = I_{coil} k_{coil} \tag{5.44}$$

In the previous formula I_{coil} is the current flowing through the integrated coil and k_{coil} is the coil efficiency (for example, k_{coil} is equal to 2G/mA in Section 5.4.2). The current I_{coil} is generated via a reference voltage V_{ref} over a reference resistor R_{ref}.

$$B_{\text{int}} = \frac{V_{ref}}{R_{ref}} k_{coil} \tag{5.45}$$

The voltage V_{int} at the output of the low-pass filter is:

$$V_{\text{int}} = \frac{V_{ref}}{R_{ref}} k_{coil} \frac{G_S I_{bias} R_H}{t} A_v \tag{5.46}$$

The current needed to bias the Hall plate is defined by:

$$I_{bias} = A_{ol}(V_{ref} Pf - V_{\text{int}}) \tag{5.47}$$

$$I_{bias} = A_{ol}\left(V_{ref} Pf - \frac{V_{ref}}{R_{ref}} k_{coil} \frac{G_S I_{bias} R_H}{t} A_v\right) \tag{5.48}$$

In order to understand it better, the feedback loop can be redrawn as shown in Figure 5.19:

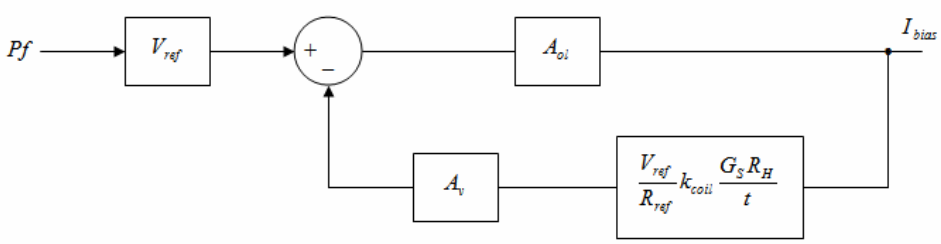

Figure 5.19 - *Feedback loop.*

For simplicity we can group some of the parameters as:

$$x = V_{ref} Pf \tag{5.49}$$

$$y = I_{bias} \tag{5.50}$$

$$\beta = \frac{V_{ref}}{R_{ref}} k_{coil} \frac{G_S R_H}{t} A_v \tag{5.51}$$

Thus, Equation (5.48) can then be re-written as:

$$y = A_{ol}(x - \beta y) \tag{5.52}$$

$$\frac{y}{x} = \frac{A_{ol}}{1 + A_{ol}\beta} \tag{5.53}$$

If $A_{ol}\beta >> 1$ then:

$$\frac{y}{x} = \frac{1}{\beta} \tag{5.54}$$

Replacing with the original parameters:

$$\frac{I_{bias}}{V_{ref} Pf} = \frac{R_{ref} t}{A_v G_S R_H k_{coil} V_{ref}} \tag{5.55}$$

$$\frac{I_{bias}}{Pf} = \frac{R_{ref} t}{A_v G_S R_H k_{coil}} \tag{5.56}$$

Rearranging the previous expression and recalling Equation (5.43):

$$\frac{V_o}{B_{ext}} = \frac{R_{ref} Pf}{k_{coil}} = \frac{I_{bias} A_v G_S R_H}{t} \tag{5.57}$$

So, with the proposed feedback scheme, the gain of the system is defined by the proportionality factor *Pf*, the coil efficiency k_{coil} and the reference resistor R_{ref}. If we manage to make these parameters independent of temperature and stress, so will be the gain of the system. The factor *Pf* is just the ratio between two voltages, and can easily be made independent of temperature and stress. The coefficient k_{coil} is believed to be constant, but the measurements with ceramic packages (which were found to be ferromagnetic) didn't help to prove it. If this supposition is found to be true, the only remaining parameter to take care of is the reference resistor R_{ref}. The easiest way to implement R_{ref} is to use an external resistor, but it has the drawbacks of having to use an extra package pin and the having to deal with an increased overall system cost. The other alternative is to use an integrated resistor. A P+ diffused resistor is a very good starting point. From the measurements in Section 4.4.4, we can see that the change in resistance due to moisture-absorption-driven stress is about an order of magnitude less than the change in Hall plate sensitivity (The Pwell resistor is better, but its big temperature drift -Section 4.4.2- rules out its use). The measurements in Section 4.4.2 show that the temperature drift of the P+ resistor from -40C to 150C is about 5%. If the P+ resistor is combined with a resistor having a negative temperature coefficient, the combined resistor can be made independent of the temperature. The effect of stress in the extra resistor must also be evaluated.

The system presented in this section allows for a closed-loop compensation of the system gain with three parameters defining the system gain outside the loop, and with only one of them limiting the accuracy of the system. It is also very important to notice

that there is no need for a temperature stabilized voltage reference to assure an accurate system, a significant advantage compared with [50] and [51].

CHAPTER VI

CONCLUSIONS AND OUTLOOK

In this work the effect of stress on magnetic Hall sensors, and more specifically on their sensitivity, was studied. The origin of these stresses and in particular the importance of the moisture absorption by the plastic package as a source of stress was investigated.

Two schemes have been proposed to compensate for the sensitivity drift. The first one uses integrated piezoresistors to measure changes in the stress conditions and use these results to compensate the sensitivity. The second employs an integrated coil to generate a reference magnetic field which can be used to implement a feedback system that dynamically compensates the variations in the system gain. In the future, the systems proposed in Sections 4.5 and 5.5 should be implemented to verify if the preliminary results presented in this thesis can be translated into a complete system.

At first sight, the compensation method proposed in Chapter 4 seems to be the one with the most prominent results. Measurements have been obtained showing Hall sensitivity compensation, which validates the theory behind it. But its implementation into a self-contained system presents several challenges. The scheme used to sense changes in stress (the integrated resistors) is also very sensitive to temperature changes. Even if a hypothetic Wheatstone bridge independent of the temperature were to be devised, the piezoresistive coefficients of the bridge's resistors would still depend on the operating temperature. At least for now, the use of a temperature sensor to track temperature changes appears unavoidable. The readings from the integrated resistors and

the temperature sensor have to be processed in order to compensate the effects of stress. The easiest way to implement the processing unit from a theoretical point of view is using a digital system. From a practical point of view, on the contrary, this becomes a challenging task. Analog to digital converters will be needed to translate the signals, a digital processing unit will have to be devised, and integrated memory banks will need to be provided. Besides, the real estate consumed by these blocks needs to be carefully considered. If this compensation scheme could be implemented entirely in the analog realm remains to be proven. It is very important to keep in mind that this is an open loop compensation scheme. In addition, only the effect of the in-plane normal stresses is being taken into account to compensate the sensitivity (it is known that e.g. the out-of-plane normal stress also affects the Hall sensitivity).

No major technical breakthroughs are needed to implement the compensation system presented in Chapter 5, provided that the magnetic field generated by the integrated coils does remain constant with varying external magnetic field. Nevertheless, there are some challenges to be tackled. One of them is to deal with the very low noise levels needed to distinguish the magnetic field generated by the integrated coil. This will require the design of a very low noise amplifier. Another challenge will be to implement a MOS-C low-pass filter which complies with the required level of linearity. Finally, there is the issue of the reference resistor and its stress and temperature drifts. At the end, a system can only be as accurate as the reference elements used to implement it.

If the two systems were to be put side by side, the main advantage of the magnetic feedback compensation scheme is that it is a closed-loop system. This means that as long

as the reference elements remain constant, any changes in the rest of the system will not affect the overall gain, regardless of the effect that causes them.

REFERENCES

[1] G. S. Randhawa, *Monolithic integrated Hall devices in silicon circuits.* Microelectron. J. vol. 12, pp. 24-29, 1981.

[2] P. J. Munter, *A low offset spinning-current Hall plate.* Sensors and Actuators, vols. A21-A23, pp. 743-746, 1990.

[3] D. Manic, J. Petr, R. S. Popovic, *Short and long-term stability problems of Hall plates in plastic packages.* 38th Annual Int'l Reliability Physics Symposium,San Jose, California, pp. 225-230, 2000.

[4] E. Stellrecht, B. Han, M. G. Pecht, *Characterization of hygroscopic swelling behavior of mold compounds and plastic packages.* IEEE Transactions on Components and Packaging Technologies, vol. 27, no. 3, pp. 499-506, Sept. 2004.

[5] U. Ausserlechner, M. Motz, M. Holliber, *Drift of magnetic sensitivity of smart Hall sensors due to moisture absorbed by the IC-package*. Proc. of IEEE Sensors 2004, vol. 1, pp. 455-458, Oct. 2004.

[6] Y. Kanda, K. Suzuki, *The piezo-Hall effect in n-silicon*. 22nd International Conf. on the Physics of Semiconductors, vol. 1, pp. 89-92, 1995.

[7] J. Lenz, S. Edelstein. *Magnetic Sensors and their applications.* IEEE Sensors Journal, vol. 6, no. 3, pp. 631-649, June 2006.

[8] V. Pizzella, S. Della Penna, C. Del Gratta, G. L. Romani, *SQUID systems for biomagnetic imaging.* Supercond. Sci. Technol., vol. 14, pp. R79-R114, 2001.

[9] R. Cantor, *SQUID's and emerging applications.* Superconductor and Cryoelectronics, vol. 13, pp. 16-22, 2001.

[10] W. Happer, *Optical Pumping.* Rev. Mod. Phys., vol. 44, pp. 169-249, 1972.

[11] D. Budker, W. Gawlik, D.F. Kimball, S.M. Rochester, V. Yashchuk, A. Wies, *Resonant nonlinear magneto-optical effects in atoms.* Rev. Mod. Phys., vol. 74, pp. 169-249, 1972.

[12] A. Overhauser, *Polarization of nuclei in metals.* Phys. Rev. vol. 91, pp. 476-476, 1953.

[13] W. Meissner, R. Ochsenfeld, *Ein neuer Effekt bei Eintritt der Supraleitfähigkeit.* Naturwissenschaften, vol. 21, pp. 787-790, 1933.

[14] M. Pannetier, C. Fermon, G. Le Goff, J. Simola, E. Kerr, *Femtotesla magnetic field measurement with magnetoresistive sensors.* Science, vol. 304, pp. 1648-1650, 2004.

[15] P. Ripka, *Advances in fluxgate sensors.* Sensors and Actuators A, vol. 106, pp. 8-14, 2003.

[16] T. R. McGuire, *Anisotropic magnetoresistance in ferromagnetic 3D alloys.* IEEE Trans. Magn. vol. 11, no. 4, pp. 1018-1038, July 1975.

[17] M. N. Baibich, J. M. Broto, A. Fert, F. Nguyen Van Dau, F. Petroff, P. Eitenne, G. Creuzet, A. Friederich, J. Chazelas, *Giant magnetoresistance of (001)Fe/(001)Cr magnetic superlattices.* Phys. Rev. Lett., vol. 61, pp. 2472-2475, 1998.

[18] R. Sunier, T. Vancura, Y. Li, K-U Kirstein, H. Baltes, O. Brand, *Resonant magnetic field sensor with frequency output*. Journal of Microelectromechanical Systems, vol. 15, no. 5, pp. 1098-1107, Oct. 2006.

[19] R. S. Popovic, *Hall effect devices.* 2nd Edition, Institute of Physics Publishing, 2004.

[20] V. I. Stafeev, *Modulation of diffusion length as a new principle of operation of semiconductor devices.* Sov. Phys. Solid State, vol. 1, pp. 763-768, Dec. 1959.

[21] R. S. Popovic, H. Baltes, F. Rudolf, *An integrated silicon magnetic field sensor using the magnetodiode principle.* IEEE Transactions on Electron Devices, vol. 31, no. 3, pp. 286-291, 1984.

[22] E. Hall, *On a new action of the magnet on electric current.* American Journal of Mathematics, vol. 2, no. 3, pp. 287-292. Sep, 1879.

[23] E. Ohta, M. Sakata, *Temperature Dependence of Hall Factor in Low-Compensated n-Type Silicon.* Japanese Journal of App. Physics, vol. 17, no. 10, pp. 1795-1804, 1978.

[24] W. Versnel, *Analysis of symmetrical Hall plates with finite contacts.* J. App. Physics, vol. 52, pp. 4659-4666, July 1981.

[25] W. Versnel, *Analysis of a circular Hall plate with equal finite contacts.* Solid-State Electronics, vol. 24, no. 1, pp. 63-68, Jan. 1981.

[26] H. Weiss, *Structure and application of galvanometric devices.* Pergamon, Oxford, pp. 88-133, 1969.

[27] A. Bilotti, G. Monreal, R. Vig, *Monolithic Magnetic Hall Sensor Using Dynamic Quadrature Offset Cancellation.* IEEE J. Solid-State Circuits, vol. 32, no. 6, pp. 829-836, June 1997.

[28] R. Steiner, A. Haeberli, F. P. Steiner, Ch. Maier, H. Baltes, *Offset reduction in Hall devices by continuous spinning current.* Sensors and Actuators A, vol. 66, pp. 167-172, 1998.

[29] U. Ausserlechner, *Limits of offset cancellation by the principle of spinning current Hall probe.* Proc. of IEEE Sensors 2004, vol. 3, pp. 1117-1120, Oct. 2004.

[30] Ch. Schott, R. S. Popovic, *Linearizing integrated Hall devices.* Transducers '97, 1997 International Conf. on Solid-State Sensors and Actuators, vol. 1, pp. 393-396, June 1997.

[31] A. Bilotti, *Current vs. voltage driving Hall cells.* Unpublished report, Oct. 2001.

[32] S. Timoshenko, *Hystory of strength of materials.* Courier Dover Publications, pp. 107-109, 1983.

[33] D. Manic, *Drift in silicon integrated sensors and circuits due to thermo-mechanical stress.* PhD thesis, Lausanne, EPFL, 2000.

[34] S. M. Hu, *Stress-related problems in silicon technology.* Journal of Applied Physics, vol. 70, pp. 53-80, 1991.

[35] J. Lau, *Thermal stress and strain in microelectronic packaging.* New York: Van Nostrad Reinhold, 1993.

[36] A. Heuberger, *Mikromechanik: Mikrofertigung mit Methoden der Halbleitertechnologie.* Springer, 1989.

[37] U. Ausserlechner, *The piezo-Hall effect in n-silicon for arbitrary crystal orientation.* Proceedings of IEEE Sensors, vol. 3, pp. 1149-1152, 2004.

[38] B. Hälg, *Piezo-Hall coefficients of n-type silicon.* Journal of Applied Physics, vol. 64, no. 1, pp. 276-282, 1 July 1988.

[39] D. Manic, J. Petr, R. S. Popovic, *Temperature cross-sensitivity of Hall plate in submicron CMOS technology.* Sensors and Actuators A (Physical), vol. A85, no. 1-3, pp. 244-248, 1999.

[40] R. Tummala, E. Rymaszewski, A. Klopfenstein, *Microelectronics packaging handbook.* 2nd Edition, Chapman & Hall, 1997.

[41] Y. Zou, J. C. Suhling, R. C. Jaeger, H. Ali, *Three dimensional die surface stress measurements in delaminated and non-delaminated plastic packages.* 48th Electronic Components and Technology Conference, pp. 1223-1234, 1998.

[42] M. Motz, U. Ausserlechner, W. Scherr, B. Schaffer, *An integrated magnetic sensor with two continuous-time ΔΣ-converters and stress compensation capability*. 2006 IEEE International Solid-State Circuits Conference. Digest of Technical Papers, pp. 1151-1160, 2006.

[43] U. Ausserlechner, M. Motz, M. Holliber*, Compensation of the piezo-Hall effect in integrated Hall sensors on (100)-Si.* IEEE Sensors Journal, vol. 7, no. 11, pp. 1475-1482, November 2007.

[44] S. Komatsu, S. Takahashi, K. Suzuki, M. Wakatsuki, Strain insensitive integrated circuit resistor pair. U.S. Patent 4236832, Jun 29, 1978.

[45] U. Ausserlechner, *The piezo-resistive effect in silicon for arbitrary crystal orientation.* Proceedings of IEEE Sensors, vol. 3, pp. 1121-1124, 2004.

[46] J. Trontelj, L. Trontelj, R. Opara, A. Pleteresk, *CMOS integrated magnetic field source used as a reference in magnetic field sensors on common subtrate.* Instrumentation and Measurement Technology Conf. pp. 461-463, 1994.

[47] P.L.C. Simon, P.H.S. de Vries, S. Middelhoek, *Autocalibration of silicon Hall devices.* Sensors and Actuators A52, pp. 203-207, 1996.

[48] J. Trontelj, *Optimization of integrated magnetic sensor by mixed signal processing.* Proceedings of the Instrumentation and Measurement Technology Conference, pp. 299-302, 1999.

[49] M. Demierre, S. Pesenti, J. Frounchi, P. Besse, R. Popovic, *Reference magnetic actuator for self calibration of a very small Hall sensor array.* Sensors and Actuators A97-98, pp. 39-46, 2002.

[50] M. Pastre, M. Kayal, H. Blanchard, *A Hall sensor analog front end for current measurement with continuous gain calibration.* IEEE International Solid-State Circuits Conference, pp. 242-243, February 2005.

[51] M. Pastre, M. Kayal, *A Hall sensor-based current measurement microsystem with continuous gain calibration.* Research in Microelectronics and Electronics, 2005 PhD vol. 2, pp. 95-98, July 2005.

[52] M. Pastre, M. Kayal, and H. Blanchard, *Continuously calibrated magnetic field sensor*. European Patent 1637898, March 2006.

[53] N. Panitantum, N. Wongkomet**,** *A low-offset high-CMRR switched-capacitor instrumentation amplifier for data acquisition applications.* Asia-Pacific Conference on Circuits and Systems, APCCAS'02, vol. 1, pp. 339-342, 2002.

[54] A. Colonna, *Una aproximación hacia la intregración total de sensores de efecto Hall con auto-calibración de ganancia magnética.* Graduation thesis, Universidad de Buenos Aires, 2005.